The reflected irradiance inside an urban environment – Its role and improved modelling for building integrated photovoltaics

Dissertation
for obtaining a doctorate degree
at the University of Natural Resources and Applied Life Sciences Vienna

Submitted by
DI Michael Revesz, BSc

Advisors:
Ao.Univ.Prof. Mag.rer.nat. Dr.rer.nat. Philipp Weihs
Ao.Univ.Prof. Dr.phil. Erich Mursch-Radlgruber
DI Dr. Shokufeh Zamini

Conducted at:
Institute of Meteorology and Climatology
Head: Univ.Prof. Mag. Dr. Harald Rieder
and
Austrian Institute of Technology GmbH
Photovoltaic Systems

Vienna, 22 June 2020

Universität für Bodenkultur Wien

AUSTRIAN INSTITUTE OF TECHNOLOGY

Thanks to my wife, Sînzi, for her patience and support when I was in great need for it. I also thank my parents who supported me during all those years. Without all the support i received I might have quit the work.

My thanks also go to my supervisors Shokufeh and Philipp. Especially to Philipp for adopting and supporting me after my time at AIT had to come to an end.

Unfortunately, the Corona virus SARS-CoV-2 pandemic hit the world while I was on short final of runway 20-PhD. It spatially separated me and Sînzi during this hard and final period of my PhD. Thanks to video conferencing tools, I was able to stay in contact with Sînzi for some "writing parties". Only little fortunate in this situation, I got some extra time at home to write on this thesis.

The research leading to these results has received funding from Austria Research Promotion Agency (FFG), research programme "Stadt der Zukunft, 3. Ausschreibung 2015", under grant agreement number 854691 (project: "PVOPTI-Ray").

Zusammenfassung

Mit dem Ziel den Energiebedarf zunehmend mit erneuerbaren Energieträgern zu decken, steigt auch der Bedarf das Solarpotential für Fassaden im Stadtgebiet genauer abzubilden. Derzeit wird in Abschätzungen speziell für Städte die Verschattung berücksichtigt. Dagegen ist jener Teil der Gesamtsonneneinstrahlung, der vom Boden reflektiert wird nur unzureichend abgebildet. Die Kenntnis der Sonneneinstrahlung im Straßenkanyon betrifft vor allem die Anwendung Photovoltaikanlagen. Jedoch betrifft das auch die Themen städtische Wärmeinsel, Klimawandel und den thermischen Komfort der Fußgänger.

Ziel dieser Arbeit war es, zunächst Defizite bei der Modellierung der reflektierten Sonneneinstrahlung zu identifizieren. Anschließend wurde der Anteil der in einer Straßenschlucht reflektierten Strahlung bestimmt, um die Relevanz des Themas und den Bedarf zu klären. Schlussendlich wurde das bereits existierende Modell SEBE (Solar Energy on Building Envelope), für Geographic Information System (GIS) Anwendungen gedacht und als geeignet erachtet, in Bezug auf die reflektierte Einstrahlungskomponente verbessert und als SEBEpv veröffentlicht.

Am Beispiel eines ost-west orientierten Straßenzuges bei der Universität für Bodenkultur in Wien, Österreich, wurde die Einstrahlung auf eine nach Süden gerichtete Fassade gemessen und modelliert. Die Messungen haben gezeigt, dass die reflektierte Komponente einen wesentlichen Anteil hat. Eine Erhöhung der Straßenalbedo von 0,13 auf 0,77 auf einer Teilfläche von etwa 30 m^2 bewirkte in den Messungen eine um fast 14 % höhere Gesamteinstrahlung in 3,5 m über dem Boden. Auf Basis von Sichtfaktoren wurde der zu erwartende Photovoltaikertrag in 12 m über dem Boden abgeschätzt. Würde die Albedo auf der gesamten Straße auf 0,5 erhöht, was einer sehr hellen Betondecke entspricht, so sind Ertragssteigerungen von 7,3 % zu erwarten.

Das verbesserte Tool SEBEpv wurde an Hand von Messungen über mehr als zwei Jahre validiert. Die reflektierte Komponente wurde deutlich genauer berücksichtigt. Dazu gehört unter anderem, dass am Boden abhängig von möglicher Verschattung durch Gebäude Sonneneinstrahlung räumlich unterschiedlich auftrifft und deshalb auch entsprechend reflektiert wird. Mehrfachreflektionen sind zum derzeitigen Stand jedoch nicht berücksichtigt und betragen Schätzungen zufolge wenige Prozent. Zuletzt wurde SEBEpv für eine Fallstudie des Photovoltaikertrages in Abhängigkeit der Parameter Straßenalbedo (0,13, 0,56), Fassadenorientierung (Süd, Ost, West) und Photovoltaiktechnologie (kristallines Silizium, CIGS) verwendet.

Abstract

With the goal of satisfying our energy demand with renewable sources, there is an increasing need to model the solar potential on facades in the urban environment. Currently, models consider shading specifically for the urban solar potential. However, the portion of solar radiation that is reflected from the ground onto the buildings is not considered satisfactory. Knowing the solar radiation inside an urban canyon concerns mainly the application photovoltaic systems for electricity production. Nevertheless, other topics are the urban heat island effect, climate change or the thermal comfort of the pedestrians.

The aim of this work was first, to identify shortcomings of solar resource models with regard to the reflected radiation. Then the portion of radiation reflected inside a street canyon compared to the total radiation was determined to assess relevance of the topic and further needs. Finally, the model for determining the reflected component in the existing tool SEBE (Solar Energy on Building Envelope) was improved. SEBE is intended for Geographic Information System (GIS) applications and was regarded as suitable to implement changes. The final tool was then published as SEBEpv.

Using the example of a street canyon oriented east-west at the University of Natural Resources and Life Sciences, Vienna, Austria, the irradiation at a south-facing facade was measured and modelled. The measurements showed that the reflected component is significant. Increasing the ground's albedo on a small portion of 30 m^2 from 0.13 to 0.77, an increase of the resulting total radiation by almost 14 % was measured at 3.5 m above ground. Based on view factors the expected photovoltaic yield was estimated 12 m above ground. Increasing the ground-albedo on the whole street to 0.5, corresponding to highly reflective concrete, then photovoltaic yields were expected to increase by 7.3 %.

The improved tool SEBEpv was validated using more than two years of measurement data. It was found that the reflected radiation was modelled better. Amongst others, it concerns spatial distribution of radiation onto ground due to shading by buildings and resulting reflection by the ground. However, multiple reflections were not considered in the current state, resulting in an estimated bias of a few percent. Finally, SEBEpv was used for a case study assessing photovoltaic yields depending on the ground's albedo (0.13, 0.56), facade orientation (south, east, west) and photovoltaic technology (crystalline silicon, CIGS).

Contents

1 Introduction

Solar resources in an urban environment have been assessed for the last decades. Mainly, the interest was focused on simulating thermal properties of buildings (Robinson and Stone, 2004), but also regarding urban heat island mitigation related to climate change (Taha, 1997). Rather recent, interest grew for the assessment of the solar potential on roofs or on facades for electricity production with photovoltaics (PV) (Hofierka and Zlocha, 2012; Redweik et al., 2013). This work focused on the reflected irradiance onto building facades inside a street canyon. The amount and contribution of the reflected irradiation to the total solar irradiation onto facades was assessed and a model was refined and validated. Furthermore, the results were used to assess the solar potential for producing electricity with facade integrated or attached photovoltaics.

In this thesis, first, the motivation for the work is introduced in section 1.1. Afterwards, in section 1.2 the components of solar radiation are described from different points of view, followed by the state-of-the-art of modelling the reflected radiation. Then follow the hypotheses and objectives in sections 1.3 and 1.4. Further, in section 1.5 the measurements taken to assess the significance of the reflected component and the potential impact of increasing the ground's reflectivity are briefly introduced. Then, in section 1.6 the basic ideas for an improved model for the reflected radiation are described. Finally, a case study for the solar potential and the PV yield on vertical facades with different orientations and photovoltaic technologies are presented in section 1.7.

1.1 Motivation

The solar resource on surfaces in a complex urban environment is undoubtedly of great interest for the future renewable energy production using Building Integrated or Attached Photovoltaics (BIPV/BAPV). On international (IEA, 2014; Krawietz et al., 2016) and local level (e.g. reports by Dvorak (2016); Fechner et al. (2016); Magistrat der Stadt Wien (2019)) policies and directives were given to foster an increased share of BIPV in cities for local electricity production. The advantage is that renewable energy is generated closely to the consumer, whilst transportation losses are avoided (IEA, 2019). Especially in cities with its taller buildings PV systems on the available roof surfaces are not able to meet the building energy demand. Therefore, facades are important as additional surfaces for electricity generation (Osseweijer et al., 2018). Building facades are the last available surfaces for installing PV systems without consuming surfaces that are needed for other purposes. However, the performance of BIPV depends strongly on shadow-casting structures in the built environment. Thus, modelling electricity yields of BIPV is more complex than of regular PV systems (Osseweijer et al., 2018).

Another field where the solar resource in the urban environment is of great interest is related to Climate Change and the Human Thermal Comfort: Urban Heat Island Mitigation. One very effective measure that was proposed is an increase of the surfaces' albedo. The purpose is reflecting as much solar irradiance as possible back to the atmosphere and out of the urban canyon (Taha, 1997; Santamouris, 2014; Mohajerani et al., 2017). In addition, such measures also have a positive side effect on PV at facades: increasing electricity production. The important factor in this context is the radiative energy balance in the built environment. There are also further factors that are relevant, such as the near and far infrared spectrum of the solar radiation, which contribute to the thermal energy balance (Taha, 1997; Matzarakis et al., 2007). However, this part of the spectrum is not considered in this work.

One component that has a significant contribution to the total solar resource inside urban street canyons is the reflected radiation. This is especially valid for ground surfaces and the building facades as well as the respective exploitation of the solar resource. Inside a narrow street canyon one can easily argue that the strong limitation of the sky view for those surfaces also reduces the diffuse solar irradiation from the sky. As a consequence, the relative portion of any other irradiance component increases. With the possibility of altering the reflectivity of the ground or facades, the portion of reflected irradiation can be increased by higher reflectivity as well. Therefore, this component and its relation to surface reflectivity in a complex urban environment is of interest.

1.2 State-of-the art

1.2.1 The composition of solar irradiance

The solar radiation can be characterised by different means, such as its attribution to a part of the spectrum or the source of radiation. In this work, "solar radiation" means the terrestrial solar radiation, as after all absorption and scattering processes by the atmosphere and considering any indirect contribution from surface reflections. The knowledge of the composition of the radiation and its spectrum is not only relevant for understanding assumptions in modelling. There are also some implications on the choice of measurement devices due to the devices' properties and measurement mechanisms.

Spectral characterisation: The solar radiation can be characterised by attribution to different portions of the spectrum. The spectrum is divided into three portions (see Figure 1): Radiation with a wavelength shorter than about 0.4 μm is called ultraviolet (UV). The portion of spectrum between 380 and 780 μm is called the visible light. The next range of larger wavelengths is called infrared (IR), which is further sub-divided in near infrared (NIR, until 1.5 μm) and far infrared. There are wavelengths emitted beyond the IR portion which are not relevant in this context. The visible part of the spectrum also makes almost 50 % of the energy received on the ground (Ahrens, 2008; Malberg, 2002; Quaschning, 2011). For Photovoltaic applications only the spectral portions from UV to the NIR are relevant (Quaschning, 2011).

Components of incident irradiance on arbitrary surfaces The irradiance onto a surface originates mainly from the direction of the sky and to a small extent also from other surfaces according to their reflectance. These possible components are depicted in Figure 2. The so called "sky irradiance" consists of the "direct" radiation from the sun (if not obstructed by clouds) and the "diffuse" component being either sun's irradiation scattered within the atmosphere or scattered within clouds. The latter is incident from the whole visible sky. The diffuse component is considered as isotropic by some models, but by now an anisotropic distribution over the sky hemisphere is considered the standard (Maxwell et al., 1986; Gueymard, 2009; Demain

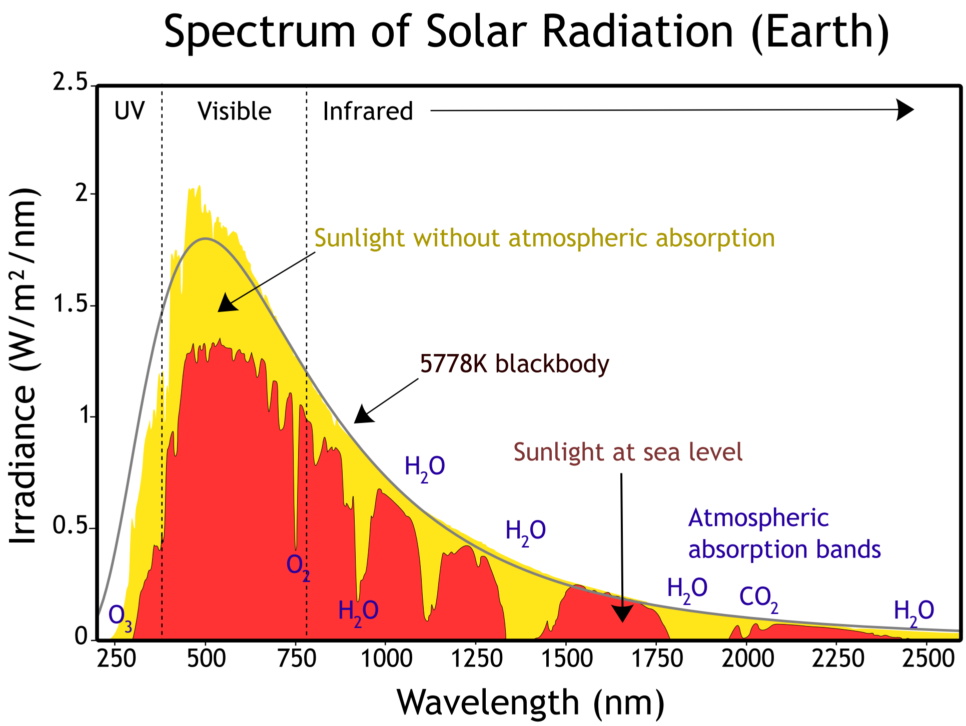

Figure 1: Spectrum of the solar radiation: Yellow - extra terrestrial, red - terrestrial radiation at sea level, black line - expected spectrum of a black body with 5778 K. © Nick84 / Creative Commons / CC-BY-SA-3.0, version 16:10, 13 May 2019 with changed limits of visible radiation, source: `https://commons.wikimedia.org/wiki/File:Solar_spectrum_en.svg`.

et al., 2013).

For measuring and modelling the sky irradiance, three terms are commonly used: Onto a horizontal plane the total irradiation is the Global Horizontal Irradiation (GHI). Solely the diffuse component on the same plane is the Diffuse Horizontal Irradiation (DHI). The direct radiation from the sun in direction of the sun's position is the Direct Normal Irradiation (DNI) (Maxwell et al., 1986). Knowing at least two of those three components from measurements allows to transpose the incoming sky irradiance onto an arbitrarily oriented and tilted surface. The relationship between those three definitions of sky irradiance components is given by Equation 1:

$$G_{GHI} = G_{DNI} \ \cos\vartheta + G_{DHI}, \tag{1}$$

with ϑ the solar zenith angle and G_{GHI}, G_{DNI} and G_{DHI} the respective components of sky irradiance as listed before. The transposition onto an arbitrarily tilted plane is then given by Equation 2:

$$G = G_{DNI}\ \cos\beta + G_{DHI}\ T_d + \rho\ G_{GHI}\ T_r, \tag{2}$$

where G is the irradiance onto an arbitrarily tilted plane, β is the angle of incidence between the sun and the tilted plane of interest, ρ the surface albedo of the surrounding and T_d and T_r transposition functions for the diffuse sky irradiance and reflected irradiance, respectively (Gueymard, 2009; Demain et al., 2013).

The reflected irradiance is the one reflected from any surrounding ground and buildings as well as other objects. Usually, all surfaces are summarised using a bulk reflectance (with one bulk albedo for all surfaces) (Maxwell et al., 1986). In modelling, mostly, only single reflections are considered while in reality there are multiple reflections happening between all surfaces. Those may be considered in models only up to some degree (Qin, 2015). Furthermore, reflectance is mostly considered as being isotropic, although, for some materials as metals or glass it is a specular reflectance (Maxwell et al., 1986).

Different models exist for describing the distribution of radiation coming from the sky fault. As stated, there are isotropic models, but more important many anisotropic models (Maxwell et al., 1986; Gueymard, 2009). Amongst the anisotropic models, the most famous ones were developed by Temps and Coulson, Klucher, Hay, Muneer, and Perez et al. (in chronological order). The Perez model was found to provide the best results for a wide variety of locations (Robinson and Stone, 2004; Gueymard, 2009). Furthermore, it is a so called "all-sky model", meaning the model's coefficients fit for a statistical occurrence of both clear and overcast sky conditions (Gueymard, 2009). Thus, for locations with a similar distribution of clear and overcast sky compared to where the model was calibrated the bias will be close to zero in average. Furthermore, the absolute bias increases with either very high or very low diffuse fraction (Revesz et al., 2020).

Irradiation from the ground is reflected anisotropically. The anisotropy depends on different factors such as the specularity of the material, sun's position relative to the surface, but also other material and surface properties. The determined albedo of a surface also varies with the source of

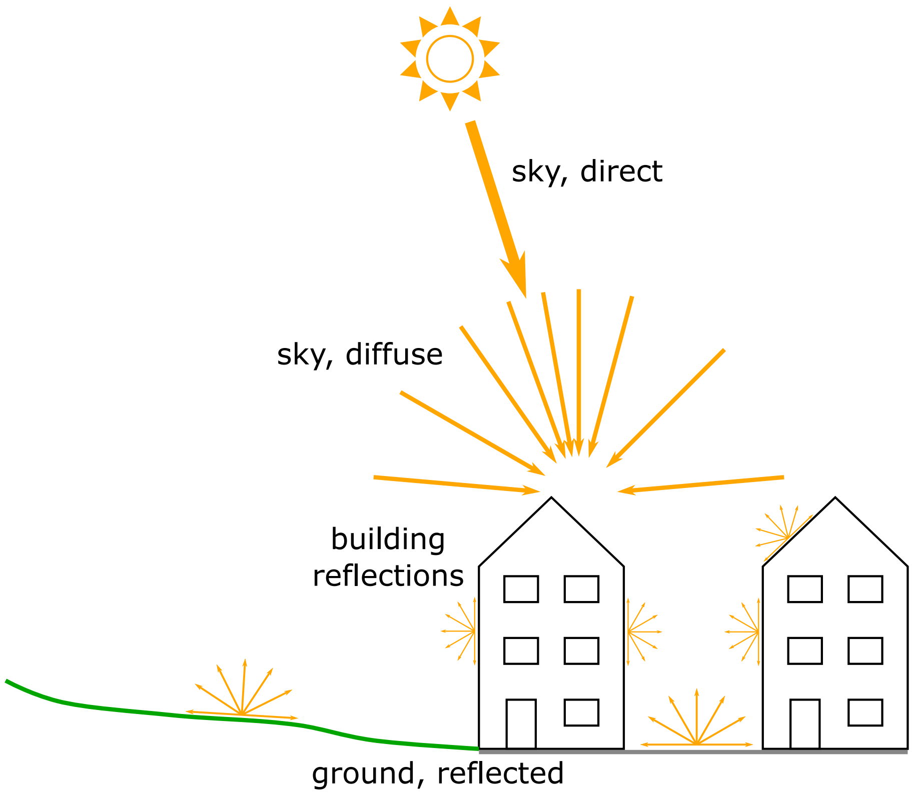

Figure 2: Composition of the irradiance from the sun and the environment. Surfaces only reflect irradiance proportionally to the solar radiation they receive.

radiation, depending on the fraction of direct solar radiation compared to diffuse radiation from the sky. It is difficult to determine all factors and therefore it is impractical to implement anisotropy in models. Hence, the isotropic assumption seems reasonable enough for modelling the reflected component (Ineichen et al., 1990).

1.2.2 Modelling the reflected irradiation

The reflected irradiation onto tilted surfaces is determined using a few different methods, also depending on the needs and purpose. In the following the most important methods are listed starting with the one that is used the most:

1. Geometric, simplified approach (Ineichen et al., 1990)
2. Ray-tracing methods (see (Freitas et al., 2015))

3. View-factors (see (Chatzipoulka et al., 2016, 2018; Calcabrini et al., 2019))

4. Geometric considerations for ideal, simplified canyon structures (e.g. by Qin (2015))

More detailed reviews of typical models and methods being used were published by Freitas et al. (2015); Jakica (2018); Revesz et al. (2020).

The geometric simplified approach, herein called "standard approach", is the one usually used for estimating the solar resources for PV applications or even (bio-) meteorological studies (see e.g. Šúri et al. (2005); Sa PVsyst (2012); Dr. Valentin EnergieSoftware GmbH (2013); Lindberg et al. (2015)). With this method the reflected component R is calculated as

$$R = \frac{1}{2}\, G_{GHI}\ \rho\ (1 - cos\ \theta), \tag{3}$$

with G_{GHI} the global horizontal irradiance onto the ground, ρ the albedo of the ground and θ the tilt angle of the receiving surface. It is based on a couple of assumptions, that are: (i) isotropic reflections (ii) from an infinitely large area with a (iii) homogeneous constant albedo ρ (Ineichen et al., 1990). In a broader sense, the "ground" can be interpreted as anything, even non-flat surfaces, that is effectively visible to the receiving surface. Then the tilt angle is considered relative to the apparent "ground". However, that requires estimations which potentially cause larger uncertainties.

Shortcoming of original approach for complex urban environment
While Equation 3 was sufficient and effective for most applications so far, it does not suffice for today's interest in solar resources inside an urban canyon. First, surfaces that reflect towards a facade are usually the ground which may be partially shaded, or another facade. Neither really receives the assumed irradiance GHI. Second, the albedo varies besides the presence of specular reflectance on windows or metal surfaces in the city. To summarize the shortcoming, for the application of estimating the solar potential in complex urban canyons most assumptions don't hold as discussed by Revesz et al. (2018).

1.3 Hypotheses

So far it was assumed that the reflected irradiance component is significant compared to the total irradiation onto building facades inside a street canyon. With the knowledge of the model that represents the reflected component one can raise the question if it is a suitable model, given the environment it will be applied to. Therefore, the following was claimed:

- The reflected irradiance onto facades inside an urban canyon is significant.

- Under current assumptions and using state-of-the-art models its value is overestimated.

The conducted research aimed at answering and proofing the claims. Improving models with regard to the reflected component would increase the reliability of e.g. electricity production forecasts for facades. Thus, lower uncertainty may have positive impact on the acceptance of electricity produced from a renewable source such as BIPV/BAPV mounted on facades, especially, in case the economic benefit is rather low.

1.4 Objectives

The objectives of this work were:

Determine the amount of the (ground)-reflected component Setup and perform measurements to determine the amount of reflected irradiance and if not the absolute values, at least the gains from increasing the surface albedo. Measurements were to be taken inside a real street canyon, which is representative for a city.

Assess the relevance of the reflected component for the application of energy production using PV Initially, the significance of the reflected radiation compared to the total solar resource was to be assessed for BIPV/BAPV applications based on the measurements. Furthermore, a case study was supposed to demonstrate an assessment for different orientations of building facades and different PV-technologies.

Improve state-of-the-art modelling of the reflected component in a complex urban environment The aim was to use a method that allows to model the complex urban structure on a larger scale than only a single building, or eventually including only directly neighbouring buildings. Ray-tracing methods are not favoured as their computational requirements don't allow an application on that scale.

1.5 Measurements inside an urban canyon

To assess the amount of irradiation received by facades the irradiance was measured at various points inside an urban canyon (for all details see (Revesz et al., 2018)). An east-west oriented road in between two buildings at the University of Natural Resources and Life Sciences in Vienna, Austria was selected. The street canyon was representative enough for many streets in the city of Vienna. During the measurements, the ground-albedo was temporary increased from 0.13 (asphalt) to 0.77 (on a limited area of about 30 m^2,) to assess its impact. The larger albedo was obtained by placing styrofoam panels on the ground that were painted white. In addition to irradiance measurements, three mini-PV modules were mounted vertically, facing south. The canyon with the temporary increased reflectivity is shown in Figure 3. At the top of one of the buildings the undisturbed direct normal and global horizontal irradiance were measured. While these measurements were ongoing for more than two years, the ground-albedo was only altered for a total of six non-consecutive days.

The irradiance inside the canyon was measured using silicon diode-based instruments to allow easy comparison with the PV modules. This choice allows to neglect a couple of device typical behaviour, such as the impact of the angle of incidence or the spectral composition of the incoming radiation. However, that also causes some uncertainty for comparisons with simulations of the irradiance when GHI as model input was measured using a pyranometer. A few points had to be chosen that were easily accessible during the campaign. Therefore, the main measurement site (facing south) was located only about 3.5 m above ground. The main site's instrumentation is shown in Figure 4. Also, the reflectivity of the ground and of the two opposing facades were determined from measurements.

Furthermore, fisheye images were taken for selected points facing in the directions of the involved facades. The images were used to assess the view-

Figure 3: Fisheye image of the street canyon with a view to the south (view point of the PV modules). The white styrofoam panels on the ground for increasing the ground's albedo are shown. ©(Revesz et al., 2018)

factors of different wall points and a central ground point. Those views cover the respective sky-view-factors as well as view-factors to the opposing facades and the ground. The fisheye images were assumed to be representative for the whole canyon, though, it is obvious that this was not true. Especially the sky-view-factor estimated from an image at the vertical centre of a facade is not equal to the one expected at the top of a building.

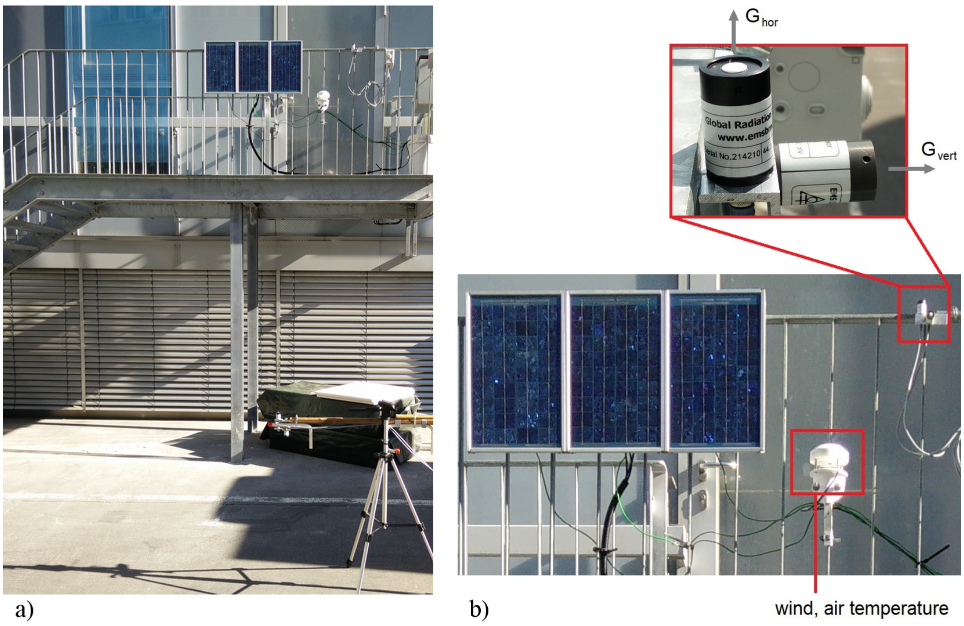

Figure 4: Main measurement site at the south-facing facade showing (a) mounting of PV modules, irradiance sensors and anemometer; (b) enlarged view of the measurement equipment (bottom) and the horizontal and south-facing silicon diode irradiance sensors (top). ©(Revesz et al., 2018)

1.6 Modelling the irradiance onto facades

The second part of this work was to develop (or at least improve) a model to estimate the reflected component of irradiation inside an urban environment in a more precise way. The chosen requirements were as follows:

- Usage of Digital Surface Model (DSM) data as urban geometry input.
- Ability to run simulations on district level in a reasonable amount of time.
- Possibility to use already available software.

Needless to say, on that scale ray-tracing tools are not applicable. Furthermore, ray-tracing tools require a 3D vector model of the scenery, which is not yet as widespread even for larger cities as DSM data. It was found practical to use the GIS based tool SEBE (Solar Energy on Building Envelope) as basis (Lindberg et al., 2015). The solar irradiance was already implemented using reasonable models as discussed by Revesz et al. (2020). Since the reflected component was implemented as a variant of the "standard approach" as described in section 1.2.2, this tool was suitable for implementing improvements. The new tool was named SEBEpv, due to its additional incorporation of a PV model as described later in section 1.7.

In addition to SEBEpv, another simple modelling approach was developed: based on view-factors. This approach was developed to ease the evaluation of errors in the model as well as the measurements. It also allowed the prognosis of the reflected component for chosen, realistic situations at the measurement site. While SEBEpv does not consider multiple reflections in its current improved state, the view-factor approach considers multiple reflections up to second degree (Revesz et al., 2018).

Typical values of the albedo There are a few surface reflectivities with relevance in regard to this work. Since the topic has a focus on modelling the current state and comparing the effect of an increased ground-surface albedo, the following surfaces are relevant: the albedo of building facades (however, here only considering a typical average) and the reflectivity of mainly present asphalt streets as well as a potential future bright surface for streets. Typical values are 0.13 for asphalt and between 0.2 and 0.3 for buildings and surroundings (Matzarakis, 2001). For a very bright concrete surface, that potentially can be used for heat island mitigation, an albedo of 0.56 was measured. Site specific values of relevant facades at University of Natural Resources and Life Sciences, Vienna, were measured as 0.5 for plastered walls and 0.27 for a partially opaque glass facade (Revesz et al., 2017; Weihs et al., 2018).

1.7 Case Study: PV power potential on an Urban Building Envelope

In the following, the case study about the effect of altering the ground-albedo on the PV yield at facades is presented. The case study was about demonstrating the effect of increased albedo on BIPV, as expected from very bright concrete surfaces. Different parameters were investigated in this study such as ground reflectivity, facade orientation and PV technology. Without the final model for reflected irradiance being finished some preliminary results were published in Revesz et al. (2017). In the following, the case study and its results using the final state of the model SEBEpv are presented.

Studied parameters and scenarios In this final case study several street canyons were formed by four adjacent building blocks as shown in Figure 5 a). The canyon width and building height was 20 m, respectively, as shown in the canyon profile in Figure 5 b). Thus, the street-width to building-height ratio is one, which is typical at least for some districts of Vienna, Austria. This constellation was used to study amongst others the effect for different orientations of facades (facing south, east and west). The positions of wall points that were evaluated for these three facade orientations are marked with a black dot in Figure 5 a). The final value used was the mean value within the upper 5 m and 2.5 m to either side of that point. It must be noted, that the results are only comparable with locations that have similar sky and irradiance conditions as measured during the study and that are located at similar latitudes as Vienna, Austria.

Within this case study the energy yield of PV plants located at the upmost 5 m of a building was evaluated changing the following two parameters:

- First, the reflectivity of the ground within the street canyon was altered. The albedo of normal asphalt with 0.13 was used for one case and then increased to 0.56 in the other case.

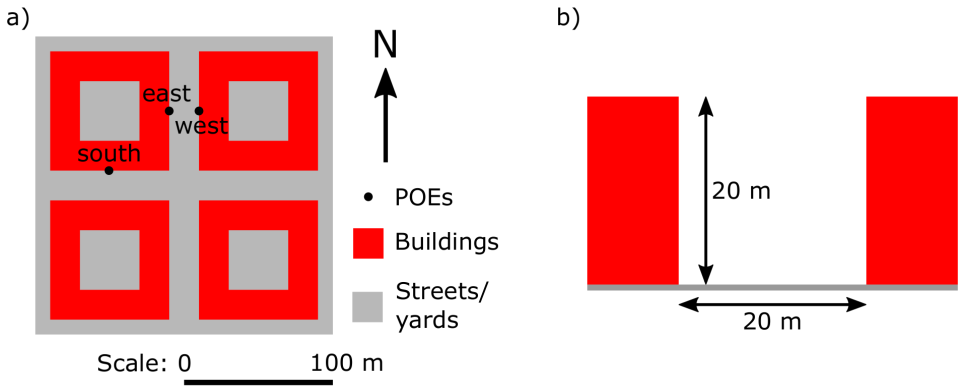

Figure 5: Scenario forming perpendicular street canyons with a street-width to building-height ratio of one. A) Land cover of buildings forming street canyons (top view, north on top); the wall point of evaluation (POE) are marked with a black dot. B) Cross section of the street canyon with building height and street width of 20 m, respectively.

- Second, the PV technology was altered choosing the most common technology, crystalline silicon (c-Si), and one thin-film technology, CIGS. The latter PV technology is considered as one of the most promising technologies in the future. Most important however, for CIGS the losses with increasing temperature are less than for c-Si (Sellner et al., 2012). Therefore, CIGS may have an advantage in environments and under conditions that potentially heat up more as given for BIPV/BAPV.

Meteorological data used A bit more than two years of meteorological data that was collected at the University of Natural Resources and Life Sciences, Vienna was used for this case study, as described in section 1.5. However, data is missing for continuous periods during the time from 20.01.2017 until 22.02.2017, 27.11.2016 until 11.01.2017 and from 31.01.2018 until 23.02.2018. Therefore, monthly sums may not correspond to expected sums in the respective months in the results. In order to compensate missing data, for each day of the year the mean of the daily aggregated sum of PV yield was used and thereafter aggregated to monthly sums. Nevertheless, over all data the period from 31st of January until 22nd of February remained without any available data.

PV model: potential power output The Energy Yield (EY) for PV modules and systems is the produced electric energy compared to (or normalised by) its installed nominal capacity under standard test condition. For this study the yield was estimated from the simulated total irradiation onto the respective facade using a simple model as published by Huld et al. (2010, 2011). The model is based on six parameters that are determined in laboratories for different PV technologies. Producer specific characteristics are not reflected by those parameters. However, general characteristics which distinguish different technologies are reflected well enough for this case study.

For the case study the model inputs were the irradiation (G in W m^{-2}) in plane of the PV modules, i.e. vertical for this study, as simulated with SEBEpv and the estimated cell temperature of the PV modules (T_{cell}). The modelled energy yield per installed nominal peak power of 1 Wp is:

$$Y(\bar{G},\bar{T}) = \frac{\bar{G}}{1\text{Wp}} \cdot [P_{STC} + k_1 \cdot \ln(\bar{G}) + k_2 \cdot \ln(\bar{G})^2 + k_3 \cdot \bar{T} \\ + k_4 \cdot \bar{T}\ln(\bar{G}) + k_5 \cdot \bar{T}\ln(\bar{G})^2 + k_6 \cdot \bar{T}^2] \tag{4}$$

with P_{STC} the module's power under standard test conditions per installed 1 Wp of PV, the six coefficients $k_1 - k_6$ and the two abbreviations defined as $\bar{G} := G/(1000 \text{ W m}^{-2})$ and $\bar{T} := T_{cell} - 25°\text{C}$ (Huld et al., 2010, 2011; Huld and Amillo, 2015).

The PV cell temperature was calculated from equations 5 and 6 as follows:

$$T_{cell} = T_{mod} + \bar{G} \cdot \Delta T \tag{5}$$

$$T_{mod} = G \cdot \exp^{a+b \cdot v} + T_{amb} \tag{6}$$

where T_{mod} is the PV module temperature, ΔT is a temperature difference depending on mounting and module-design (King et al., 1998, 2004), v is the wind speed, a and b are empirical coefficients and T_{amb} is the ambient air temperature around the PV modules. The two coefficients are characteristic for the mounting of the modules as well as the PV module type (King et al., 2004). In this study the PV modules were assumed to be mounted well ventilated and being assembled as sandwich of glass/cell/polymer-backsheet layers.

Although the power output is mainly determined by irradiance and temperature, several effects influence the power output of PV modules, but are neglected here. Those are variations of the spectrum due to the atmospheric composition, reflection losses on the module depending on the Angle of Incidence (AOI) or dirt on the modules (Ransome et al., 2012; Kubicek et al., 2014). Except for the last one, the others are effective if the irradiance is measured using a pyranometer instead of a calibrated reference cell built from the same PV material as the PV modules. Overall, this may not be a problem here as the different scenarios being compared here are subject to the same errors and therefore, do not affect a direct comparison.

Results - Estimated PV yield on building facades The total annual EY for either PV technology and the different compared scenarios are shown in Table 1. Those values are noted as metric $\sum$. Comparisons of the higher albedo (0.56) with the low ground-albedo (0.13) for the same technology (noted as $\Delta_{0.13}$) as well as comparisons of CIGS and c-Si for either of the respective albedos (noted as $\Delta_{\mathrm{c-Si}}$) are provided as relative difference in percent. In all cases the EY for a south facing facade was largest. PV modules on east and west facing facades deliver less yield by 25 %. As expected, east and west facing results show the same performance. The marginal differences could be due to slightly more cloud cover during morning hours compared to evening hours and is subject to the odds. Furthermore, it was found that under the given circumstances CIGS has no significant benefit compared to c-Si. That seems valid regardless of an increased irradiance onto the PV modules. Regarding the effect of an increased ground-albedo: Over a year for an increase of the reflectivity from 0.13 to 0.56 and considering the larger distance to the ground the gain is between 3 and 5 %. This benefit was found to be regardless of the PV module type.

The monthly sums of EY for PV modules located at the top most part of building facades is shown in Figures 6 and 7. Figure 6 shows only the results for crystalline silicon PV modules whereas Figure 7 shows the results for CIGS modules. In separate panels the yields are shown for facades oriented towards the three directions south, east and west. Furthermore, the two different ground-surface reflectivities (0.13 and 0.56) are directly compared for each case in the colours violet and yellow, respectively. The respective relative gains in EY in percent due to the higher value of albedo

Table 1: Yearly PV yield for the three orientations (south, east, west) and the two PV module technologies c-Si and CIGS. For the low albedo the yield is shown and otherwise the relative change of the yield compared to the lower albedo of the same PV technology or the same albedo and the other PV technology.

PV technology	**albedo**	**metric**		**South**	**East**	**West**
c-Si	0.13	$\sum$	[kWh/kWp]	697.3	526.0	531.2
	0.56	$\Delta_{0.13}$	[%]	3.8	5.0	3.4
CIGS	0.13	$\sum$	[kWh/kWp]	697.0	523.9	533.2
		$\Delta_{\mathrm{c-Si}}$	[%]	0.0	-0.4	0.4
	0.56	$\Delta_{0.13}$	[%]	3.6	5.0	3.3
		$\Delta_{\mathrm{c-Si}}$	[%]	-0.2	-0.4	0.3

are annotated above each pair of colour bars in the graphs.

For the majority of the months, especially for the east and west orientation, the gain with an increased albedo is around 3 – 5 %. Though for a south facing facade the gain from autumn until spring is only between 1 and 2 %. In contrast, during summer the increase goes up to 8 %, which is remarkable considering the already quite large yields in that time of the year. For this latitude it seems that during the early summer months of June and July overall more irradiance reaches to the east and west facing PV modules compared to ones with orientation to the south. However, in any other month of the year the south facing facade is superior to any other orientation.

Overall, CIGS technology seems to deliver a better EY by 1 – 5 % compared to c-Si for a south oriented PV system in all scenarios. The only exception is May for an unknown reason. For the other facade orientations CIGS seems to perform worse than c-Si from around April till September. During the other months the results show the opposite.

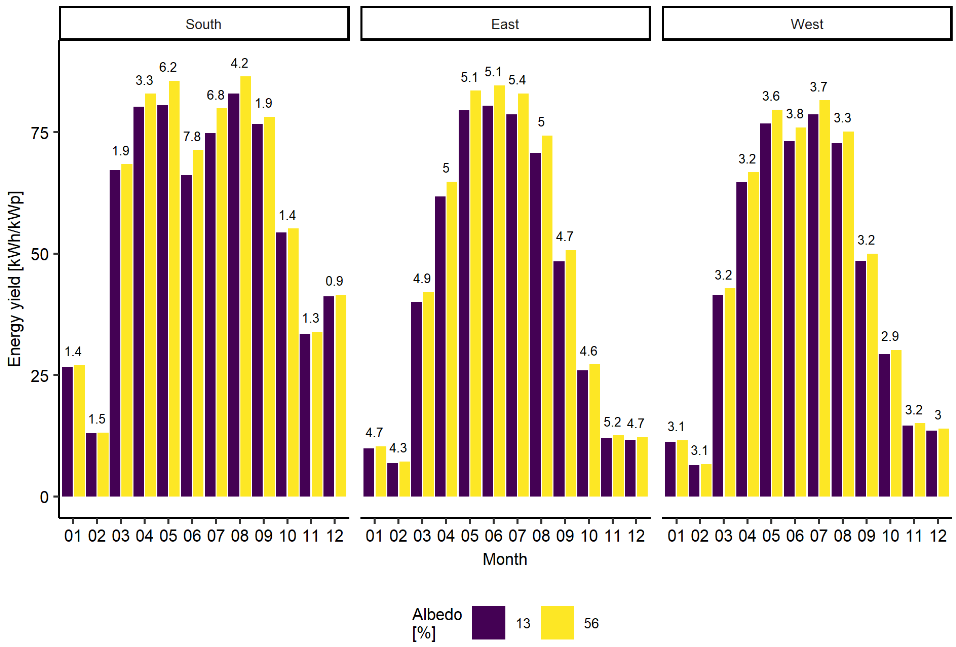

Figure 6: Monthly PV-yield inside a street canyon with a width to height ratio of 1 for crystalline silicon PV modules on south, east and west facing facades, respectively, and the gain [%] due to increased ground-albedo to 0.56 compared to a ground-albedo of 0.13.

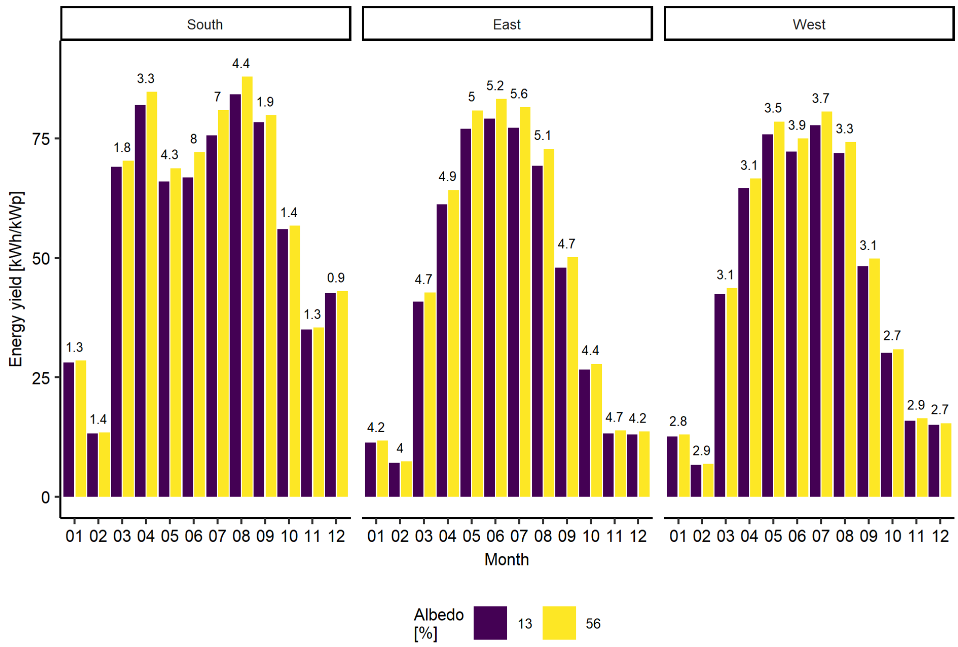

Figure 7: Monthly PV-yield inside a street canyon with a width to height ratio of 1 for CIGS PV modules on south, east and west facing facades, respectively, and the gain [%] due to increased ground-albedo to 0.56 compared to a ground-albedo of 0.13.

2 Publications and their relevance to the topic

2.1 List of publications

2.1.1 SCI-Publications

- Potential increase of solar irradiation and its influence on PV facades inside an urban canyon by increasing the ground-albedo (2018)
  `https://doi.org/10.1016/j.solener.2018.08.037`

- SEBEpv – New digital surface model based method for estimating the ground reflected irradiance in an urban environment (2020)
  `https://doi.org/10.1016/j.solener.2020.01.075`

2.1.2 Other Publication

- PVOPTI-RAY: OPTIMISATION OF REFLECTING MATERIALS AND PHOTOVOLTAIC YIELD IN AN URBAN CONTEXT (2017)
  `https://doi.org/10.4229/EUPVSEC20172017-6DO.11.4`

2.2 Relevance to the topic

Potential increase of solar irradiation and its influence on PV facades inside an urban canyon by increasing the ground-albedo (2018) In this work, first, it is shown, that the state-of-the-art method for estimating the irradiation reflected from the ground is generally overestimated and not appropriate for application in an urban environment. Therefore, the initial hypothesis was confirmed as being valid. Then, the realistic amount of the reflected component in an urban canyon was estimated by two methods:

- Measurements inside a street canyon at the University of Natural Resources and Life Sciences, Vienna, Austria, which were thoroughly described in that work.

- Estimating the irradiation at arbitrary facade-points based on the known view-factors inside the canyon.

The measurements were used to investigate and compare two scenarios: the usual reflectivity of the road as well as the effect of a locally increased surface albedo. For estimating the irradiation on arbitrary facade-points, a model was developed, that takes advantage of the known view-factors. It considers multiple reflections up to the second degree, which is more than what is used in other models for computational reasons. Those estimates were further used in later work to assess the error of neglecting multiple reflections. The view-factors were determined using fish-eye images from various points inside the canyon. Finally, this model was used to estimate the portion of irradiation reflected onto a wall inside an urban canyon. The results proofed the relevance and importance of the present work and provided an estimate for the reflected component.

SEBEpv – New digital surface model based method for estimating the ground reflected irradiance in an urban environment (2020)

In this publication a new method was proposed to estimate the reflected irradiation component for the complex urban environment. The method was based on a GIS tool, SEBE (Lindberg et al., 2015), to calculate the irradiance on building surfaces. Thus, it allows to do calculations for often available raster data of dwellings (digital surface model). The new method allowed to calculate the reflected component more precisely than possible so far without the use of computationally intensive ray-tracing methods. However, multiple reflections were not implemented in this method. Therefore, the new method poses an underestimation of the reflected component. The various error sources were discussed and the validation using measured data was presented in that work.

PVOPTI-RAY: OPTIMISATION OF REFLECTING MATERIALS AND PHOTOVOLTAIC YIELD IN AN URBAN CONTEXT (2017) This conference paper contains a summary of the results from the project PVOPTI-ray. One of the important parts was the development of the new tool SEBEpv with the improved algorithm for the reflected component. However, results regarding the reflected component were based on an initial version of the algorithm that was still subject to improvement. Further results concern the thermal impact of BIPV/BAPV in the urban environment. Other results presented, that are not part of this work, were the impact of an increased ground albedo on the thermal comfort and the air temperature inside the urban environment.

3 Conclusion

This work initially claimed that the currently used models for the reflected irradiance component are not suitable for estimating its value on building facades in a street canyon. Setting up measurements in between two buildings at the University of Natural Resources and Life Sciences (BOKU) in Vienna, Austria, aimed at determining the amount of reflected irradiation at facades. In addition, the ground's albedo was temporary increased to study its effect. Using fish-eye images from various perspectives inside the street canyon allowed to establish a simple model to estimate the reflected component amongst the total irradiance received at a south-facing wall.

The measurements paired with this simple, but effective model proofed the claimed hypotheses and conclusions were drawn as follows: Indeed, the common modelling approach is overestimating the irradiance reflected onto a facade inside a street canyon. Secondly, the reflected component is in practice still large enough to be significant for the total electricity production, even inside cities. In comparison to asphalt, increasing the albedo to a rather unrealistic value of 0.77 on an area of only 30 m^2 increased the total irradiance by around 13 % at a south-facing wall point at 3.5 m above ground during a 16-days examination period. The estimated PV yield would be increased by about the same value under these conditions. The simple model based on view-factors confirmed this result. Furthermore, using the model showed that increasing the reflectivity to 0.5 on the complete street compared to asphalt still results in a PV yield gain by about 7 % for a wall point at 12 m above ground (i.e. almost top floor of a usual building) (Revesz et al., 2018).

Extensive literature research also showed that there is a need for accurate simulation tools, especially for the complex urban environment. That led to improve an existing tool with regard to the irradiance reflected from the ground. The new tool was named SEBEpv emphasising some novelty added to the original tool SEBE (Lindberg et al., 2015). Its new algorithm for the reflected component uses the trick of calculating shadow pattern onto the inverse of the DSM, i.e. ground-shadows onto building walls. Further improvement was accomplished by implementing a spatially variable ground-albedo and considering the actual irradiance received at a spot on the ground. The latter was also a necessity to avoid the assumption of an unshaded ground, that receives GHI as if unobstructed and reflects the respective radiation. Without multiple reflections being considered, SEBEpv was validated at the example of a south-facing facade inside a street canyon in Vienna, Austria. In that study, the irradiance was underestimated with a negative bias of 7 % and a standard deviation of about 29 W/m^2. However, a part of the bias error was attributed to a rather low number of sky-patches that were used for the shadow casting (Revesz et al., 2020).

Further validation of SEBEpv may be advised, using measured data from other locations as well as measurements of the reflected irradiation at the top of building facades. Also, measurements for other facade orientations are recommended. While SEBEpv was proven to be a very suitable tool for solar resource assessment on building facades in the urban environment, a few recommendations of improvement were identified. In the future, tuning on the computational efficiency is another point for improvement which can make the tool to be easily applied by any interested citizen without the need of powerful hardware (Revesz et al., 2020).

4 Publications

4.1 Publication I

Potential increase of solar irradiation and its influence on PV facades inside an urban canyon by increasing the ground-albedo
`https://doi.org/10.1016/j.solener.2018.08.037`

Solar Energy 174 (2018) 7–15

Contents lists available at ScienceDirect

Solar Energy

journal homepage: www.elsevier.com/locate/solener

Potential increase of solar irradiation and its influence on PV facades inside an urban canyon by increasing the ground-albedo

Michael Revesz[a,b,*], Sandro Michael Oswald[b], Heidelinde Trimmel[b], Philipp Weihs[b], Shokufeh Zamini[a]

[a] AIT Austrian Institute of Technology GmbH, Center for Energy, Photovoltaic Systems, Giefinggasse 2, 1210 Vienna, Austria
[b] University of Natural Resources and Life Sciences, Department of Water-Atmosphere-Environment, Institute of Meteorology, Gregor-Mendel-Straße 33, 1180 Vienna, Austria

ARTICLE INFO

Keywords:
Photovoltaics
Facade-integrated photovoltaics
Ground-reflected irradiance
Urban canyon

ABSTRACT

Due to the large demand for electricity in cities, photovoltaic (PV) installations inside the urban environment will increase in the near future. It is known that the yield of PV systems on facades can be increased by increasing the ground-albedo. White surfaces are also proposed for urban heat island mitigation. Thus, increasing the ground-albedo inside the urban environment has multiple advantages. However, solar potential simulation tools are not yet designed for simulating in an urban canyon. The ground-reflected irradiance is either neglected or the known approximation is applied. The potential contribution of ground-reflected irradiance to the electricity production of PV facades in an urban canyon is not yet investigated. Therefore, measurements were made in a street canyon to show the potential effect of an increased ground-albedo on the power output of south-facing, vertically mounted PV modules and the total in-plane irradiance. Further, the potential increase of PV yield on a reference point was estimated, when asphalt on an approximately 15 m wide street canyon was replaced with a highly reflective concrete and an albedo of 0.5. For the latter case, at a wall point 12 m above ground and with a ground view factor of 0.16, it was found that during an eleven days reference period in August 2016, in Vienna, the PV yield increases by 7.3%.

1. Introduction

Today, many governments strive to increase the use of renewable energies, particularly photovoltaics (PV). Given that most electricity is consumed in cities, it is proposed that PV systems will play a more important role in urban environments in the future. Decentralised systems can then provide electricity close to where it is consumed (Fechner et al., 2016; IEA, 2014; Krawietz et al., 2016). In Vienna, for example, the city council already addressed those topics and developed strategies to increase the amount of PV installations in the city (Dvorak, 2016).

In the past, several institutions have created tools to estimate the solar potential of residential areas (Freitas et al., 2015). In early and simple solar potential estimations only roofs were considered (Freitas et al., 2015). The urban solar potential algorithm SOL was one of the first algorithms to address the solar potential on walls in addition to roofs. However, ground reflections are neglected in SOL (Redweik et al., 2013). Only more recently have tools been developed that include the ground-reflected irradiance on facades, e.g. SEBE (Solar Energy on Building Envelope) (Lindberg et al., 2015).

Usually, the ground-reflected irradiance is estimated by the term $1/2\,\rho\,G\,(1\text{–}\cos\beta)$, where ρ is the albedo, β is the tilt of the receiving plane and G is the global horizontal irradiance. This approach assumes an isotropic reflecting and infinitely large ground surface and is argued to be sufficiently accurate (Ineichen et al., 1990). Nevertheless, the authors of this paper argue that this approach overestimates the contribution of ground-reflected irradiance to the total irradiance on facades inside an urban canyon. The obvious reason is that the ground view factor is significantly limited inside an urban canyon, which is inconsistent with the assumption of an infinitely large ground area.

Previous studies regarding the effect of ground-albedo on the performance of PV modules focus on either the spectral effects of albedo or the effect of snow (Andrews and Pearce, 2013, 2012; Brennan et al., 2014). Additional potential PV yield due to increasing ground-albedo has not yet been addressed.

In the meantime, urban climatologists have been researching methods to mitigate urban heat island effects. Adding white surfaces to cities is one of many suggested methods to reduce the heat island effect

* Corresponding author at: AIT Austrian Institute of Technology GmbH, Center for Energy, Photovoltaic Systems, Giefinggasse 2, 1210 Vienna, Austria.
E-mail address: revesz.michael@gmail.com (M. Revesz).

https://doi.org/10.1016/j.solener.2018.08.037
Received 19 June 2018; Received in revised form 11 August 2018; Accepted 16 August 2018
0038-092X/

in urban environments (Mohajerani et al., 2017; Santamouris, 2014; Taha, 1997). Technological developments on reflective pavements and their effects are discussed in Qin (2015a), Santamouris (2013). Positive and negative effects of reflective pavements inside urban canyons are discussed as well. Examples include their effect on cooling and heating loads in buildings (Yaghoobian and Kleissl, 2012) and their effect on the thermal and visual comfort of pedestrians (Rosso et al., 2016). Preliminary results of a recent case study within the PVOPTI-Ray project also show that increasing the ground-albedo up to 0.56 does not significantly effect human thermal comfort (Revesz et al., 2017).

Considering the reported benefits of an increased albedo of the ground surface to the urban climate, the shortcoming in irradiance estimation for predicting the PV power output in an urban environment, as described before, leads to two important questions: How much irradiance is realistically reflected from the ground onto a wall inside an urban canyon? And how much does increasing the ground-albedo increase the solar irradiation and thus increase the yield of PV facades inside an urban canyon? This work attempts to address these questions.

For this purpose, gains were measured at the University of Natural Resources and Life Sciences (BOKU) in Vienna during August 2016. In addition, the potential effect of replacing asphalt with highly reflecting concrete on the total irradiance inside an urban canyon was estimated.

2. Methods

Measurements were made to investigate the potential increase of electricity production of vertically mounted PV modules due to an increase in ground reflectance. Those measurements validate a simple method to estimate the ground-reflected irradiance on a wall point. In addition, simulations were performed assuming a more reflective ground surface material. Whenever irradiance was estimated the diffuse sky irradiance and the irradiance reflected from the ground or the building facade (except for the glass facade) were assumed to be isotropic.

2.1. Measurements inside an urban canyon

The area between two buildings of the University of Natural Resources and Life Sciences (BOKU) in Vienna, Austria, was used for measurements. Fig. 1 shows the surrounding of the measurement site. The location "C" marks the position of measurement equipment inside the street canyon. Facing south, three vertical multicrystalline silicon PV modules and one vertical irradiance (G_v) sensor were mounted. Further, the horizontal irradiance (G_h), ambient air temperature (T_a), and module temperature (T_m) on each of the PV modules' backside were measured. Fig. 2 shows the installed equipment, which was mounted about 3.5 m above ground. BP solar SX 10 M modules were used and their short circuit current (I_{sc}) was measured. The vertical and horizontal irradiance sensors were EMS 11 which are silicon diode irradiance sensors with a calibration error of max. 7% (EMS Brno, 2016) and are expected to have a similar spectral response as the PV modules. The data-logger for those two irradiance sensors had a resolution corresponding to about $1.4\,W\,m^{-2}$ and $1.8\,W\,m^{-2}$ respectively. Within this work the position of the vertical irradiance sensor is referred to as "wall point".

On the roof of Schwackhöfer-Haus the global horizontal irradiance (G) and the direct normal irradiance (DNI) were measured, using a EKO MS-802 pyranometer and Kipp & Zonen CHP-1 pyrheliometer, respectively. Their position is marked in Fig. 1 with "R". The measurements of both devices were compared to measurements within the ARAD network (Olefs et al., 2016). The diffuse horizontal irradiance (DHI) component was estimated from G and DNI. All values were measured at 5 s intervals and aggregated by the data-loggers to record a 1-minute mean value. For the evaluation of the gain the data was further aggregated to 5-minute mean values.

The ground-albedo was measured 80 cm above the ground using two silicon diode irradiance sensors of type EMS 11 (by EMS Brno), one oriented upwards and one downwards (see Fig. 2(a)). In this configuration the influence of the equipment itself on the reflected radiation is negligible, while providing a good estimate of ground-albedo of a brighter surface with limited surface area. Further, Apogee SN-500 were used to determine the albedo of the non-glass facade and for occasional measurement of incoming irradiance onto the centre point of the plastered facade, opposite of the PV modules.

Measurements were performed for a period of one month in August 2016. During the measurements, the "low ground-albedo" condition was for asphalt in between the two buildings with ρ = 0.13. Several times, "high ground-albedo" measurements were made by placing

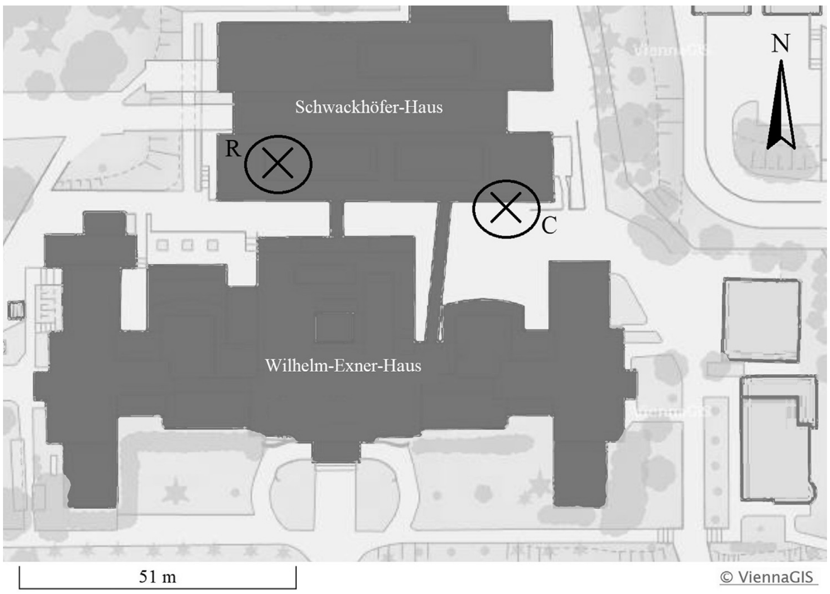

Fig. 1. Measurement site at University of Natural Resources and Life Sciences (BOKU) in Vienna between Schwackhöfer-Haus and Wilhelm-Exner-Haus (lat. 48.237 N, lon. 16.332 E). The location of the PV modules and the vertical irradiance sensor in the canyon is labelled with "C" and the location for the irradiance measurement on the roof is labelled with "R". Source of base-map: www.wien.gv.at/viennagis/.

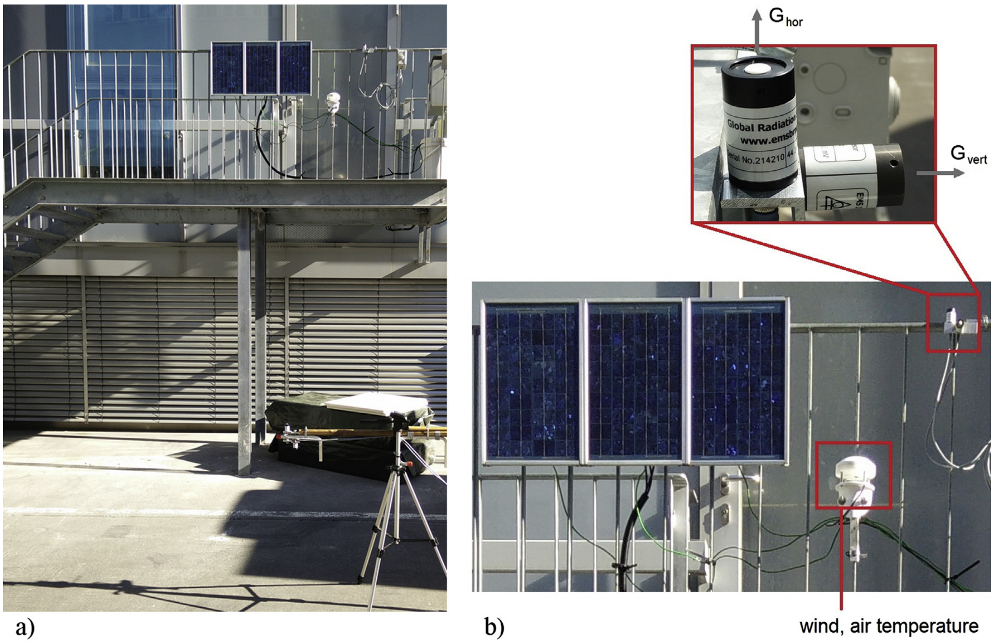

Fig. 2. Measurement equipment: (a) mounting in the canyon in front of Schwackhöfer-Haus; (b) enlarged view on the measurement equipment (PV modules, irradiance sensors, wind speed, wind direction and air temperature).

Fig. 3. View of south-facing PV modules taken with a camera with a fish-eye lens. The placement of the white Styrofoam panels in front of the PV modules is shown.

30 m^2 of white painted Styrofoam panels with $\rho = 0.77$ on the asphalt in front of the PV modules (see Fig. 3).

2.2. Evaluation of the irradiance gain

In this study the ground-albedo was temporary altered at the same location. Due to temporal variations of the humidity, aerosol content, dust and clouds the irradiance levels varied with time (Ineichen and Perez, 2002; Remund et al., 2003). Therefore, it was required to use a reference irradiance for comparison with the measured vertical irradiance during different days and to evaluate the gain due to different ground-albedos.

For this purpose, the vertical irradiance in the canyon (at the position of the vertical irradiance sensor) was estimated from the irradiance components that were measured on the roof. As suggested by e.g. Qin (2015b) the contribution from multiple reflections was considered, herein up to the second degree. Thus, the total vertical irradiance was calculated, using:

$$G_v = G_{sky} + \sum_i G_{gnd} \cdot f_{gnd,i} \cdot \rho_{gnd,i} + G_{b1} \cdot f_{b1} \cdot \rho_{b1}, \quad (1)$$

where the first term G_{sky} refers to the direct and diffuse irradiance from the sun incident onto the wall point, the second term refers to the radiation reflected from the ground and the third term refers to the radiation reflected from the building on the opposite side of the canyon. In the second term a summation over sub-surfaces of the ground with different ground-albedos is used, if applicable, and it consists of the irradiance G_{gnd} received by the ground, the view factor $f_{gnd,i}$ of the ground's sub-area i that is visible to the wall point and the albedo $\rho_{gnd,i}$ of the i-th ground's surface. The variables in the third term with subscript b1 refer to the respective variables for the building opposing the PV modules. Here f_{b1} is the view factor of building b1 as seen by the wall point and ρ_{b1} is the albedo of the facade on building b1.

The irradiance received by the wall point from the sky is simply

$$G_{sky} = DNI \cdot \cos\theta + DHI \cdot f_{sky}, \quad (2)$$

where θ is the solar angle of incidence on the tilted (in this case vertical) plane and f_{sky} is the sky view factor of the receiving wall point.

The irradiance received by the building b1 consists of contributions from the sky, the reflections from the ground (summation over different ground surfaces with different albedo, if applicable) and from the building with the receiving wall point (subscript b2) and is written as:

$$G_{b1} = G_{b1,sky} + \sum_i G_{gnd,sky} \cdot f_{b1,gnd,i} \cdot \rho_{gnd,i} + (G_{b2,sky} \cdot \rho_{b2}) \cdot f_{b1,b2}, \quad (3)$$

where $G_{b1,sky}$ is the irradiance received by building b1 from the sky, $G_{gnd,sky}$ is the irradiance received by the ground surface from the sky, $f_{b1,gnd,i}$ is the view factor of the ground area i that is visible to the building b1, $\rho_{gnd,i}$ is the albedo of the ground area i, $G_{b2,sky}$ is the irradiance received by the building b2 from the sky, ρ_{b2} is a specular reflectance of the glass facade and $f_{b1,b2}$ is the view factor of the building b2 that is visible to the building b1. The following equations show the calculation of the irradiance onto the three relevant surfaces used in Eq. (3):

$$G_{b1,sky} = DHI \cdot f_{b1,sky}, \tag{3a}$$

$$G_{gnd,sky} = DNI \cdot \cos\theta_{gnd} \cdot sh + DHI \cdot f_{gnd,sky}, \tag{3b}$$

$$(G_{b2,sky} \cdot \rho_{b2}) = DNI \cdot \cos\theta_{b2} \cdot \rho_{b2,dir} + DHI \cdot f_{b2,sky} \cdot \rho_{b2,dif}, \tag{3c}$$

where $f_{b1,sky}$ is the sky view factor of b1, θ_{gnd} is the solar angle of incidence onto the ground, *sh* is a factor accounting for the fraction of shadow on the ground surface, $f_{gnd,sky}$ is the sky view factor of the ground, θ_{b2} is the solar angle of incidence onto the facade of b2, $f_{b2,sky}$ is the sky view factor of b2 and $\rho_{b2,dir}$ and $\rho_{b2,dif}$ are parameters referring to the specular reflectance for diffuse and direct irradiance from b2.

At last, the irradiance onto the ground's surfaces is calculated similarly to Eq. (3) as:

$$G_{gnd} = G_{gnd,sky} + G_{b1} \cdot f_{gnd,b1} \cdot \rho_{b1} + (G_{b2,sky} \cdot \rho_{b2}) \cdot f_{gnd,b2}, \tag{4}$$

where $G_{gnd,sky}$, G_{b1} and the term $(G_{b2,sky} \cdot \rho_{b2})$ are as calculated according to the Eqs. (3a), (3b) and (3c), respectively and $f_{gnd,b1}$ and $f_{gnd,b2}$ are the view factor of the buildings b1 and b2, respectively, that are visible to the ground.

All values of surface albedo were determined from measurements, except for the specular reflectance of the glass facade. The specular reflectance $\rho_{b2,dir}$ and $\rho_{b2,dif}$ were determined by linear regression to measured data and are the only parameters that had to be determined by other means than measurement. The view factors were determined from fish-eye images in a central point of the respective surface relative to the canyon or the position of the reference wall point. Further, it was assumed that the view factors are representative for the whole surface, although it is known that the view factors depend on the exact location on a surface. The shadow factor *sh* for the ground is set to 1 when the wall point is known to be in shadow. Otherwise, it is estimated to be around 0.5 for most of the time. For simplicity the shadow factor is assumed to be constant.

To calculate the gain of the irradiance at the wall point, the irradiance at the wall point was estimated for each of the two ground-surface conditions as described in Section 2.1 and using Eq. (1). The respective values for the ground's albedo were used in the estimations. The gain of the irradiance at the wall point (g_G) is then calculated as:

$$g_G = \frac{G_{v,sim}(\rho_{high})}{G_{v,sim}(\rho_{low})}, \tag{5}$$

where $G_{v,sim}(\rho_{high})$ is the vertical irradiance simulated at the wall point for the condition with the higher ground-albedo and $G_{v,sim}(\rho_{low})$ is the vertical irradiance simulated at the wall point for the condition with the lower ground-albedo. In addition, the gain is presented as the quotient of the respective irradiation over a given time.

2.3. Evaluation of the PV power gain

The gain in PV power output for a vertical, south-facing PV panel was evaluated by calculating the PV power at the PV module's maximum power point. As reference and for the assessment of the estimations' quality the PV power was calculated using the measured short circuit current. First, the effective irradiance was calculated according to King et al. (2004) as:

$$G_e = \frac{I_{sc}}{I_{sc,0} \cdot [1 + \alpha_{Isc} \cdot (T_m - T_0)]}, \tag{6}$$

where G_e is the effective irradiance, I_{sc} is the measured short circuit current, $I_{sc,0}$ is the short circuit current at reference condition of 1000 W/m^2 and 25 °C, α_{Isc} is the temperature coefficient of the short circuit current, T_m is the module temperature (measured at the back of the PV module), and T_0 is the reference temperature of 25 °C. Results referring to this method are called "measured".

Afterwards, the PV power was calculated according to the following formulas by King et al. (2004):

$$I_{mp} = I_{mp,0} \cdot [C_0 \cdot G_e + C_1 \cdot G_e^2] \cdot [1 + \alpha_{Imp} \cdot (T_m - T_0)], \tag{7}$$

$$V_{mp} = V_{mp,0} + C_2 \cdot N_s \cdot \delta(T_m) \cdot ln(G_e) + C_3 \cdot N_s \cdot [\delta(T_m) \cdot \ln(G_e)]^2 + \beta_{Vmp} \cdot (T_m - T_0), \tag{8}$$

$$P_{mp} = I_{mp} \cdot V_{mp}, \tag{9}$$

where I_{mp} and V_{mp} are the current and the voltage of the PV module at its maximum power point, $I_{mp,0}$ and $V_{mp,0}$ are the current and the voltage at the modules maximum power point under a reference condition of 1000 W/m^2 and 25 °C, α_{Imp} and β_{Vmp} are the temperature coefficients for the current and the voltage at the maximum power point, C_0, C_1, C_2 and C_3 are empirical coefficients determined for the PV module, $\delta(T_m)$ is the thermal voltage at T_m, N_s is the number of cells connected in series in a PV module, and P_{mp} is the electric power of the PV module at its maximum power point. All relevant PV module related coefficients are taken from a database available on https://sam.nrel.gov/libraries (Gilman, n.d.), except of $I_{sc,0}$, $I_{mp,0}$ and $V_{mp,0}$, which were determined in a laboratory for the PV modules in use.

Eqs. (7) and (8) were simplified by neglecting the influence of airmass on the spectrum and the losses with increased angle of incidence. Further, the module backside temperature was used as the cell temperature. These effects will cancel as the ratio of two PV powers will be calculated for evaluating the gain.

For the evaluation of the gain in PV power, however, the effective irradiance in Eq. (6) was calculated from estimated irradiance at the wall point according to $G_e = G_v/(1000\ \mathrm{W/m^2})$. The irradiance used in this case was estimated using the irradiance components measured on the roof and as described in Section 2.2. Those values of PV power are referred to as being "simulated".

Finally, the PV power gain due to different ground-albedos was calculated as:

$$g_{PV} = \frac{P_{mp}(\rho_{high})}{P_{mp}(\rho_{low})}, \tag{10}$$

where $P_{mp}(\rho_{high})$ is the PV power resulting from the high albedo compared to $P_{mp}(\rho_{low})$, which is resulting from the lower albedo.

In addition, the gain is expressed as the quotient of the respective PV yields over a specified period. The yield is the energy produced (in units of Wh) divided by the nominal peak power (in units Wp) of the PV module under reference condition. Providing PV yields makes the results comparable for arbitrary PV installations. When PV power is stated in the results-section, the average value of the three PV modules was calculated and multiplied with the average peak power of the three PV modules under reference condition (9.2 W).

2.4. Evaluating the effect of highly reflective concrete

The measurements described previously show the impact of ground-reflected irradiance inside an urban canyon. However, they represent unrealistic conditions as the highly reflective surface had limited ground coverage. Therefore, the impact of highly reflective concrete which covers the entire ground surface of the urban canyon was estimated.

The new scenario was the same canyon as for the measurements described above. The albedo for the asphalt was 0.13 and the albedo of the highly reflective concrete was assumed to be 0.50 (Krispel et al., 2017). The irradiation and the PV yield on a south-facing wall were estimated as described in Section 2.2 for a wall point 3.5 m above ground, corresponding to the position of the vertical irradiance sensor in the canyon, and for a wall point about 12 m above ground. The latter point was chosen because this is the point at the centre of the facade, for which fish-eye images were taken. Further, the installation of PV modules at that height and above is reasonable.

The irradiance data used was from the measurements described above. The irradiation and PV yield were estimated for the period 17. to 28. August 2016. In this period the sky conditions were clear sky, scattered clouds, as well as two days of overcast sky.

3. Results

3.1. Accuracy of the model

In the following the accuracy of the overall model and the two models for the irradiance onto the ground surface and onto a central point on the facade of the building b1, opposite of the wall point, are presented. In addition to the standard deviation and the mean bias error of the modelled data and the available measured data, also the deviation between the total irradiation over the period of available data is stated.

The estimated irradiance onto the building b1, calculated using Eq. (3), has a standard deviation of $\sigma = 8.0\,\mathrm{W\,m^{-2}}$ and a mean bias error of $-2.4\,\mathrm{W\,m^{-2}}$. The difference to the total measured irradiation is -4.1%. For the estimated irradiance onto the ground-surface the modelled (see Eq. (4)) compared to the measured data has a standard deviation of $\sigma = 38\,\mathrm{W\,m^{-2}}$ and a mean bias error of $3.3\,\mathrm{W\,m^{-2}}$. In this case, the difference to the total measured irradiation is 2.0%.

The final model for the irradiance onto the wall point of interest (see Eq. (1)) exhibits a standard deviation of $\sigma = 20\,\mathrm{W\,m^{-2}}$ and a mean bias error of $-5.0\,\mathrm{W\,m^{-2}}$. Over the period from 13. until 28. August 2016 the total estimated irradiation is 4.9% lower than the measured irradiation. The comparison of the estimated data with the measured data is shown in Fig. 4, where the points with residuals larger than the residuals' standard deviation are marked as dark-orange triangles. The points with extreme deviation (see the area at the bottom of the figure) relate to points during the transition when the wall point becomes shaded or the shading ends.

For comparison, the irradiance onto the wall point was estimated ignoring second degree reflections. In that case, the standard deviation was $\sigma = 21\,\mathrm{W\,m^{-2}}$ and the mean bias error $-8.5\,\mathrm{W\,m^{-2}}$. More significant was the difference for the total estimated irradiation, which is 6.9% lower than the measured irradiation.

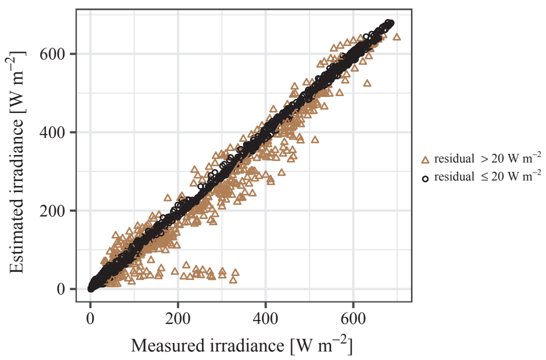

Fig. 4. Estimated irradiance versus the measured irradiance. Dark-orange triangles depict data points those absolute residual is larger than the residual standard deviation of the model.

3.2. Measurements

The results for the evaluation of the measurements are presented here. Useable data is available from 13. to 28. August 2016. For this period the irradiance was estimated once for a ground with bare asphalt and with an albedo of 0.13. In addition, the irradiance was estimated for the same period with Styrofoam panels with an albedo of 0.77 being placed on the ground, as described in Section 2.1. Within this period the total irradiation onto the south-facing wall point increased from $36.6\,\mathrm{kWh\,m^{-2}}$ to $41.7\,\mathrm{kWh\,m^{-2}}$ due to the described change of the ground's albedo. This corresponds to an increase by 13.8%. Looking only at a four-days period of clear sky, from 25. to 28. August 2016, by increasing the ground's albedo the irradiation in that period increased by 12.0% from $12.0\,\mathrm{kWh\,m^{-2}}$ to $13.4\,\mathrm{kWh\,m^{-2}}$.

For the PV modules the estimated gain in energy yield due to increasing the ground's albedo is 3.15 Wh/Wp for the period 13. to 28. August 2016. This corresponds to a gain by 12.8%. For the four-days period of clear sky the energy yield is estimated to increase by 1.19 Wh/Wp, which is a gain by 11.3%. The relative gain in PV yield is slightly lower than the gain in irradiation. This is because of the PV module's temperature coefficient. Increased irradiation causes a higher temperature inside the PV module and thus, reduces the PV module's power.

Fig. 5 shows the measured irradiance on the wall point for 25. to 28. August 2016 in comparison with the estimated irradiance for the cases of low ground-albedo (asphalt) and the increased ground-albedo. During the first two days in this figure, the ground surface is only asphalt. Thus, the estimated irradiance for the same ground condition corresponds well to the measurement. Similarly, for the other two days the measured irradiance is well represented by the estimated irradiance for the respective ground-surface condition, where white Styrofoam was placed on the ground. Though, one can also see that during morning and afternoon the deviation between measurement and estimation is larger than around noon. Fig. 6 shows the gain in irradiance for those four days of clear sky; Fig. 6(a) the absolute gain and (b) the relative gain. As expected, the relative difference is smaller the higher the portion of direct irradiance.

In Fig. 7 the increase of PV power due to the two different conditions of ground-albedo is shown. The corresponding curves of the simulated PV power for each of those two conditions are shown in Fig. 7(a). In addition, the "measured" PV power, which was calculated based on the measured I_{sc}, is shown in Fig. 7(a). The gain g_{PV}, which was calculated from the simulated PV power for the condition with lower albedo and the condition with larger albedo, is shown in Fig. 7(b).

3.3. Effect of highly reflective concrete

In the following, the potential effect of highly reflective concrete compared to asphalt is presented. The two scenarios that were simulated are described in Section 2.4. Based on irradiance measurements between 17. and 28. August 2016 the following results were found when increasing the ground's albedo: The total irradiation on a south-facing wall point 12 m above ground was estimated to increase by 7.4% compared to a total of $37.5\,\mathrm{kWh\,m^{-2}}$ for asphalt. The PV yield was estimated to increase for the same case by 7.3% compared to the case of asphalt with a total yield of 32.8 Wh/Wp.

For the wall point in only 3.5 m above ground the gain is significantly larger, as expected. It is around 20% compared to asphalt as a ground-surface, for which the total irradiation is $28.1\,\mathrm{kWh\,m^{-2}}$ and the PV yield is 24.2 Wh/Wp. Nevertheless, at a wall point in 12 m above ground and even with asphalt, the PV yield would still be larger than at the lower wall point with increased ground-albedo.

Figs. 8 and 9 show the results for each day in this period. In Fig. 8(a) one can see the PV yield for each of the assumed ground-albedos, on the left in 12 m above ground and on the right in 3.5 m above ground.

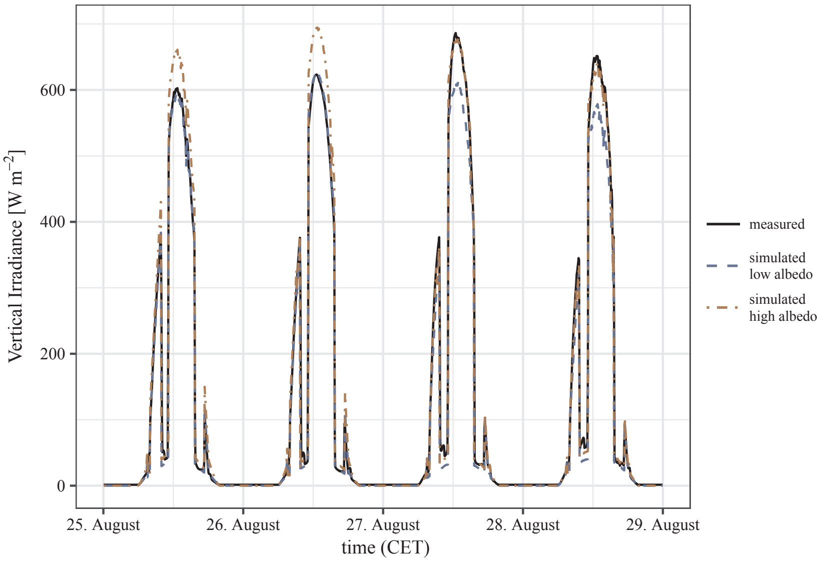

Fig. 5. Comparison of measured vertical irradiance with estimated irradiance for different conditions of the ground's albedo. The low albedo is 0.13 for asphalt during 25. – 26. August 2016 and the high albedo is asphalt with partial Styrofoam cover with an albedo of 0.77 during 27. – 28. August 2016 in Vienna.

Fig. 8(b) shows the resulting absolute gain in PV yield due to increasing the ground-albedo from 0.13 to 0.50. A comparison of days with overcast sky and clear sky shows that the benefit of the higher albedo for overcast sky is around half in 12 m above ground, despite the yield being only a quarter to a third. In Fig. 9 the absolute gain in irradiation is shown for those two wall points and shows similar results as the PV yield. This result clearly shows that the potential gain in PV yield inside an urban canyon is significant if bright concrete is chosen for the ground surface in cities.

4. Discussion

The chosen method for evaluation of the gain of vertical irradiance and PV power due to an increased ground-albedo seems reasonable under the present conditions. An advantage was the use of fish-eye images, taken from various surfaces inside the urban canyon and the availability of measurement data for irradiance onto ground of building surfaces. This allowed estimations with only a limited amount of model-calibration being required.

The rather large standard deviation of the residuals with 20 W m^{-2} for the wall point of interest can clearly be attributed to the transition

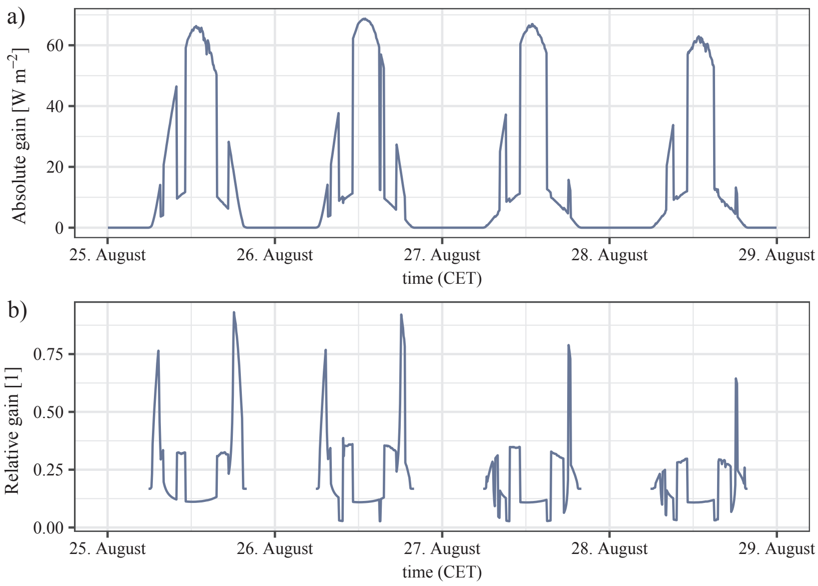

Fig. 6. Increase of irradiance on a south-facing wall point due to an increase of the ground's albedo. Based on estimated irradiance values in Vienna. 25. – 26. August 2016: asphalt with an albedo of 0.13; 27. – 28. August 2016: Styrofoam with an albedo of 0.77 on asphalt. a) Absolute difference; b) relative difference (gain).

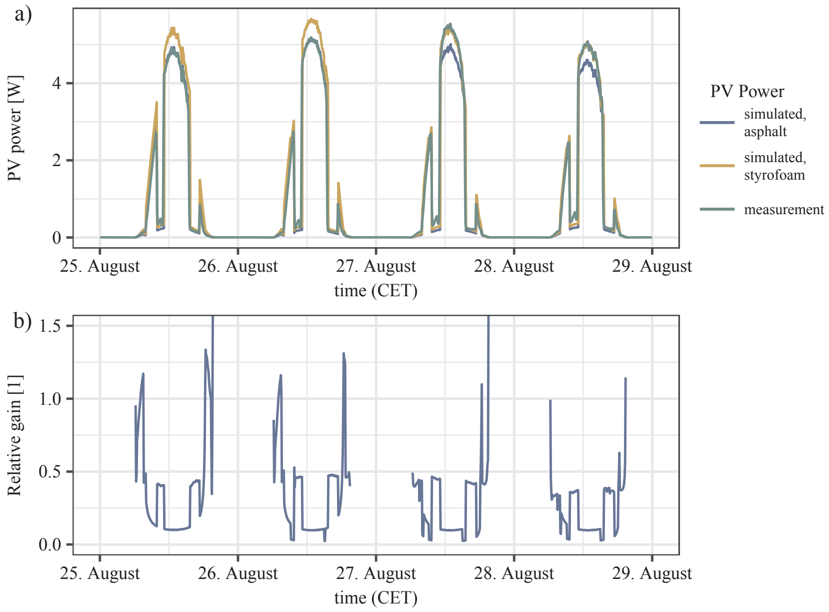

Fig. 7. Comparison of the power of a vertical, south-facing PV module (nominal power of 9.2 W) for different conditions of ground-albedo. The low albedo is 0.13 for asphalt (measured 25. – 26. August 2016 in Vienna) and the higher albedo is asphalt with partial Styrofoam cover with an albedo of 0.77 (measured 27. – 28. August 2016). (a) Power output calculated from estimated vertical irradiance (blue and orange) and from measured I_{sc} (green); (b) relative gain.

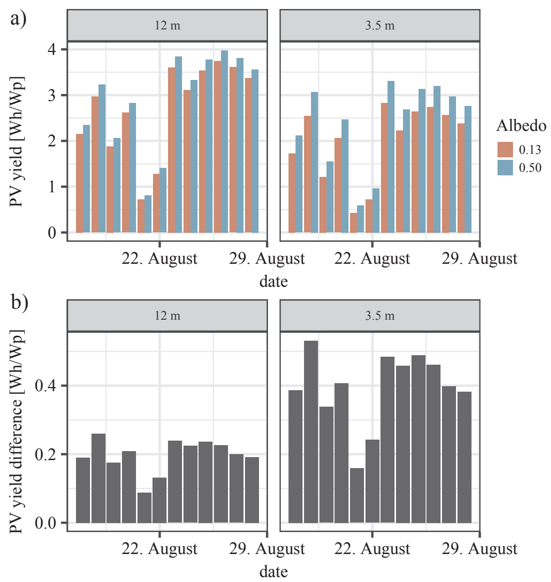

Fig. 8. Estimated PV yield on a south-facing wall point for a ground-albedo of 0.13 and 0.50 and the resulting gain. Based on irradiance measurements in Vienna, between 17. and 28. August 2016. Left: at wall point in 3.5 m above ground; right: in 12 m above ground. (a) Absolute PV yield; (b) resulting gain.

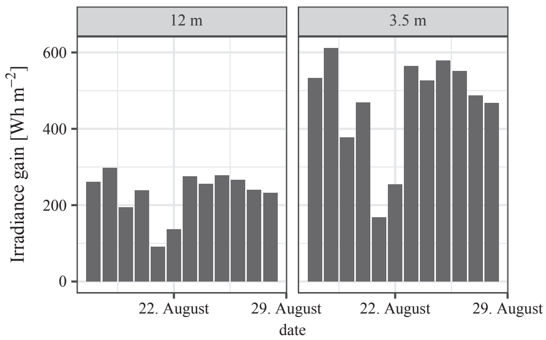

Fig. 9. Increase of irradiation on a south-facing wall point in 3.5 m above ground (as for the measurements) and in 12 m above ground, due to an increase of the ground-albedo from 0.13 to 0.50. Estimated results for an urban canyon in Vienna, based on irradiance measurement between 17. and 28. August 2016.

between sunlit and shaded. For the estimations it was not possible to clearly define this transition phases. Though, the definition of shading was required as the pyranometer and pyrheliometer on the roof, which were used for estimating the irradiance in the canyon, were not shaded in contrast to the irradiance sensor and PV modules in the canyon.

In Section 3.2 it was noted that in the morning and the afternoon the deviation between measurement and estimation is relatively larger than around mid-day. It is believed this is due to the difficulty of accurately estimating the portion of ground that is shaded by the building in the south of the canyon. It is not clear how much this is contributing to the error. However, any bias from the estimated portion of shadow on the ground, plus the neglected contribution from multiple reflections of higher order than two, can only be in the magnitude of the stated 5% bias of the total irradiation between 13. and 28. August 2016. Overall, this method provides reasonable results and deems suitable for the evaluation of the measurement and further estimations.

For future studies, it is recommended to analyse different scenarios, especially regarding different urban geometries. Those include different ratios of building height to street width, for which the portion of shadow on the ground is the main influence, and different canyon orientations. Notably PV systems that are oriented easterly or westerly are expected to benefit from an increase of the ground-albedo, compared to south oriented PV modules in an east-west oriented canyon. That is because when the sun azimuth corresponds to the canyon direction and the angle of incidence on the PV modules becomes small, most of the electricity will be generated from the diffuse sky irradiance and the radiation reflected from the ground. At that time, the ground will have the lowest amount of shadow and the global horizontal irradiance will be rather large. Increasing the ground-albedo will then significantly increase the contribution of ground reflected irradiation to the PV yield. Altering the building height to street width ratio changes the fraction of shadow on the ground, too, and thus, has an impact on the total radiation reflected from the ground.

5. Conclusion

Measurements inside an urban canyon at the site of the University of Natural Resources and Life Sciences (BOKU) in Vienna, Austria, were used to show the increase of PV yield by increasing the ground's albedo. During several days in August 2016, 30 m^2 of white painted Styrofoam panels with an albedo of approximately 0.77 were placed on the ground in front of a vertical irradiance sensor and PV-modules, about 3.5 m above ground.

The total PV yield during a period of 16 days was shown to increase by almost 13% under the stated increase of the ground's albedo. During a four-days period of clear sky the energy yield was estimated to increase by 11.3%, or 1.19 Wh/Wp.

Under the assumption of replacing the asphalt on the ground by highly reflective concrete with an albedo of 0.5, it was estimated that the PV yield would increase by 20% on a wall point 3.5 m above ground. At a point 12 m above ground, which is a usual position for PV installations inside such a canyon, the PV yield was estimated to still increase by 7.3% compared to asphalt. The total yield produced for a selected period and with asphalt on the ground was 32.8 Wh/Wp. For the same time the incident irradiation was estimated to increase from a total of 37.5 kWh m^{-2} by 7.4%.

This study clearly shows that the amount of radiation reflected from the ground cannot be neglected for PV yield estimations of facade installations inside an urban canyon. Further, increasing the ground's albedo can have a significant impact on the yield of PV facades in an urban environment. However, for the assessment of economic aspects of PV installations inside an urban environment and PV potential analysis better simulation tools are required. Those are required to calculate the ground-reflected irradiance on facades inside an urban canyon more accurately. Besides accuracy, algorithms should require only short computational time such that larger urban areas can be simulated within a reasonable amount of time.

For an extensive study of the potential PV yield inside an urban canyon it will be required to assess various scenarios. Those scenarios should account for different urban geometries (e.g. canyon orientation and building height to street width ratio) and different ground-surface materials. The PV yield should also be calculated over the period of a full year to account for the varying sun altitude with its implications. In conjunction with studies of on cool pavements, the assessment of synergy effects between PV yield and compensation of energy consumption in buildings is a relevant topic.

6. Declaration of interest

None.

Acknowledgement

The research leading to these results has received funding from the Austrian Research Programme (Stadt der Zukunft, 3. Ausschreibung 2015) under grant agreement number 854691. The authors thank Eamon McDermott and Sean Philipp for their input during revision.

Appendix

List of symbols	
α_{Imp}	temperature coefficient of PV current
α_{Isc}	temperature coefficient of the short circuit current
β	tilt of the receiving plane
β_{Vmp}	temperature coefficient of PV voltage
$\delta(T_{\mathrm{m}})$	thermal voltage at temperature T_{m}
θ	solar angle of incidence on the wall point
θ_{b2}	solar angle of incidence onto facade of building b2 (facade at wall point)
θ_{gnd}	solar angle of incidence onto the ground
ρ	ground albedo
ρ_{b1}	albedo of the facade on building b1 (opposing the wall point)
ρ_{b2}	specular reflectance of building b2 (glass, facade at wall point)
$\rho_{\mathrm{b2,dif}}$	specular reflectance for diffuse irradiance of building b2
$\rho_{\mathrm{b2,dir}}$	specular reflectance for direct irradiance of building b2
$\rho_{\mathrm{gnd,i}}$	albedo of the *i*th subpart of the ground surface
ρ_{high}	albedo for condition with the higher ground-albedo
ρ_{low}	albedo for condition with the lower ground-albedo
C_0, C_1	empirical coefficients for PV module
C_2, C_3	empirical coefficients for PV module
DHI	diffuse horizontal irradiance
DNI	direct normal irradiance
f_{b1}	view factor from the wall point to the building b1 (opposing the wall point)
$f_{\mathrm{b1,b2}}$	view factor from building b1 to building b2 (facade at wall point)
$f_{\mathrm{b1,gnd,i}}$	view factor from building b1 to the *i*th subpart of the ground surface
$f_{\mathrm{b1,sky}}$	sky view factor for facade of building b1 (opposing the wall point)
$f_{\mathrm{b2,sky}}$	sky view factor for facade of building b2 (facade at wall point)
$f_{\mathrm{gnd,b1}}$	view factor from the ground to building b1
$f_{\mathrm{gnd,b2}}$	view factor from the ground to building b2
$f_{\mathrm{gnd,i}}$	view factor from the wall point to the *i*th subpart of the ground surface
$f_{\mathrm{gnd,sky}}$	sky view factor for the ground
f_{sky}	sky view factor for the wall point
G	global horizontal irradiation

G_{b1}	total irradiance onto the facade of building b1 (opposing the wall point)
$G_{b1,sky}$	total irradiance from the sky onto building b1 (opposing the wall point)
$G_{b2,sky}$	total irradiance from the sky onto building b2 (facade at wall point)
G_e	effective irradiance
g_G	gain of the irradiance at the wall point
G_{gnd}	total irradiance onto the ground surface
$G_{gnd,sky}$	total irradiance from the sky onto the ground surface
G_h	irradiance at a wall point in horizontal plane
g_{PV}	gain of PV power at the wall point
G_{sky}	total irradiance from the sky onto a wall point
G_v	irradiance at a wall point in vertical plane (herein facing south)
$G_{v,sim}$	simulated vertical irradiance onto the wall point
I_{mp}	current at maximum power point
$I_{mp,0}$	current at maximum power point at standard condition
I_{sc}	short circuit current of PV module
$I_{sc,0}$	short circuit current at reference condition of 1000 W/m^2 and 25 °C
N_s	number of PV cell connected in series
P_{mp}	PV power at maximum power point
sh	fraction of shadow on the ground surface
T_0	reference temperature of 25 °C
T_a	ambient air temperature
T_m	PV module backside temperature
V_{mp}	voltage at maximum power point
$V_{mp,0}$	voltage at maximum power point at standard condition

References

Andrews, R.W., Pearce, J.M., 2013. The effect of spectral albedo on amorphous silicon and crystalline silicon solar photovoltaic device performance. Sol. Energy 91, 233–241. https://doi.org/10.1016/j.solener.2013.01.030.

Andrews, R.W., Pearce, J.M., 2012. Prediction of energy effects on photovoltaic systems due to snowfall events. In: 2012 38th IEEE Photovoltaic Specialists Conference (PVSC). Presented at the 2012 38th IEEE Photovoltaic Specialists Conference (PVSC), pp. 003386–003391. https://doi.org/10.1109/PVSC.2012.6318297.

Brennan, M.P., Abramase, A.L., Andrews, R.W., Pearce, J.M., 2014. Effects of spectral albedo on solar photovoltaic devices. Sol. Energy Mater. Sol. Cells 124, 111–116. https://doi.org/10.1016/j.solmat.2014.01.046.

Dvorak, E., 2016. PV im dicht verbauten Gebiet - Treiber und Hemmnisse aus Sicht der Stadt Wien.

EMS Brno, 2016. Global radiation sensor EMS 11 [WWW Document]. URL http://emsbrno.cz/r.axd/pdf_v_EMS11_u_pdf.jpg?ver= (Accessed 8.16.16).

Fechner, H., Mayr, C., Schneider, A., Rennhofer, M., Peharz, G., 2016. Technologie-Roadmap für Photovoltaik in Österreich (Report for energy and environmental research No. 15/2016), Berichte aus Energie- und Umweltforschung. Bundesministerium für Verkehr, Innovation und Technologie, Austria, Vienna, Austria.

Freitas, S., Catita, C., Redweik, P., Brito, M.C., 2015. Modelling solar potential in the urban environment: State-of-the-art review. Renew. Sustain. Energy Rev. 41, 915–931. https://doi.org/10.1016/j.rser.2014.08.060.

Gilman, P., n.d. Sandia National Laboratories Modules Database [WWW Document]. Syst. Advis. Model SAM - Libr. Databases. URL https://sam.nrel.gov/sites/default/files/sam-library-sandia-modules-2015-6-30.csv (Accessed 2.4.16).

IEA, 2014. Technology Roadmap: Solar Photovoltaic Energy, 2014 edition. OECD/IEA, Paris.

Ineichen, P., Guisan, O., Perez, R., 1990. Ground-reflected radiation and albedo. Sol. Energy 44, 207–214. https://doi.org/10.1016/0038-092X(90)90149-7.

Ineichen, P., Perez, R., 2002. A new airmass independent formulation for the Linke turbidity coefficient. Sol. Energy 73, 151–157. https://doi.org/10.1016/S0038-092X(02)00045-2.

King, D.L., Boyson, W.E., Kratochvil, J.A., 2004. Photovoltaic Array Performance Model (No. SAND2004-3535). Sandia National Laboratories.

Krawietz, S., Poortmans, J., Masson, G., Pause, F., Palm, J., Schlatmann, R., 2016. BIPV Position Paper - Building Integrated Photovoltaics (BIPV) as a core Element for Smart Cities.

Krispel, S., Peyerl, M., Maier, G., Weihs, P., 2017. Urban Heat Islands – Reduktion von innerstädtischen Wärmeinseln durch Whitetopping. Bauphysik 39, 33–40. https://doi.org/10.1002/bapi.201710002.

Lindberg, F., Jonsson, P., Honjo, T., Wästberg, D., 2015. Solar energy on building envelopes – 3D modelling in a 2D environment. Sol. Energy 115, 369–378. https://doi.org/10.1016/j.solener.2015.03.001.

Mohajerani, A., Bakaric, J., Jeffrey-Bailey, T., 2017. The urban heat island effect, its causes, and mitigation, with reference to the thermal properties of asphalt concrete. J. Environ. Manage. 197, 522–538. https://doi.org/10.1016/j.jenvman.2017.03.095.

Olefs, M., Baumgartner, D.J., Obleitner, F., Bichler, C., Foelsche, U., Pietsch, H., Rieder, H.E., Weihs, P., Geyer, F., Haiden, T., Sch, W., ner, 2016. The Austrian radiation monitoring network ARAD – best practice and added value. Atmos Meas Tech 9, 1513–1531. https://doi.org/10.5194/amt-9-1513-2016.

Qin, Y., 2015a. A review on the development of cool pavements to mitigate urban heat island effect. Renew. Sustain. Energy Rev. 52, 445–459. https://doi.org/10.1016/j.rser.2015.07.177.

Qin, Y., 2015b. Urban canyon albedo and its implication on the use of reflective cool pavements. Energy Build. 96, 86–94. https://doi.org/10.1016/j.enbuild.2015.03.005.

Redweik, P., Catita, C., Brito, M., 2013. Solar energy potential on roofs and facades in an urban landscape. Sol. Energy 97, 332–341. https://doi.org/10.1016/j.solener.2013.08.036.

Remund, J., Wald, L., Lefèvre, M., Ranchin, T., Page, J.H., 2003. Worldwide Linke turbidity information. In: ISES Solar World Congress 2003. International Solar Energy Society (ISES), Göteborg, Sweden, pp. 13.

Revesz, M., Oswald, S., Trimmel, H., Schneider, A., Weihs, P., Zamini, S., Peyerl, M., Krispel, S., 2017. PVOPTI-Ray: Optimisation of reflecting materials and photovoltaic yield in an urban context. In: Proceedings of 33rd European Photovoltaic Solar Energy Conference and Exhibition. Presented at the 33rd European Photovoltaic Solar Energy Conference and Exhibition, Amsterdam, pp. 2130–2134. https://doi.org/10.4229/EUPVSEC20172017-6DO.11.4.

Rosso, F., Pisello, A.L., Cotana, F., Ferrero, M., 2016. On the thermal and visual pedestrians' perception about cool natural stones for urban paving: A field survey in summer conditions. Build. Environ. 107, 198–214. https://doi.org/10.1016/j.buildenv.2016.07.028.

Santamouris, M., 2014. Cooling the cities – A review of reflective and green roof mitigation technologies to fight heat island and improve comfort in urban environments. Sol. Energy 103, 682–703. https://doi.org/10.1016/j.solener.2012.07.003.

Santamouris, M., 2013. Using cool pavements as a mitigation strategy to fight urban heat island—A review of the actual developments. Renew. Sustain. Energy Rev. 26, 224–240. https://doi.org/10.1016/j.rser.2013.05.047.

Taha, H., 1997. Urban climates and heat islands: albedo, evapotranspiration, and anthropogenic heat. Energy Build. 25, 99–103. https://doi.org/10.1016/S0378-7788(96)00999-1.

Yaghoobian, N., Kleissl, J., 2012. Effect of reflective pavements on building energy use. Urban Clim. 2, 25–42. https://doi.org/10.1016/j.uclim.2012.09.002.

4.2 Publication II

SEBEpv – New digital surface model based method for estimating the ground reflected irradiance in an urban environment

https://doi.org/10.1016/j.solener.2020.01.075

Solar Energy 199 (2020) 400–410

Contents lists available at ScienceDirect

Solar Energy

journal homepage: www.elsevier.com/locate/solener

SEBEpv – New digital surface model based method for estimating the ground reflected irradiance in an urban environment

Michael Revesz[a,*], Shokufeh Zamini[a], Sandro M. Oswald[b,1], Heidelinde Trimmel[b], Philipp Weihs[b]

[a] AIT Austrian Institute of Technology GmbH, Vienna, Austria
[b] Institute of Meteorology and Climatology, University of Natural Resources and Life Sciences, Vienna, Austria

ARTICLE INFO

Keywords:
Reflected radiation
Solar radiation
Urban environment
Modelling
Digital surface model
Photovoltaic

ABSTRACT

Knowing the solar radiation fluxes inside an urban canyon is of interest for different purposes: e.g. urban climatology and studies of human thermal comfort and gaining relevance for future renewable energy generation in an urban environment using photovoltaic systems. For the latter, mainly rooftops are of interest, but studies started to extend towards the solar resources on building facades. However, the reflected solar radiation from the ground is either neglected or estimated using simplifications that lead to overestimation.

SEBEpv (Solar Energy on Building Envelope – photovoltaic) is a new tool attempting to provide better estimates for the radiation reflected from the ground onto facades. It is primarily intended for the urban environment where the ground-view is very limited. SEBEpv delivers 3D results based on digital surface models of the environment. Furthermore, an optional PV model was added in order to address the simplified of estimation of reflected radiation when modelling photovoltaic (PV) yields.

SEBEpv delivers quite good estimates for the solar radiation compared to the measurements. The simulated irradiance shows an RMSE of 28.7 W/m^2 compared to the measured irradiance and has a bias close to zero. This is about half the RMSE shown by the predecessor tool SEBE. The measured total irradiation over two years shows a bias of about 7%, which is likely to be a result of the limited angular resolution of the shading algorithm. Overall, SEBEpv seems to be a promising tool, accounting for reflected radiation in urban environments.

1. Introduction

In an urban environment, the available solar resource is of special interest for different applications and fields of research. This applies to research in urban climate, e.g. estimating the urban energy balance. It is also important for evaluating the thermal comfort of humans, especially in the context of global warming. Estimating the available solar radiation is also required in the field of renewable energy generation, e.g. making economic decisions or analysing the energy potential of photovoltaic (PV) or solar thermal systems. Already proposed for several years, renewable energy generation may become relevant inside the urban environment (IEA, 2014; Krawietz et al., 2016).

Inside the complex urban structure not only shadowing, but also the reflected solar radiation from the ground or other buildings and obstacles, has an impact on the total irradiation on surfaces. A facade oriented towards an open square receives higher amounts of reflected radiation than in a narrow street. Increasing the surface albedo of the surroundings in an urban environment also increases the amount of reflections. The latter case can be desired for the purpose of heat island mitigation (Mohajerani et al., 2017; Santamouris, 2014; Taha, 1997), or to increase the yields of PV systems. The contribution to the total irradiation of a surface is largest when those are vertical, e.g. the building facades. Recent studies as Revesz et al. (2018) showed that if the ground's albedo inside an urban canyon is quadrupled, the PV yields can be increased by about 7% on the top level of south-facing facades. Therefore, urban solar resource assessment in general has been of increased interest for research. The importance of estimating irradiation and reflected radiation on building facades was also confirmed by e.g. Brito et al. (Oct. 2017), Catita et al. (2014), or Rodríguez et al. (2017).

A common approach for estimating the radiation reflected from the ground uses the simple geometric relationship $1/2(1 - \cos\theta)\rho G$, depending on the tilt angle θ of the analysed plane, the surface albedo ρ of the surroundings and the global horizontal irradiance G (Ineichen et al., 1990). This approach is usually used, because the contribution to the

* Corresponding author at: Institute of Meteorology and Climatology, University of Natural Resources and Life Sciences, Vienna, Austria.
E-mail addresses: michael.revesz@boku.ac.at (M. Revesz), shokufeh.zamini@ait.ac.at (S. Zamini), sandro.oswald@zamg.ac.at (S.M. Oswald), heidelinde.trimmel@boku.ac.at (H. Trimmel), philipp.weihs@boku.ac.at (P. Weihs).
[1] Present address: Urban Climate Modelling, Central Institution of Meteorology and Geodynamics (ZAMG), Vienna, Austria

https://doi.org/10.1016/j.solener.2020.01.075
Received 20 September 2019; Received in revised form 15 December 2019; Accepted 27 January 2020

total radiation is argued to be rather small due to relatively small albedo values, which is especially valid for non-vertical surfaces. Multiple reflections may even be neglected (Lorenzo, 2011). The limits of this approach were briefly discussed in (Revesz et al., 2018) for the case of urban canyons. Furthermore, using G does not account for differences in the amount of radiation that is reflected by surrounding surfaces due to the shading of those reflecting surfaces or their orientation and tilt. In most cases, the reflected irradiance component is overestimated.

However, there are many different tools and models for assessing the solar resource. An overview on applications and tools is given, starting with the first group of tools as used for architectural design and daylighting analysis. Another group is used for energy system design and analysis, e.g. of solar thermal and PV systems. As third, there are tools for solar resource assessment and are partially related to urban climate topics. Reviews on tools for assessing the urban solar potential, daylighting or for solar design were presented in Freitas et al. (2015) and Jakica (2018). However, information on the estimation of reflected irradiation is not published for all tools or models.

In architectural design and daylight assessment the tools are often based on ray-tracing methods, e.g. Daysim or ECOTECT that are both based on RADIANCE. Therefore, they account for surface reflections, but are computationally intensive (Freitas et al., 2015; Machete et al., Oct. 2018). Due to the higher computation time those tools are not used for the analysis of solar potential, especially for areas of district scale or much larger.

The tools used for designing solar-based energy generation systems are mainly based on estimating the solar resource by geometric considerations. In general, those tools were developed for designing field power plants or rooftop systems. For that application an average albedo of the surrounding is assumed (Dr. Valentin EnergieSoftware GmbH, 2013; PVsyst, 2012) and the method for estimating the reflected irradiance as mentioned before is sufficient. However, this method has increased uncertainty in case of systems mounted on facades and with vertical tilt, especially in an urban environment. There is one tool based on Daysim and ray-tracing that was specifically developed to simulate rooftop PV systems in cities. It uses LiDAR (Light Detection And Ranging) data for its 3D model, but doesn't consider building facades (Jakubiec and Reinhart, 2013). Also, in the tool SimStadt walls are currently neglected, as presented by Rodríguez et al. (2017).

Many different approaches are used for modelling the solar irradiation in the third group of application: solar resource analysis. Except for the tools that were only developed for the assessment on rooftops (Li et al., 2016; Lukac et al., 2013), usually the geometric method as mentioned before is used for solar potential estimation (e.g. in PVGIS (Šúri et al., 2005)), especially when used in GIS applications (Hofierka and Zlocha, 2012; Šúri and Hofierka, 2004). In contrast, there are tools that specifically address the urban environment and estimate the solar irradiation on building facades. However, SOL, Surfsun3D (based on r.sun) and SORAM for example do not account for reflections onto facades (Erdélyi et al., 2014; Liang et al., 2015; Redweik et al., 2013). Amongst GIS tools, ArcGIS was reported not having a suitable model for the reflected irradiation inside a street canyon due to its 2.5D urban representation (Machete et al., Oct. 2018). The term "2.5D" refers to the representation of objects as spatial distribution of their height, in contrast to the objects' definition in 3D space. A more detailed GIS based tool is "Solar energy on building envelope" (SEBE) that is part of the "Urban Multi-scale Environmental Predictor" (UMEP) toolbox (Lindberg et al., 2015, 2018). SEBE sums over sky-patches to approximate the view-factor into ground and building surfaces, assuming one average albedo and using the global horizontal irradiation (Lindberg et al., 2015). Methods for a more accurate estimation of reflections inside an urban canyon and even accounting for multiple reflections appear in applications of urban climate modelling. Though, those were only applied to simplified parametric street canyons (Qin, 2015).

Recent developments on tools that estimate the urban solar potential and include improved algorithms for the reflected irradiation were published during the last 2 years. Those methods are based on estimating view-factors (Calcabrini et al., 2019; Chatzipoulka et al., 2016, 2018) or simplified ray-tracing algorithms to overcome the issue of computation time (Liao and Heo, 2017; Waibel et al., 2017) and were only validated against other tools. Another method published in (Calcabrini et al., 2019) is based on fitting a parameter to measurement data and is only valid for that particular location and typical climatic condition. This confirmed that accounting for ground- and building-reflections inside an urban canyon is an open research topic and improved tools are needed. In an attempt to improve the estimation of the solar resource on building surfaces, SEBEpv (Solar Energy on Building Envelope – photovoltaic) was developed based on SEBE (Solar energy on building envelopes) (Lindberg et al., 2015).

2. New tool proposal: SEBEpv

2.1. Introduction to the tool

In SEBEpv the estimation of reflected irradiation inside the urban environment was improved, with a focus on facades. In addition, SEBEpv was extended with a model to estimate the PV yield, hence the suffix "pv". The PV yield is determined by using a model published in Huld et al. (2010, 2011) which is not subject of the validation. However, this feature came on the cost of computational time. SEBE itself is a very fast and effective algorithm to estimate the solar potential on roofs and building facades. SEBEpv is a GIS application and was developed as a plug-in for QGIS 2 (QGIS Development Team, 2019). It uses a digital surface model (DSM) as raster input, which is often available for urban areas. The DSM data for this study origins from https://www.wien.gv.at/ma41datenviewer/public/. European wide one can search at https://www.europeandataportal.eu/ for publicly accessible, national databases. The source code is found at https://bitbucket.org/pvoptiray/umep-3d/.

Fig. 1 shows the flow diagram of SEBEpv, including input, output and important intermediate results that are used for further steps are highlighted. Similar to SEBE, SEBEpv uses the concept of a hemisphere divided in 145 sky-patches, being approximately of equal solid angles (Robinson and Stone, 2004; Lindberg et al., 2015). This hemisphere of sky-patches is used to pre-process the distribution of the direct and diffuse irradiance components on the sky-vault and also sets the viewing directions used for shadow casting. In contrast to other tools, the algorithm of SEBEpv first determines the shading on all surfaces (facades, ground, roofs) including the shadow of the ground surfaces onto the walls which is used for estimating the ground-reflections (see Section 2.3), then calculates the direct and diffuse sky irradiance onto those and only afterwards the radiation reflected from those surfaces.

2.2. Irradiance components onto urban surfaces

SEBEpv makes use of the direct input of all three irradiance components: global horizontal (GHI), direct normal (DNI) and diffuse horizontal (DHI) irradiance. Nevertheless, if only GHI is provided then DNI and DHI are estimated after Reindl et al. (1990) as done by SEBE. The diffuse radiation from the sky is distributed anisotropically onto all sky-patches according to Perez et al. (1993). In SEBE the direct irradiance component onto a tilted surface is calculated by using the azimuth and elevation angles of the sky-patch associated with the respective sun position to determine the angle of incidence. This is handled different in SEBEpv, where the actual sun position angle is used to determine the angle of incidence of DNI onto the tilted surface (Lindberg et al., 2015).

The total irradiance onto roof and ground surfaces ($G_{r,g}$) on the DSM is calculated by adding up the direct, diffuse and reflected radiation from the directions of all patches on the hemisphere:

$$G_{r,g} = \sum_{i=1}^{p} [I\theta S + DS + G(1 - S)\alpha]_i \tag{1}$$

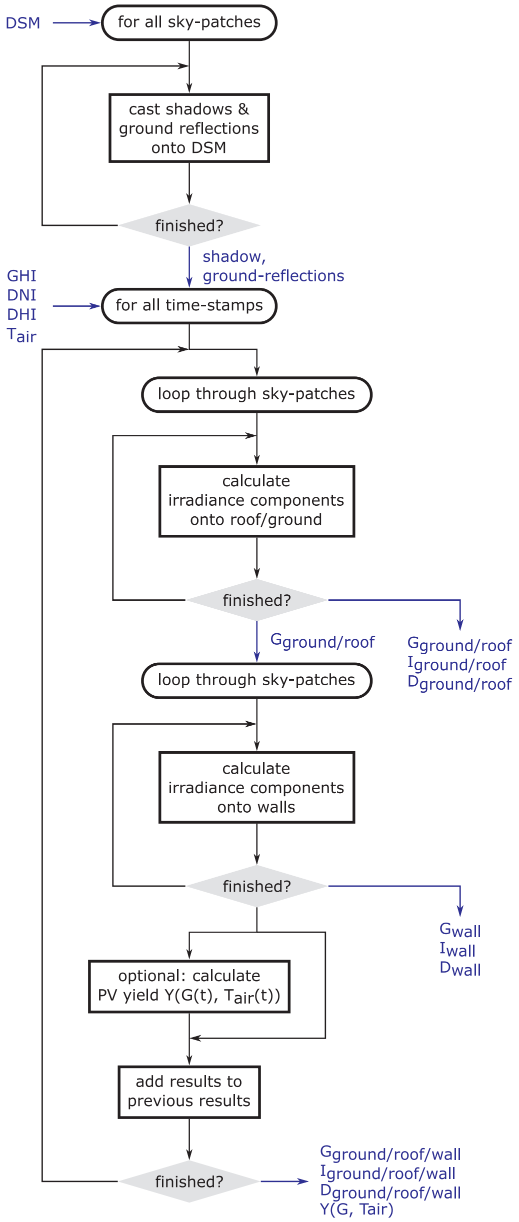

Fig. 1. Flow diagram for SEBEpv. Inputs: DSM is the digital surface model of the scenery; GHI is the global horizontal, DNI the direct normal and DHI the diffuse horizontal irradiance. Outputs: G, I and D are the total, direct and diffuse components for the irradiation received by the surfaces noted as subscript, respectively; optional output is the PV yield Y at each data point, requiring the pair of irradiation and air temperature T_{air}.

where p is the number of sky-patches on the hemisphere, I is the direct radiation, D is the diffuse radiation and G is the global radiation from the i-th patch. It should be noted that G is determined by distributing GHI isotropically onto all hemisphere patches. θ is the angle of incidence of the sun onto the surface and α is the global surface albedo set for all surfaces. S is the shadow determined for each surface pixel in the direction of the i-th patch.

The direct and diffuse radiation onto the wall pixel are calculated in the same manner as for the roof and ground surfaces. However, the reflected irradiance component is calculated different than in SEBE and the newly developed method is described in Section 2.3. Multiple reflections, especially wall-to-wall are not considered. Implications of the latter are discussed later. As a result, the final estimated irradiation onto the building facades constitutes a lower boundary for the solar potential. Thus, the estimate is more useful to economic analysis than if it was overestimated.

In addition to the mentioned changes in the algorithm, SEBEpv has the possibility to distinguish between the albedo of building walls and the roof or ground surfaces. It is also possible to load raster data specifying the spatial distribution of the surface reflectivity. This is rather unique as usually a constant ground-albedo is assumed for the whole ground surface (Demain et al., 2013). However, only one value of albedo can be set for all walls in the DSM.

2.3. Estimation of the ground reflected component

The main idea for determining which facade pixel receive radiation reflected from the ground is taken from the shadow casting algorithm that is used in SEBE. The viewing directions are set to the 145 hemisphere-patches. Shadows are cast by shifting the DSM raster by one pixel in x direction (the larger dimension) and by a value corresponding to the respective orientation and elevation angle in y and z direction (Lindberg et al., 2015, 2018; Ratti and Richens, 2004). This approach limits the required number of calculations, on the one hand by the number of view-angles and on the other hand by the largest dimension of the DSM-array.

The new idea for treating ground-reflections is to determine those using a method equivalent to shadow-casting. It must be noted that all surfaces are assumed to reflect radiation isotropically. Specular reflectance, as it would be the case e.g. for glazing, or anisotropic reflectance require a more detailed algorithm and knowledge about the present surface materials. Ground-reflections from one direction are treated as the respective shadow of the ground onto walls using a z-inverted DSM raster. In Fig. 2 the method is shown for one orientation. The highest level at a wall that still receives radiation reflected onto it from a specific orientation, corresponds to the projection of the last ground-pixel lying ahead of an opposite wall.

The reflected radiation is weighted with the view-factor between a wall-pixel (with assumed unit area of 1 m^2 to keep the units of irradiance as W/m^2) and the reflecting ground using

$$GVF_i = \frac{-1}{\pi}\frac{(\vec{r_i}\,\vec{n}_{\mathrm{w}})\cdot(\vec{r_i}\,\vec{n}_{\mathrm{g},i})}{(\vec{r_i}\,\vec{r_i}\,)^2}\cdot \mathrm{d}A_i, \tag{2}$$

where GVF_i is the view-factor of the ith reflecting ground-patch, $\vec{r_i}$ is the spatial vector from the wall point to the ith patch of ground, $\vec{n}_{\mathrm{w}}$ is the normal vector onto the wall surface, $\vec{n}_{\mathrm{g},i}$ the normal vector onto the ith patch of ground and $\mathrm{d}A_i$ is the surface area of the ith patch of ground (Walton, 2002). Finally, reflections from each of the visible ground-patches are summed to the total ground-reflected irradiance G_{r} onto a wall pixel by

$$G_{\mathrm{r}} = \sum_{i}^{N} GVF_i\cdot\overline{G}_{\mathrm{g},i}, \tag{3}$$

where N is the total number of visible ground-patches and $\overline{G}_{\mathrm{g},i}$ is the average radiation reflected from the ith patch of ground.

$\overline{G}_{\mathrm{g},i}$ is estimated as the mean irradiation on the ground within the ground area $\mathrm{d}A_i$, which is a projection of the corresponding hemisphere-patch. To determine the mean irradiation, that area is divided in four equal areas. Afterwards, the irradiation at the respective centre points is multiplied with the corresponding reflectivity followed by calculating their average value. This also allows to distinguish between different ground surfaces with varying values for the albedo. However, with greater distance smaller areas with a different ground-albedo

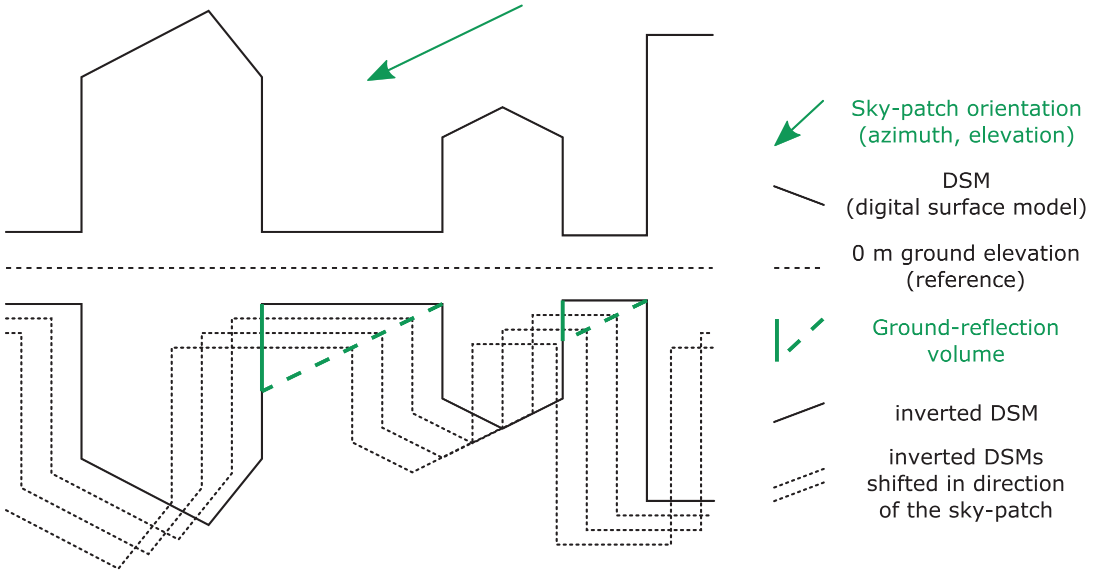

Fig. 2. Ground-reflection algorithm: "shadow"-casting on an inverted digital surface model (DSM). The DSM and inverted DSM are shown as solid lines above and below the dashed line marking the zero-elevation. The direction of shadow-casting is marked with the green arrow. The incrementally shifted inverted DSMs are shown as black dotted lines and the resulting projection of the ground surface onto the walls of the inverted DSM is marked in green. (For interpretation of the references to colour in this figure legend, the reader is referred to the web version of this article.)

cannot be resolved well. Currently no distance-limits are applied.

3. Evaluation of the model

3.1. Measurements inside a street canyon

For the validation of SEBEpv, measurements of the solar irradiance were performed inside an urban canyon at the University of Natural Resources and Life Sciences in Vienna, Austria. A map of the location is shown in Fig. 3. The measurements were taken for a period of about 2 years, from August 2016 until September 2018. All measured values are 1-min means, aggregated from samples at a 5-s interval. Non-shaded DNI and GHI were measured on the rooftop. The diffuse irradiance component was deducted from those measurements via $DHI = GHI - sin(\theta)DNI$ with θ being the sun elevation angle. The circumsolar part was considered in the diffuse component, except what lies within the pyrheliometer's field of view of 5° (Kipp and Zonen, 2008). Further, inside the canyon at 3.5 m above ground the vertical irradiance at a facade facing south was measured. The street canyon and the position of the vertical irradiance sensor (marked with a white X) are shown in Fig. 4.

As for the instrumentation, an EKO MS-802 pyranometer and Kipp & Zonen CHP-1 pyrheliometer were used to measure GHI and DNI, respectively. Quality of the measurements was ensured by comparison with measurements of the ARAD site Wien Hohe Warte (Olefs et al., 2016). The uncertainty of the pyranometer is lower than 1 W/m^2. For the measurement at the facade, the silicon diode irradiance sensor EMS 11 was used with a reported calibration error of max. 7% (EMS Brno, 2016). To ensure the quality of the measurements, these sensors were previously compared to measurements with the pyranometer. This sensor was initially chosen for its similarity in spectral response compared to photovoltaic modules. Further details on the measurements can be found in Revesz et al. (2018).

Since in the past EMS Brno sensors showed larger drift with time, the used sensor was checked for drift as well. The irradiation measured at the roof (GHI and DHI) was converted to vertical irradiance at the facade using view-factors, as described in (Revesz et al., 2018) followed by a comparison between the measured irradiation at the facade and the estimated value. It was concluded that the used sensor did not exhibit any significant drift per year and the drift was below 1 $W/(m^2a)$. The estimated drift is relative to the drift of the more stable pyranometer and pyrheliometer.

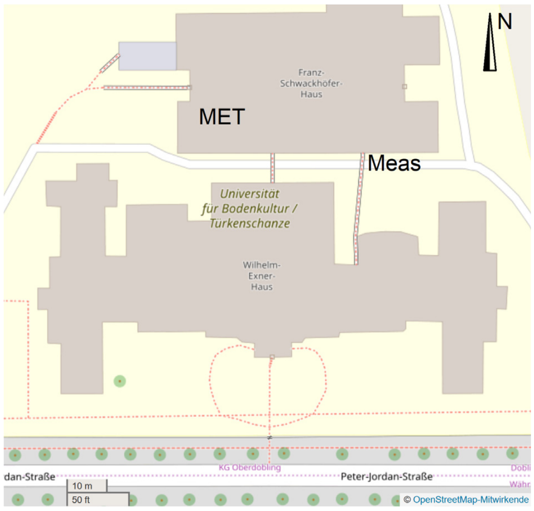

Fig. 3. Map of the measurement site at the University of Natural Resources and Life Sciences in Vienna, Austria. Undisturbed irradiance components were measured at the roof of Schwackhoefer Haus (marked "MET") and the vertical irradiance was measured at the southern facade of this building (marked "Meas"). ©OpenStreetMap contributors, http://www.openstreetmap.org/copyright.

3.2. Model input

The input for modelling the solar resource using SEBEpv and also

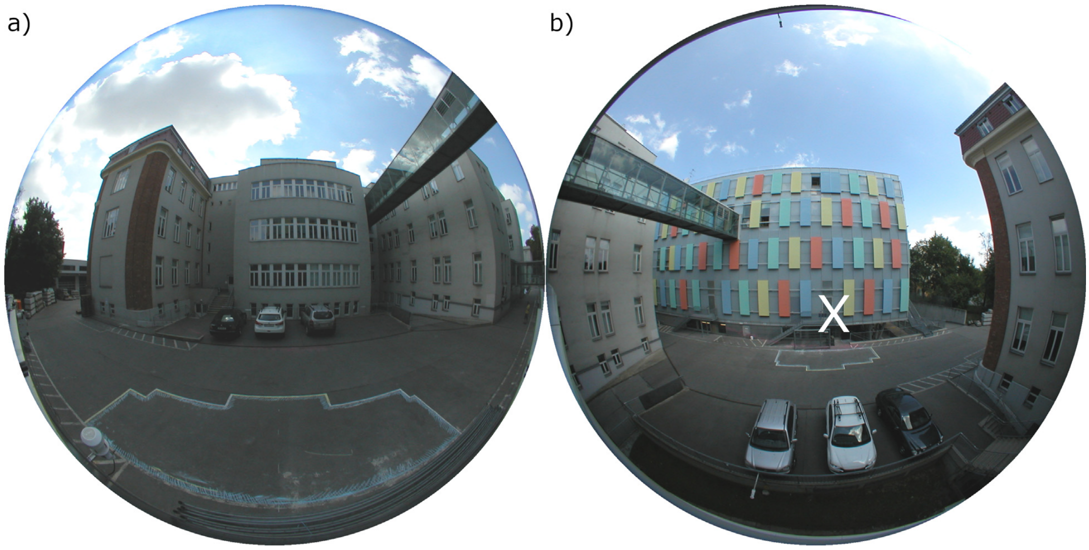

Fig. 4. Fisheye images of the street canyon used for measurements. (a) Field of view of the south facing irradiance sensor, (b) view from the north facing facade towards the measurement site (position of the irradiance sensor marked with a white X).

SEBE were the measured solar irradiance (GHI, DNI, DHI), the DSM for the site and the surface albedo. The DSM has a resolution of 0.5 m (https://www.wien.gv.at/ma41datenviewer/public/). The albedo of the ground was set to 0.13 and was only used to determine the ground-reflected component onto the facades. For the building facades the albedo was set to 0.27, as determined by measurements at the site, which was used to determine the reflected component onto the ground and the roof surfaces. The value for the facades' albedo corresponds to the value for the south-facing wall, since the higher value measured at the north-facing one was expected to have less influence on the simulation results. However, the value of the facades' reflectivity has no effect on the results at the measurement-site, as only the ground-reflection is considered in this version of SEBEpv. Simulations with SEBE were done assuming one global albedo of 0.13. The latter is a significant source of error in the results for SEBE since in reality the albedo of buildings is around double that and thus, the reflected radiation may be underestimated.

3.3. Model output

To demonstrate the output of SEBEpv, a 3D visualisation of the total and the reflected irradiation on the building surfaces is shown in Fig. 5. The irradiation was simulated for one clear sky day close to the summer solstice (24 June 2017) and for the buildings Exner Haus (in the south at the site) and Schwackhoefer Haus (northern building at the site) at the University of Natural Resources and Life Sciences in Vienna, Austria. A summer day was chosen due to the sites latitude, and consequent predominant shading during the winter. Fig. 5(a) shows the total irradiation on all surfaces, including the ground and roofs and (b) shows only the total radiation reflected onto the building facades. DSMs have limitations, such as the inability to represent hanging structures. This poses a problem for simulating buildings with e.g. complex vertical profile, balconies or hanging roofs and scenarios with a bridge connecting two buildings (see Fig. 4 with the bridge between the two buildings in this study). Those limitations were also described in Redweik et al. (2013), where also the process of deriving the urban 3D-model from LiDAR data is briefly described. The white artefacts visible in Fig. 5 usually arise from the visualisation in 3D space where data points, represented as cubes, do not overlap. However, the reason for the white patches of facade in Fig. 5(b) (bottom, right) is unknown, but may be due to data point values being set zero for an unknown reason.

3.4. Validation results

The quality of the simulation compared to the measured data was assessed for two subsets of the "complete" data set. One subset contains 99% of all data, during the whole two years period, with the lowest residuals. The other subset is further reduced to 95% of all data with the lowest residuals. The complete dataset is shown in Fig. 6, comparing measured and simulated irradiance with one-hour intervals. The points surrounded by the yellow dotted line are the 95%-subset and those surrounded by the teal dotted line are the 99%-subset. Except for the complete data, the regression lines are shown as thicker, solid lines in the respective colours, as well as the ideal correlation (black dashed line). The reason for sub-setting was the presence of erroneous measurement readings that were not easily filtered out (see Section 4.1). Those data were kept in the data set, while data with known equipment failures or easily detectable non-physical values were dismissed. A detailed discussion is presented in the Sections 4.1 and 4.2. The 95%-subset with hourly data shows an R^2 of 0.962 with a standard deviation of $\pm$ 29 Wm^{-2}. The Pearson correlation coefficient between measured data and the simulation with SEBEpv is 0.981, with normally distributed residuals. The 99%-subset of hourly data has an R^2 of 0.889, a Pearson correlation coefficient of 0.943 and an almost double standard deviation of $\pm$ 50 Wm^{-2}. In both cases the mean bias error is $\ll$ 1 Wm^{-2}.

In addition to the presented hourly data, clear sky days were selected and simulated with 10-min intervals. Due to the low height of the instruments above ground, the irradiation sensor was shaded by the building Exner Haus in the south and no direct radiation was reaching the irradiation sensor during winter. The duration of shading was shortest during the summer but was still evident in the measurement data. Therefore, only those days were selected for simulation, for which the irradiance sensor inside the street canyon was not shaded for most of the day. The error of these simulations was lower because of the lower temporal resolution. In that case the standard deviation was as low as $\pm$ 12 Wm^{-2}.

The monthly total irradiation and the total of all plausible data during the two years of measurement were compared to simulations with SEBEpv and its predecessor SEBE. SEBEpv was found to

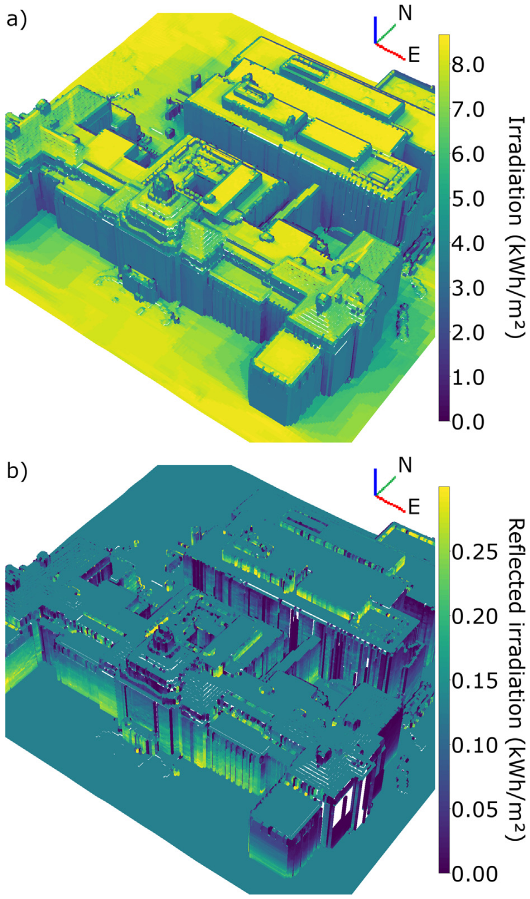

Fig. 5. Total irradiation (a) and radiation reflected onto building facades (b) during a clear sky day (24 June 2017) simulated with SEBEpv. The scenery is formed by the buildings Exner Haus and Schwackhoefer Haus at the University of Natural Resources and Life Sciences in Vienna, Austria. White surfaces, such as in (b) at the eastern facade, are artefacts in the visualisation only.

underestimate the total sum of irradiation at the wall point inside the street canyon by 7.0%. In contrast to SEBEpv, SEBE overestimates the total irradiation by 12.5%. This applies to the “complete” data set mentioned before. The monthly total irradiation resolved by the year of measurement is shown in Fig. 7. In Fig. 8 the relative differences in percent between the measurements and simulations are shown. The measured data is shown in dark purple and compared to results from SEBEpv (teal) and SEBE (yellow). The monthly irradiation must not be interpreted as solar potential, as the values for a few months are lower due to missing data.

In general, one can see that SEBE is overestimating the monthly sums, while SEBEpv is underestimating the irradiation except for four cases, January 2018, March 2018, June 2018 and November 2017. Reasons for these four cases of overestimation by SEBEpv were not found. As expected, the absolute difference between estimations with SEBEpv and measured data is rather small during winter month compared to summer months. However, the deviations increased in the course of spring and likewise decreased again in the course of autumn. Further, the deviations compared to the measurements for the months May, June and July where unexpected low. It is argued, that the variation of deviation during each year is significantly influenced by the shading algorithm, which is discussed in Section 4.2. The largest

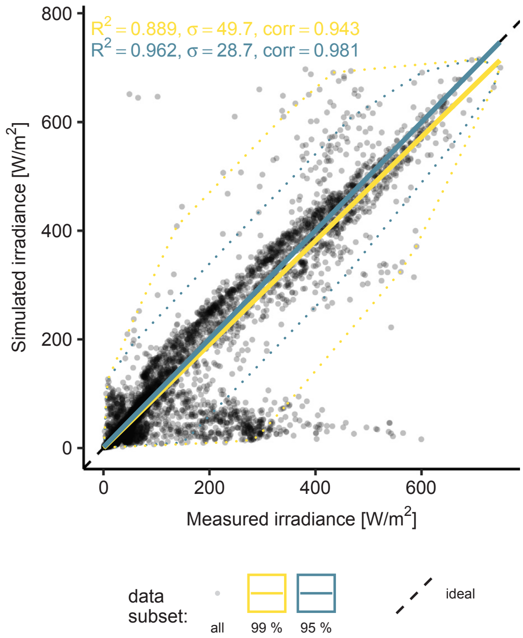

Fig. 6. Comparison of the measured and simulated hourly averaged data. Black dots show all data. Dotted lines surround: data within 99% quantile with lowest residuals (yellow) and within 95% quantile with lowest residuals (teal). The corresponding regression lines are shown as thick solid lines in respective colours; the black dashed line marks the ideal correlation. The values for adjusted R^2, standard deviation σ and Pearson correlation coefficient for the measured and simulated data are given in respective colours for the two subsets. (For interpretation of the references to colour in this figure legend, the reader is referred to the web version of this article.)

absolute deviations were consistently found in each year for April and August, and eventually was a result of the shading by Exner Haus in the south and its prediction by the shading algorithm. Monthly relative deviations for SEBEpv vary between − 21% and − 0.1% and the three cases of overestimation lie within the same bounds. The average relative deviation of monthly irradiation for SEBEpv is only about half of that for SEBE.

4. Discussion

4.1. Model-unrelated errors

The comparison of measured irradiance with the estimation by SEBEpv in Fig. 6 showed two types of major outliers. One of those is a group of uncorrelated scatters in the large irradiance range, being a significant overestimation by SEBEpv. It was found that those points are related to undetected outages of the pyrheliometer. However, it was not possible to reliably remove those outages from the data as the signal showed values around zero. As a result, the diffuse irradiation component was estimated to equal G and the irradiation on the facades was overestimated. Thus, these outliers are unrelated to the model of SEBEpv.

Another uncertainty is related to DSM. As previously stated, there is a bridge connecting the two buildings in the scenery. Bridges and other hanging structures cannot be represented in DSMs and appear as a solid building rising from the ground. To assess the uncertainty for the wall-point, that was used in the course of the validation, the scenery was modified, and the irradiation simulated during a clear sky day close to the summer solstice. It was found that adding the falsely blocked

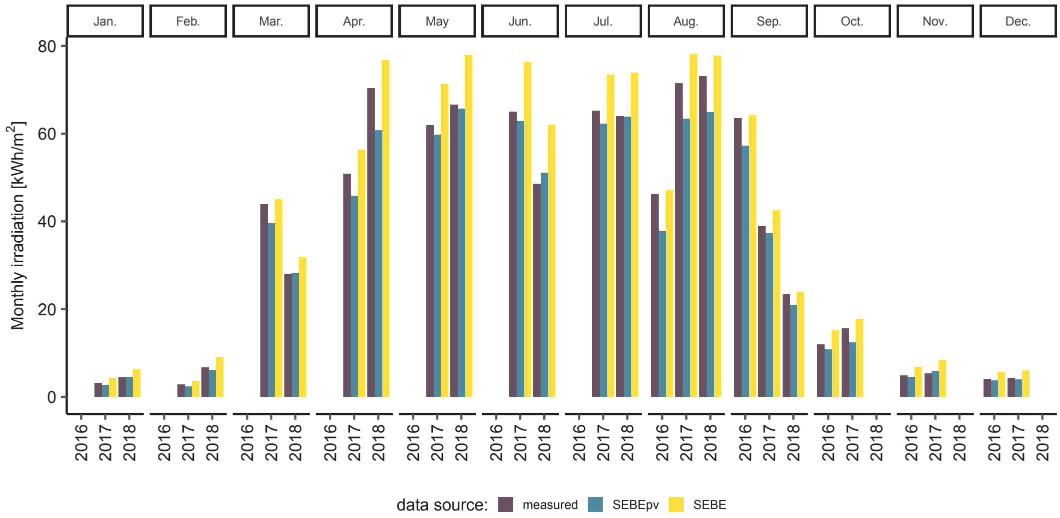

Fig. 7. Comparison of the monthly total irradiation for the measurements and the simulation tools SEBEpv and SEBE. Results are shown for each month of the year and the different years for which data is available.

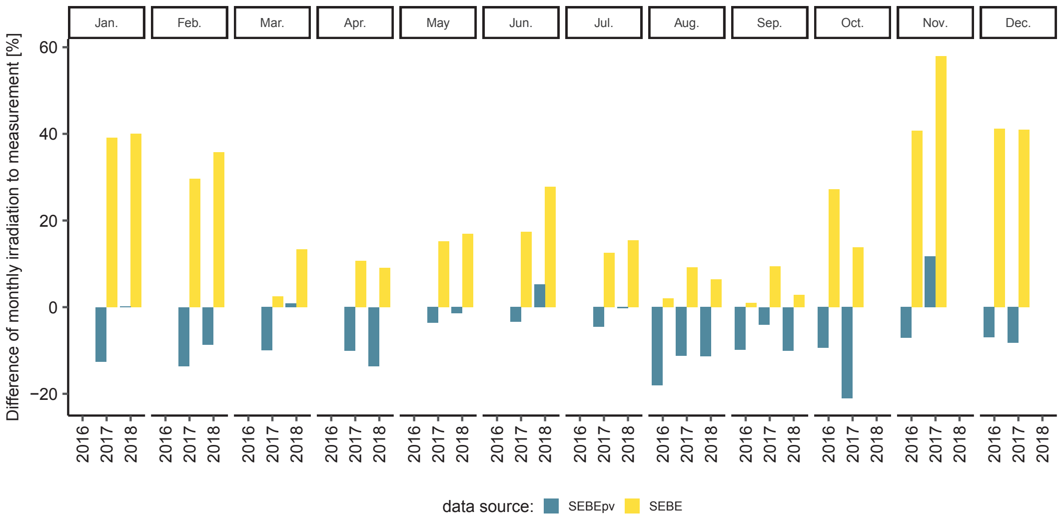

Fig. 8. Comparison of the relative difference of monthly total irradiation between the measurements and the simulation tools SEBEpv and SEBE, respectively. Results are shown for each month of the year and the different years for which data is available.

irradiation results in an increase of the total irradiation by 0.3%. Since this issue influences mostly diffuse irradiation from the western sky, it is assumed that the error may be slightly larger for a cloudy day in summer. The main contribution is expected to stem from reflections as in this situation the incidence angle for direct or diffuse irradiation from west is very shallow. Therefore, it is concluded that the uncertainty introduced due to wrong representation of the bridge is a bias error of less than 1%.

4.2. Uncertainties of SEBEpv

One group of outliers (see Fig. 6), as mentioned in Section 4.1, can be found as constant simulated values in the range of about zero to 100 W/m^2, independent of the measured irradiance. Those outliers were reliably attributed to the finite resolution of the sky-patches, also used for the shadow casting algorithm. However, the effect may be emphasised with low temporal resolution such as 1 h, which is the case here. Fig. 9 illustrates the problem by comparing the measured irradiance aggregated to a 10-min average and the average irradiance simulated by SEBEpv at the sensor location with a 10-min and 1-h temporal resolution, respectively. It shows the vertical irradiance at the described point on the facade for two clear sky days from 21 to 22 August 2018. On both days, the opposing building was casting shadows once in the morning and once in the afternoon. The differences can be seen best in the morning.

This case shows that the solid angle of one sky-patch with $1/145{\cdot}2\pi$ is already too large to resolve a shadow cast for the duration of only half an hour. For those two clear sky days, the impact on the estimated total irradiation is about 10%. Uncertainty of the radiation transposition, including reflected irradiance, was not deducted from that value. Furthermore, the impact depends on the season and has a much lower contribution during cloudy skies. Half the dimensions of a sky-patch

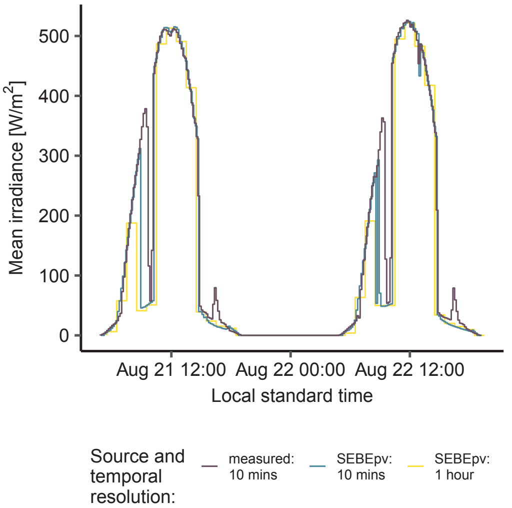

Fig. 9. Comparison between the measured vertical irradiance at the south-facing facade and the corresponding average value of the simulated irradiance to show the effect of temporal resolution in the shadow-casting algorithm. The measured irradiance (1-min temporal resolution) was aggregated to a 10-min average and the irradiance was simulated by SEBEpv with 10-min and 1-h temporal resolution, respectively. The data used is for the period between 21 and 22 August 2018.

may seem more appropriate but corresponds to approximately a quarter of its current solid angle. Then the impact on computation time must be considered.

An additional source of error can be attributed to the diffuse sky radiation model. As stated in Section 2.2, the anisotropic distribution of the sky diffuse irradiation onto the hemisphere is done using the model by Perez et al. (1993). The model's characteristics with positive deviation for high diffuse fraction and negative deviation for low diffuse fraction can be seen in Fig. 10. Therefore, it is concluded that the diffuse sky model does not introduce a large bias error. However, the

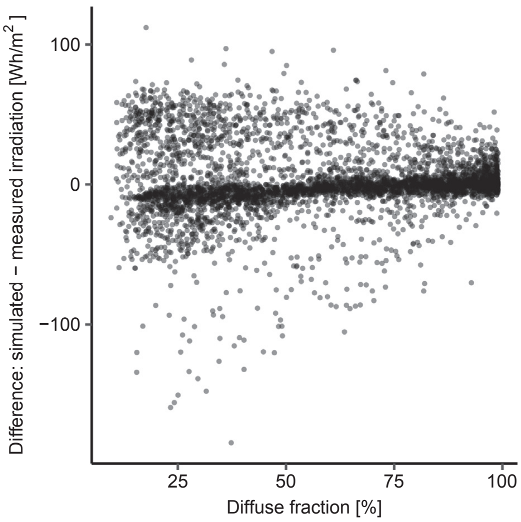

Fig. 10. Deviation between simulation results from SEBEpv and the measurements compared to the diffuse fraction. Except for data points where the state of shading differs for the measurements and the modelling results and caused a large deviation, all data was used.

frequency distribution of the diffuse fraction may allow explaining the differences of the deviation from the measurements for each month in different years. The occurrence of diffuse fraction, binned in the intervals [0%, 25%), [25%, 50%), [50%, 75%) and [75%, 100%), is shown for each month in Fig. 11. The three years of measurement are marked using different colour for easier comparison. For example, indeed the deviation in October 2017 is more negative than in 2016. Likewise, the deviation for June is more negative in 2017 than in 2018.

4.3. Various aspects of reflectivity

There are a few aspects regarding the choice of albedo-value as well as the complexity of models for the reflected radiation in a urban environment. Regarding the level of detail used for modelling the reflected component, there are two points to be aware of: In the case of SEBEpv reflectance is considered to be isotropic. However, in reality surfaces reflect radiation anisotropic and glazing or other glare causing materials may have a significant specular component (Demain et al., 2013). Especially inside an urban canyon the different materials on facades cause uncertainties to the estimated irradiance due to the spatial variability of the reflected component along facades. Related to specular reflectance, the effect of cars visible in Fig. 4 should be mentioned: For the south-facing facade, its view at a lower level is shown in subfigure (a), the influence is assumed to be negligible as the distant cars only cover a very small view-factor and are always parked in the shadow. However, the nearby north-facing facade may receive a more significant amount of radiation reflected from the cars due to the larger view-factor covered by those.

The other point concerns modelling only the ground-reflected component or increasing the level of detail by including wall-to-wall reflections (both considering only one reflection step) or even modelling multiple reflections. While the latter may be much less significant, wall-to-wall reflections can be considered relevant. This component was estimated for the south-facing wall point in this study and evaluating the implications for the modelling results of SEBEpv. The estimation is based on the known view-factors in this canyon and the measured albedo of 0.50 for the facade of Exner Haus, which is the building opposite to the measurement site and facing north. Further, the estimation was done substituting this albedo with the much lower value of 0.27, which was measured for the south-facing facade, to obtain a range of results.

Table 1 shows for each month of measurement the total radiation onto the wall-point simulated with SEBEpv, the absolute and relative difference to the measurements and two values for the single reflected wall-to-wall component assuming wall-albedos of 0.27 and 0.50, respectively. It should be noted, that those values are expected to have a rather large uncertainty, as the spatial distribution of the diffuse radiation component received by the north-facing facade is not known. Further, the reflectivity was determined by measurements pointing at the wall in between two windows. Thus, the albedo represents rather the reflectivity of the plaster material. If the facades' view-factor is reduced by the view-factor onto the windows, then the results lie in between the two shown values. From this comparison it can be concluded, that the neglected single reflection from the opposing wall is significant and may be in the magnitude of the difference between measurement and simulation.

Another aspect, as already indicated, is the choice of the reflectivity used for the estimations. Usually, the reflectivity is globally set to 0.2 (Gul et al., 2018; Thevenard and Haddad, 2006). As discussed before, the reflectivity of the different surfaces influence the reflected component. Further, the results still contain uncertainty that can be attributed to changes in reflectivity depending on time, season or weather condition the surfaces were exposed to Demain et al. (2013).

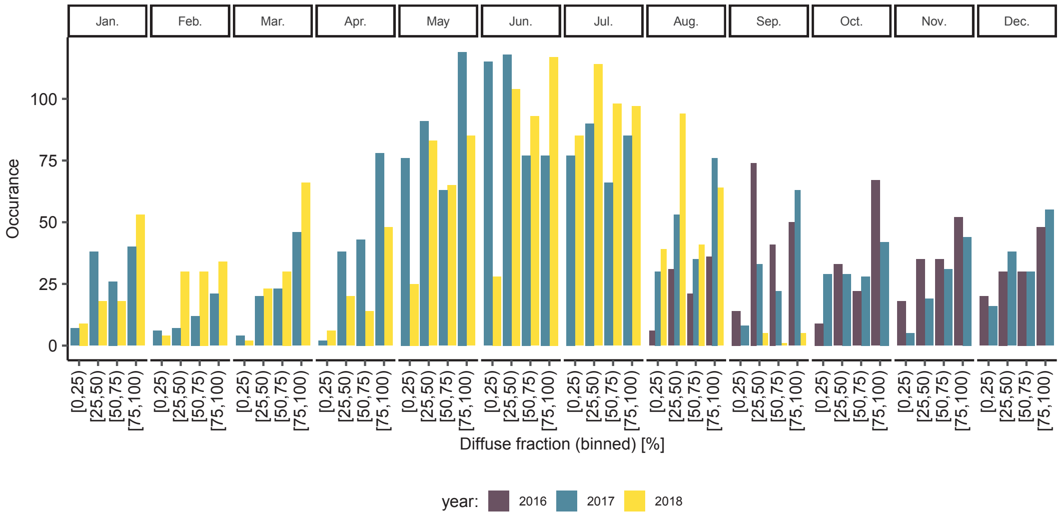

Fig. 11. Occurrence distribution of the diffuse fraction for each month and year of measurement.

4.4. Computation time

Total computation time is around 74 s per time stamp for a ground coverage of 265 × 245 pixels on an Intel i7 6700HQ @ 2.6 GHz (running between 3.2 and 3.3 GHz). The ground-reflected radiation onto walls is handled within about 6 s per time stamp. The reason for a rather long computation time, especially compared to SEBE (about 0.1 s per time step), is that SEBEpv was developed with the capability of estimating photovoltaic yields in addition to the solar resource, while SEBE was only developed for solar resource assessment.

To clarify the differences: SEBE is pre-processing solar irradiation by distributing DHI, DNI and the simplified reflected irradiation for each time step onto the 145 sky patches and summing the data over all time steps. In another step, the shadow pattern for all the 145 sky patch directions are determined for the given DSM. Finally, the incident irradiation onto the buildings' surfaces are calculated based on the pre-processed incoming irradiation and shadow pattern. For the calculation of PV yields, as done by SEBEpv in addition to the solar resource, the irradiation on the tilted surface as well as the respective ambient temperature are required for each time step. Therefore, irradiation cannot be pre-processed as in SEBE. Further, the implemented algorithm for estimating radiation reflected from the ground requires

Table 1
Irradiation at wall point simulated with SEBEpv. Comparison with measured values and radiation reflected from the opposing building (Exner Haus) estimated using the known view factor and different values of reflectivity α.

Year	Month	Total radiation	Difference to measurement		Reflected from opposing wall	
			Absolute	Relative	α = 0.27	α = 0.50
		[kWh m^{-2}]	[kWh m^{-2}]	[%]	[kWh m^{-2}]	[kWh m^{-2}]
2016	Aug.	37.8	−8.3	−18.1	1.2	2.3
	Sep.	57.2	−6.3	−9.9	1.5	2.8
	Oct.	10.8	−1.1	−9.4	1.0	1.9
	Nov.	4.5	−0.3	−7.1	0.6	1.1
	Dec.	3.7	−0.3	−7.0	0.5	0.9
2017	Jan.	2.7	−0.4	−12.6	0.4	0.7
	Feb.	2.4	−0.4	−13.6	0.3	0.5
	Mar.	39.5	−4.4	−10.0	1.5	2.7
	Apr.	45.8	−5.1	−10.1	1.9	3.6
	May	59.7	−2.2	−3.6	2.5	4.7
	Jun.	62.8	−2.2	−3.4	2.4	4.5
	Jul.	62.3	−3.0	−4.5	2.9	5.3
	Aug.	63.4	−8.0	−11.2	2.2	4.0
	Sep.	37.3	−1.6	−4.0	1.7	3.1
	Oct.	12.3	−3.3	−21.1	1.1	2.0
	Nov.	5.9	0.6	11.8	0.7	1.3
	Dec.	3.9	−0.3	−8.2	0.5	0.9
2018	Jan.	4.5	0.0	0.1	0.5	1.0
	Feb.	6.1	−0.6	−8.7	0.7	1.3
	Mar.	28.3	0.2	0.9	1.5	2.8
	Apr.	60.8	−9.6	−13.6	2.0	3.7
	May	65.6	−1.0	−1.4	3.4	6.3
	Jun.	51.1	2.6	5.3	2.8	5.1
	Jul.	63.8	−0.1	−0.2	2.6	4.9
	Aug.	64.8	−8.3	−11.3	2.7	5.0
	Sep.	21.0	−2.3	−10.0	0.9	1.6

completed processing of irradiation on the ground for each time step. Therefore, the two tools differ in the possibility of pre-processing data.

The algorithm of SEBEpv could be simplified to achieve better computational performance. However, using the same pre-processing concept as SEBE restricts SEBEpv to the estimation of the total irradiation potential on the building envelope. As a result, photovoltaic yields cannot be estimated with this tool, which is one of the purposes of SEBEpv. It is expected that the total computation time would be around double that of SEBE. While computation time of SEBE mainly scales with the size of the scenery domain, SEBEpv currently scales with the domain size times number of data points in the time series.

4.5. Comparison with other tools

Literature stating results of validation using measurements is rather scarce. SEBE was validated against measurements as shown in Lindberg et al. (2015) with a RMSE of 54.4 W/m^2 and R^2 of 0.93 for the irradiation at a wall. The reported scenario used for validation of SEBE differs from the one presented here, and results may differ significantly. Therefore, the irradiance onto the facades of the presented scenario was simulated using SEBE. The results from SEBE were compared to the ones from SEBEpv for the measurement point in front of the south-facing facade.

For that comparison, two clear sky days (21 and 22 August 2018) and two days with overcast sky (25 and 26 October 2016) were selected. The days were chosen to have a low variability in irradiance. Limiting the number of data points was necessary, because SEBE can only output the total sum over all data points and thus, starting simulations manually for each data point is required. The irradiance was simulated with a 10-min interval as described in Section 4.2. For the comparison, data points that were subjected to shade in the simulation, but not in reality and vice versa, were removed. Those data points produce outliers with strong impact on the statistical analysis and have similar influence on both tools due to their common shading algorithm.

For both tools the comparison of simulated and measured irradiance is shown in Fig. 12, in (a) for the clear sky days and in (b) for the overcast sky condition. SEBEpv shows a much lower RMSE and mean absolute error (MAE) than SEBE for both sky conditions and SEBE has a tendency for overestimation as shown in Section 3.4. During the clear sky period SEBEpv has a RMSE of 18.9 W/m^2 and a MAE of 10.6 W/m^2 compared to SEBE with 34.5 W/m^2 and 25.9 W/m^2, respectively. In Fig. 12(a) SEBE shows a step-like increase of irradiance, which is a result of how irradiance data is processed and only applies to the direct irradiance component. The irradiance components are assigned to each sky-patch according to their azimuth and elevation angle. Therefore, direct irradiance values of a few consecutive data points can be assigned to the same sky-patch and the azimuth and elevation angle of that sky-patch is then used in the simulation. Overall, the model performance of SEBEpv was significantly improved compared to SEBE and it can be concluded that both SEBE and SEBEpv profit from a higher resolution of sky-patches. Freitas et al. (2016) suggest dividing the hemisphere in 400 patches, although the resulting accuracy also depends on the accuracy of the DSM.

5. Conclusion

SEBEpv is a tool especially for estimating the irradiation on the building envelope in urban environments. It is based on its predecessor SEBE (Lindberg et al., 2015) and was improved with regard to estimating the radiation reflected from ground-surfaces onto the facades. The reflected radiation depends on the spatial distribution of irradiation on the ground, the view-factor, as well as on spatial variations of the ground's albedo.

In this study, for a point on an obstructed south-facing facade in Vienna, Austria, SEBEpv underestimates the irradiation on facades with an average bias of 7% and a standard deviation of about 29 W/m^2. To

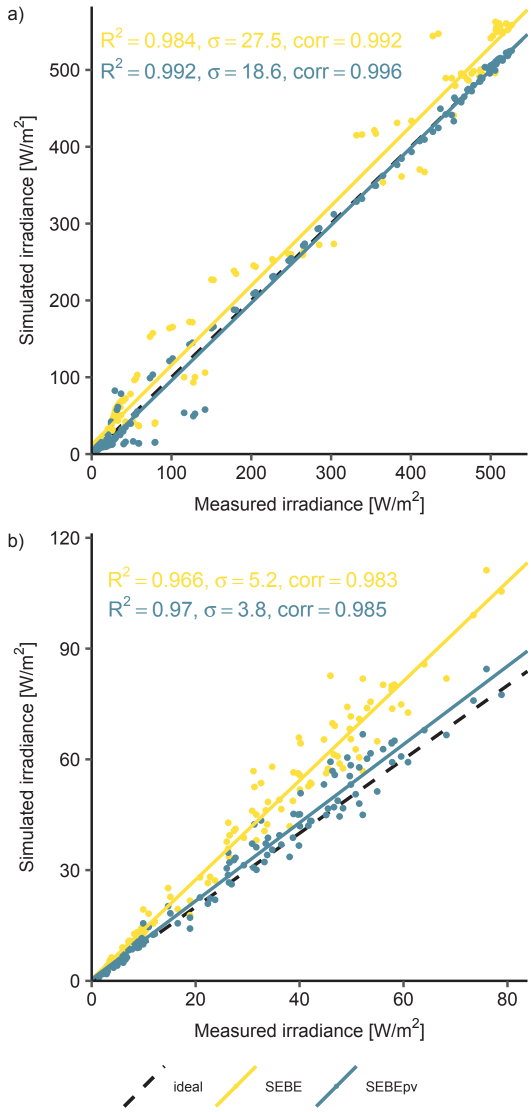

Fig. 12. Comparison of irradiance simulated with SEBE and SEBEpv, (a) for clear sky and (b) overcast sky. The results of both tools are shown versus the measured irradiance. The chosen clear sky days are 21 – 22 August 2018 and the days with overcast sky are 25 – 26 October 2016.

some extent, this bias error is caused by the rather low number of sky-patches used for the shadow casting. Overall, SEBEpv is considered to deliver pessimistic results by avoiding overestimating the reflected radiation inside an urban canyon.

Further validation based on measured irradiation at different heights at buildings as well as facade orientations and different locations is still recommended. For the future of SEBEpv, it is advisable to provide a second algorithm, only intended for solar radiation assessment, to reduce the computational time. This adaptation can turn SEBEpv to a very compatible tool for solar resource assessment on building facades in cities.

Declaration of Competing Interest

The authors declare that they have no known competing financial interests or personal relationships that could have appeared to influence the work reported in this paper.

Acknowledgements

The authors thank Fredrik Lindberg for his support understanding SEBE and his permission to use SEBE as basis for our work. The research leading to these results has received funding from Austria Research Promotion Agency (FFG), research programme “Stadt der Zukunft, 3. Ausschreibung 2015”, under grant agreement number 854691 (project: “PVOPTI-Ray”) and from “ACRP 8th call”, funded by the Klima und Energiefond (KliEN), under grant agreement number KR14AC7K11944 (project “URBANIA”).

References

Brito, M.C., Freitas, S., Guimarães, S., Catita, C., Redweik, P., 2017. The importance of facades for the solar PV potential of a Mediterranean city using LiDAR data. Renewable Energy 111, 85–94.
Calcabrini, A., Ziar, H., Isabella, O., Zeman, M., 2019. A simplified skyline-based method for estimating the annual solar energy potential in urban environments. Nat. Energy 4 (3), 206.
Catita, C., Redweik, P., Pereira, J., Brito, M.C., 2014. Extending solar potential analysis in buildings to vertical facades. Comput. Geosci. 66, 1–12.
Chatzipoulka, C., Compagnon, R., Kaempf, J., Nikolopoulou, M., 2018. Sky view factor as predictor of solar availability on building façades. Sol. Energy 170, 1026–1038.
Chatzipoulka, C., Compagnon, R., Nikolopoulou, M., 2016. Urban geometry and solar availability on façades and ground of real urban forms: using London as a case study. Sol. Energy 138, 53–66.
Demain, C., Journée, M., Bertrand, C., 2013. Evaluation of different models to estimate the global solar radiation on inclined surfaces. Renewable Energy 50, 710–721.
Dr. Valentin EnergieSoftware GmbH, 2013. PV∗SOL advanced Manual Version 6.0 – Design and Simulation of Photovoltaic Systems. https://www.valentin-software.com/sites/default/files/downloads/handbuecher/en/manual-eng_0.pdf (accessed on 2015-07-29).
EMS Brno, 2016. Global radiation sensor EMS 11. http://emsbrno.cz/r.axd/pdf_v_EMS11_u_pdf.jpg?ver= (accessed on 2016-08-16).
Erdélyi, R., Wang, Y., Guo, W., Hanna, E., Colantuono, G., 2014. Three-dimensional SOlar RAdiation Model (SORAM) and its application to 3-D urban planning. Sol. Energy 101, 63–73.
Freitas, S., Catita, C., Redweik, P., Brito, M.C., 2015. Modelling solar potential in the urban environment: State-of-the-art review. Renew. Sustain. Energy Rev. 41, 915–931.
Freitas, S.R., Cristovão, A.R., Amaro e Silva, R., Brito, M.C., 2016. Obstruction Surveying Methods for PV Application in Urban Environments. In: Proceedings of 32nd European Photovoltaic Solar Energy Conference and Exhibition. Munich, pp. 2759–2764. http://www.eupvsec-proceedings.com/proceedings?paper=37650.
Gul, M., Kotak, Y., Muneer, T., Ivanova, S., 2018. Enhancement of albedo for solar energy gain with particular emphasis on overcast skies. Energies 11 (11). https://www.mdpi.com/1996-1073/11/11/2881.
Hofierka, J., Zlocha, M., 2012. A New 3-D solar radiation model for 3-D city models. Trans. GIS 16 (5), 681–690.
Huld, T., Friesen, G., Skoczek, A., Kenny, R.P., Sample, T., Field, M., Dunlop, E.D., 2011. A power-rating model for crystalline silicon PV modules. Sol. Energy Mater. Sol. Cells 95 (12), 3359–3369.
Huld, T., Gottschalg, R., Beyer, H.G., Topic, M., 2010. Mapping the performance of PV modules, effects of module type and data averaging. Sol. Energy 84 (2), 324–338.
IEA, 2014. Technology Roadmap: Solar Photovoltaic Energy, 2014 edition. Tech. rep., OECD/IEA, Paris. https://www.iea.org/publications/freepublications/publication/technology-roadmap-solar-photovoltaic-energy—2014-edition.html.
Ineichen, P., Guisan, O., Perez, R., 1990. Ground-reflected radiation and albedo. Sol. Energy 44 (4), 207–214.
Jakica, N., 2018. State-of-the-art review of solar design tools and methods for assessing daylighting and solar potential for building-integrated photovoltaics. Renew. Sustain. Energy Rev. 81, 1296–1328.
Jakubiec, J.A., Reinhart, C.F., Jul. 2013. A method for predicting city-wide electricity gains from photovoltaic panels based on LiDAR and GIS data combined with hourly Daysim simulations. Sol. Energy 93, 127–143.
Kipp & Zonen, 2008. CHP 1 pyrheliometer - Instruction Manual. Version 0811. https://www.kippzonen.com/Download/202/CHP-1-Pyrheliometer-Manual.
Krawietz, S., Poortmans, J., Masson, G., Pause, F., Palm, J., Schlatmann, R., 2016. BIPV Position Paper – Building Integrated Photovoltaics (BIPV) as a core Element for Smart Cities.
Li, Y., Ding, D., Liu, C., Wang, C., 2016. A pixel-based approach to estimation of solar energy potential on building roofs. Energy Build. 129, 563–573.
Liang, J., Gong, J., Zhou, J., Ibrahim, A.N., Li, M., 2015. An open-source 3d solar radiation model integrated with a 3d Geographic Information System. Environ. Modell. Softw. 64, 94–101.
Liao, W., Heo, Y., 2017. A simplified vector-based method for irradiance prediction at urban scale. In: Proceedings of the 15th IBPSA Conference. vol. Building Simulation 2017. San Francisco, USA, pp. 2388–2397.
Lindberg, F., Grimmond, C.S.B., Gabey, A., Huang, B., Kent, C.W., Sun, T., Theeuwes, N.E., Järvi, L., Ward, H.C., Capel-Timms, I., Chang, Y., Jonsson, P., Krave, N., Liu, D., Meyer, D., Olofson, K.F.G., Tan, J., Wästberg, D., Xue, L., Zhang, Z., 2018. Urban Multi-scale Environmental Predictor (UMEP): An integrated tool for city-based climate services. Environ. Modell. Softw. 99, 70–87.
Lindberg, F., Jonsson, P., Honjo, T., Wästberg, D., 2015. Solar energy on building envelopes – 3D modelling in a 2D environment. Sol. Energy 115, 369–378.
Lorenzo, E., 2011. Energy Collected and Delivered to PV Modules. In: Handbook of Photovoltaic Science and Engineering, 2nd ed. Wiley, pp. 984–1042.
Lukac, N., Žlaus, D., Seme, S., Žalik, B., Štumberger, G., 2013. Rating of roofs' surfaces regarding their solar potential and suitability for PV systems, based on LiDAR data. Appl. Energy 102, 803–812.
Machete, R., Falcão, A.P., Gomes, M.G., Moret Rodrigues, A., 2018. The use of 3d GIS to analyse the influence of urban context on buildings' solar energy potential. Energy Build. 177, 290–302.
Mohajerani, A., Bakaric, J., Jeffrey-Bailey, T., 2017. The urban heat island effect, its causes, and mitigation, with reference to the thermal properties of asphalt concrete. J. Environ. Manage. 197, 522–538.
Olefs, M., Baumgartner, D.J., Obleitner, F., Bichler, C., Foelsche, U., Pietsch, H., Rieder, H.E., Weihs, P., Geyer, F., Haiden, T., Schöner, W., 2016. The Austrian radiation monitoring network ARAD – best practice and added value. Atmos. Meas. Tech. 9 (4), 1513–1531.
Perez, R., Seals, R., Michalsky, J., 1993. All-weather model for sky luminance distribution—preliminary configuration and validation. Sol. Energy 50 (3), 235–245. http://www.sciencedirect.com/science/article/pii/0038092X9390017I.
QGIS Development Team, 2019. QGIS Geographic Information System. Open Source Geospatial Foundation, http://qgis.org.
Qin, Y., 2015. Urban canyon albedo and its implication on the use of reflective cool pavements. Energy Build. 96, 86–94.
Ratti, C., Richens, P., 2004. Raster analysis of urban form. Environ. Plann. B: Plann. Des. 31 (2), 297–309.
Redweik, P., Catita, C., Brito, M., 2013. Solar energy potential on roofs and facades in an urban landscape. Sol. Energy 97, 332–341.
Reindl, D., Beckman, W., Duffie, J., 1990. Diffuse fraction correlations. Sol. Energy 45 (1), 1–7. http://www.sciencedirect.com/science/article/pii/0038092X9090060P.
Revesz, M., Oswald, S.M., Trimmel, H., Weihs, P., Zamini, S., 2018. Potential increase of solar irradiation and its influence on PV facades inside an urban canyon by increasing the ground-albedo. Sol. Energy 174, 7–15.
Robinson, D., Stone, A., 2004. Solar radiation modelling in the urban context. Sol. Energy 77 (3), 295–309.
Romero Rodríguez, L., Duminil, E., Sánchez Ramos, J., Eicker, U., 2017. Assessment of the photovoltaic potential at urban level based on 3d city models: a case study and new methodological approach. Sol. Energy 146, 264–275.
Sa PVsyst, 2012. PVsyst 5.21 Contextual Help. http://files.pvsyst.com/pvsyst5.pdf (accessed on 2015-07-29).
Santamouris, M., 2014. Cooling the cities – a review of reflective and green roof mitigation technologies to fight heat island and improve comfort in urban environments. Sol. Energy 103, 682–703.
Taha, H., 1997. Urban climates and heat islands: albedo, evapotranspiration, and anthropogenic heat. Energy Build. 25 (2), 99–103.
Thevenard, D., Haddad, K., 2006. Ground reflectivity in the context of building energy simulation. Energy Build. 38 (8), 972–980.
Šúri, M., Hofierka, J., 2004. A new GIS-based solar radiation model and its application to photovoltaic assessments. Trans. GIS 8 (2), 175–190.
Šúri, M., Huld, T.A., Dunlop, E.D., 2005. PV-GIS: a web-based solar radiation database for the calculation of PV potential in Europe. Int. J. Sustain. Energ. 24 (2), 55–67.
Waibel, C., Evins, R., Carmeliet, J., 2017. Efficient time-resolved 3d solar potential modelling. Sol. Energy 158, 960–976.
Walton, G.N., 2002. Calculation of Obstructed View Factors by Adaptive Integration. Technical Report NISTIR 6925, National Institute of Standards and Technology, Gaithersburg, US.

4.3 Publication III

PVOPTI-RAY: OPTIMISATION OF REFLECTING MATERIALS AND PHOTOVOLTAIC YIELD IN AN URBAN CONTEXT

https://doi.org/10.4229/EUPVSEC20172017-6DO.11.4

PVOPTI-RAY: OPTIMISATION OF REFLECTING MATERIALS AND PHOTOVOLTAIC YIELD IN AN URBAN CONTEXT

Michael Revesz [1,2], Sandro Oswald [2], Heidelinde Trimmel [2], Astrid Schneider [1], Philipp Weihs [2], Shokufeh Zamini [1,] ,
Martin Peyerl [3], Stefan Krispel [3]

[1] AIT Austrian Institute of Technology GmbH, Center for Energy, Photovoltaic Systems, Giefinggasse 2, 1210 Vienna, Austria
[2] University of Natural Resources and Life Sciences, Department of Water-Atmosphere-Environment, Institute of Meteorology, Gregor-Mendel-Straße 33, 1180 Vienna, Austria
[3] Smart Minerals GmbH

ABSTRACT: Within the project “PVOPTI-Ray”, the effect of increasing the albedo of streets and building façades on the yield of building integrated photovoltaic (BIPV) systems, the comfort of pedestrians and the air temperature in the canyon were investigated. The aim was to find an optimised solution (with regard to the structure of an urban canyon and properties of surface materials on streets and buildings), where the yield of directly and indirectly integrated Photovoltaic (PV) is increased and the comfort of pedestrians is maintained within defined limits. Making use of reflected irradiation can improve the yield of BIPV systems on façades and increase their attractiveness inside cities. An existing software tool had to be improved regarding the ground reflected irradiance. Simulations show that increasing the ground albedo from 0.13 to 0.56 can increase the PV yield by around 25 % on building façades over one year. Measurements at increased ground albedo of 0.75 for a limited area of only ~20 m^2 in front of PV modules showed an increased PV yield by ~13 % during a clear sky day. The thermal comfort of pedestrians is not deteriorated by the installation of PV on building façades. However, larger albedo increases the heat stress in summer.

Keywords: Building Integrated PV (BIPV), Ground Albedo, Urban, PV Yield Modelling, Human Comfort

1 INTRODUCTION

While research in Photovoltaic (PV) and urban climate modelling is already quite advanced, the interaction of Building Integrated Photovoltaic (BIPV) in cities and urban climate has not yet received the required attention. In addition, city planners search for solutions to increase renewable energy production inside cities. Besides roofs, also building facades can be used for the installation of PV systems. Making use of reflected irradiation can improve the yield of BIPV systems on façades and make them a more attractive solution inside cities.

Within the project “PVOPTI-Ray”, the effect of increasing the albedo of streets and building façades on the yield of BIPV systems and the thermal comfort of pedestrians was investigated (see the mutual influences in Fig. 1). The aim was to find an optimised solution (with regard to the structure of an urban canyon and properties of surface materials on streets and buildings), where the yield of directly and indirectly integrated PV is increased and the comfort of pedestrians is maintained within defined limits. The latter is very important in case of urban heat island effects, since additional heat stress on the human body should be avoided. While significantly larger yield could be achieved by using highly reflecting concrete for streets instead of dark asphalt, this gain could be at the cost of human comfort. Increased reflections of visible irradiation onto the human body could lead to both, thermal and visual stress [1, 2].

For this case study an improved model, with respect to the estimation of ground reflected irradiance, was required. Further, it was desired to use tools with comparably low computation time.

In the following, the main idea of the improved model and the results concerning the effect on PV yield for selected scenarios are presented. While the focus of this work is the PV yield on building facades, few results regarding the thermal stress on pedestrians will be presented in order to raise awareness of the implications.

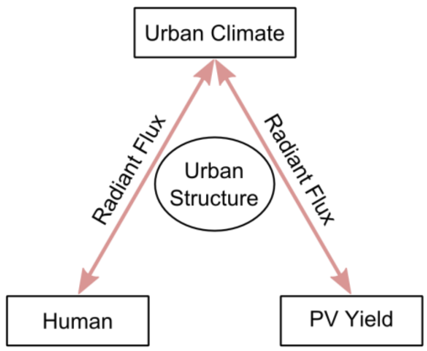

Figure 1: Mutual influences investigated in the project “PVOPTI-Ray”.

2 MODEL ADVANCEMENT

In order to investigate and simulate the impact of ground reflected irradiance on the PV yield in an urban environment an adequate model is required. Raytracing methods might be quite accurate. However, computation time is high and therefore not suitable for simulating urban districts. Suitable options are GIS-based methods. GIS data is available for bigger cities and raster-based calculations can be performed rather fast [3].

For the estimation of PV yield on the building envelope, the open-source software SEBE (Solar Energy on Building Envelopes) was adopted [3]. SEBE is part of the simulation package UMEP (Urban Multi-scale Environmental Predictor), which is used for urban environmental simulations and uses digital surface models (DSMs) as input data for urban areas [4]. Since SEBE is used to estimate the solar energy on building surfaces, it was extended with a simple PV model, by Huld et al., for PV yield estimation [5, 6].

As it was the goal to estimate the change in PV yield on buildings in an urban canyon depending on the albedo of the ground surfaces, the estimation of ground reflected irradiation needed to be revised. The usual approach is very simplified (see Eq. (1)) and based on the assumption that the inclined surface receives ground reflected irradiance (G_{gr}) from a surface of infinite extent:

$$G_{gr} = G_0 \alpha \frac{1}{2}(1 - \cos(\beta)) \tag{1}$$

where G_0 is the global horizontal irradiance, α is the ground albedo and β is the receiving surface's inclination [7]. This method is justified for the reason that usually the albedo is rather low and on a surface with the usual tilt the last term in Eq. (1) is small as well. Thus, the contribution of ground reflections to the total irradiation is very small, more detailed models are not required and multiple reflections are neglected [8].

However, this does not hold for an urban canyon. For a vertical façade the last term of Eq. (1) becomes largest. On the other hand, opposite buildings block the view onto an infinite ground plane. Since it was intended to estimate the potential influence of different ground albedo on the yield of BIPV on facades inside an urban canyon, better models are required and can be justified.

The proposed improvement can be applied, because the simulation tool in use is working in a raster space. The new method for the ground reflected irradiance is to sum over visible ground sections as in Eq. (2):

$$G_{gr} = \frac{G_0}{p} \alpha \sum_{i}^{p} P_i \tag{2}$$

where p is the number of patches of the possibly visible hemisphere for a wall pixel and P_i is the wall-hemisphere patch from which direction ground pixels are visible. The latter represents a boolean value, 1 for visible to the wall pixel and 0 for invisible.

Nevertheless, even with this approach and the given tool, some simplifications have been required. For one, shadowed ground pixels contribute with reflectance of the full horizontal irradiance as if not being shadowed. On the other hand, reflections from opposite building walls are neglected. Further, it was not yet possible to implement the angular view factor between receiving wall pixel and reflecting ground pixel. Still, this approach is a better estimation compared to the use of Eq. (1).

3 URBAN SCENARIOS

For investigating the gain of PV yield on a building façade, the following scenarios and parameters were considered:

- Basic geometric urban structures:
  - Street/intersection, square.
  - Typical wall-height to street-width.
- Most common or promising PV-module types (crystalline Si, CI(G)S).
- Different materials for pavement and façades (distinguished by albedo and emissivity).

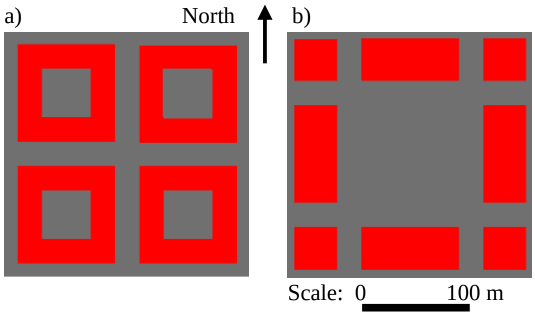

Figure 2: Land cover scheme of two scenarios, a) street canyon with intersection, b) buildings surrounding a small square. Grey: street, red: buildings. The street width is 20 m, building height 20 m.

The emissivity is not relevant for PV yield simulations, but used for the simulations related to urban climate. The scenarios were mainly based on typical urban canyons in Vienna. For each scenario different combinations of pavement and building materials with different properties (i.e. albedo and emissivity) were simulated and compared. Since it was not possible to implement ground areas with different values of albedo, the effect of vegetation as a ground surface is not simulated. Further, measurements at real sites are used for a comparison with the modelling results.

The two urban structures presented here represent a street canyon and an intersection at the centre (Fig. 2a) and buildings surrounding a smaller sized square (Fig. 2b). In both cases, a flat roof is assumed with a building height of 20 m. The street width is 20 m as well.

For each building scenario the ground albedo was set to 0.13 (typical for asphalt streets) and for comparison to 0.56 (possible with very bright concrete). The PV yield was estimated under those conditions for the PV technologies of crystalline silicon and CI(G)S. A hot clear sky day (09. June 2017) and a cloudy day (16. June 2017) were selected for the assessments. In addition, the PV yield over one year (1. September 2016 – 31. August 2017) was estimated. All weather data was measured in Vienna.

4 RESULTS

4.1 Model improvement

For the comparison of the original algorithm for calculating the irradiation on building walls with and the new algorithm to calculate the irradiation on building walls, the following situation is assumed: The two scenarios are A (street canyon, see Fig. 2a) and B (square, see Fig. 2b). The irradiance data used is arbitrarily chosen and for 1 hour around 10:00 CET at a clear sky day (09. June 2017) in June in Vienna. Table I shows the summary of estimated irradiations for a south and east facing wall. In all cases the average of the top 6 meters is taken.

For the two selected wall points, the irradiation predicted with the original algorithm is 7 – 9 % larger than with the new algorithm. Further, one can see that the irradiation estimated by the old algorithm is equal independent of the urban structure, i.e. street canyon or square. This shows that the area of ground, which is visible to each wall segment, is not taken into account. In addition, the irradiation on a wall decreases along its height as it is expected.

Table I: Comparison of the old and new algorithm for estimation of irradiation at selected wall points for 1 hour around 10:00 CET of a clear day in June.

Scenario	Wall orientation	old [kWh/m^2]	new [kWh/m^2]
B (square)	East	0.590	0.551
	South	0.390	0.359
A (street)	East	0.590	0.531
	South	0.390	0.340

Nevertheless, this improvement comes with an increase in computation time. The implementation of the PV model increased the computation time by a factor in the magnitude of the number of meteorological data points. In addition, the calculation time is increased by the better ground reflection algorithm.

4.2 PV yield increase

It is obvious that the PV yield increases if the ground reflected component is increased artificially, by altering the ground surface materials or even the facades to brighter colours. However, it is interesting to know quantitative by how much the PV yield could be increased in an urban canyon. In this chapter, this gain is presented for the two defined scenarios. Fig. 3 and Fig. 4 show the time series of the irradiance, which are used for the estimation of PV yield. Both represent the chosen days in Vienna, one cloudy day (16. June 2017) and one clear day (09. June 2017) respectively.

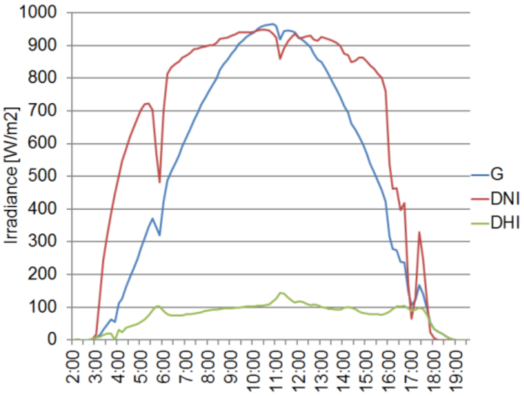

Figure 3: Irradiance profile in W/m^2 for a **clear** day used for estimations. Global horizontal irradiance (G) and direct normal irradiance (DNI) are measured values, diffuse horizontal irradiance (DHI) is estimated.

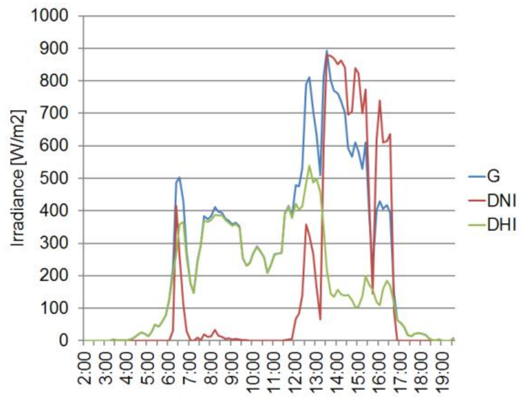

Figure 4: Irradiance profile in W/m^2 for a **cloudy** day used for estimations. Global horizontal irradiance (G) and direct normal irradiance (DNI) are measured values, diffuse horizontal irradiance (DHI) is estimated.

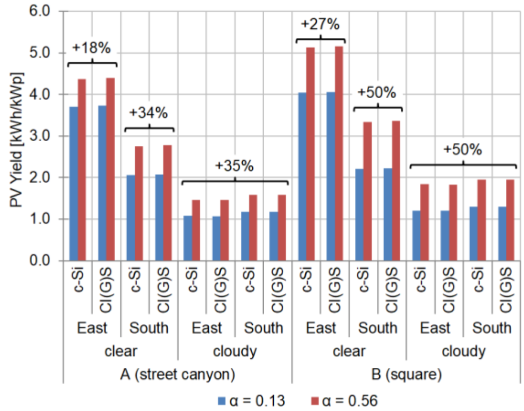

Figure 5: PV yield during one day in summer for each case of building scenario, ground albedo, weather condition and PV technology. Red: south facing wall, blue: east facing wall.

Table II: PV yield [kWh/kWp] on selected wall segments/orientations for 1 year of weather data in scenario B. Varied parameters: PV cell technology and albedo.

	$\alpha = 0.13$		$\alpha = 0.56$	
technology	**south**	**east**	**south**	**east**
c-Si	698	583	872	755
CI(G)S	706	594	879	765

During both selected days, the weather in the afternoon differs from the dominating weather condition. I.e. the afternoon of the clear sky day becomes cloudy and the cloudy day becomes scattered. Therefore, the results for the east facing wall represent the main weather condition of each day the best. In contrast, the south facing wall is exposed to a mixture of sky conditions and the corresponding results might be misleading in regards to the weather condition.

The results shown in Fig. 5 reveal the following findings: In general, it is of advantage, if a PV-façade installation is mounted on buildings at a square compared to at streets. In case of the chosen scenarios the much bigger ground surface of the square causes around double the gain compared to the street.

Further, during clear sky the gain by ground reflections is rather small compared to cloudy sky. In specific, the increase of ground albedo from 0.13 to 0.56 for a wall along a street results in a larger yield of around 18 % for the clear sky day. In contrast, for the cloudy sky condition the gain is even 36 %. This is clear as at clear sky the irradiance directly from the sun is much more dominant compared to the reflected components of irradiation. Despite the larger relative gain at cloudy sky, the absolute yield is very low. The south wall shows almost equal relative gains independent of the sky condition. This is because during each of the chosen days both weather conditions occur.

Simulations over one year of data show with increased albedo a gain of around 24 – 29 % for both considered PV technologies. For a south facing wall, the

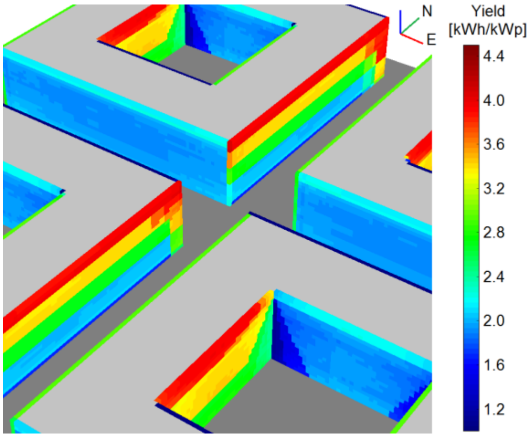

Figure 6: PV yield on façades, ground albedo is 0.13; simulated for the clear day, c-Si technology. The roof and ground are coloured in grey.

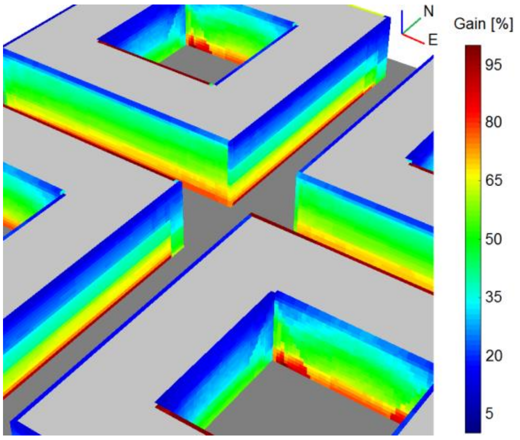

Figure 7: Gain of PV yield as a result of increasing the ground albedo from 0.13 to 0.56; simulated for the clear day, c-Si technology. The roof and ground are coloured in grey.

gain is slightly lower than for other orientations towards east or west. The absolute PV yield values for each case chosen are shown in Table II.

In case of the one-day course, the two PV cell technologies show very similar behaviour independent of the sky condition. Over a period of one year, CI(G)S technology has also no significant advantage over crystalline silicon technology when used as a façade integrated installation. Therefore, no technological preference for a PV installation in an urban environment on façades is given.

Fig. 6 shows the PV yield, in the case of a ground albedo of 0.13, on façades in an urban canyon. Fig. 7 shows the gain of yield as a result of increasing the albedo from 0.13 to 0.56. Nevertheless, for the decision where on a building a PV plant should be installed and where not, it remains important to assess not only the gain, but also the yield.

Measurements at a site which is similar to scenario A (street canyon) were taken. There the effect of a highly reflecting area in front of irradiance sensors and PV panels was tested. The street (asphalt) has an albedo of 0.13. For the measurement with higher albedo a white surface covering 29 m^2 (max. 9m x 3.7m), made of white

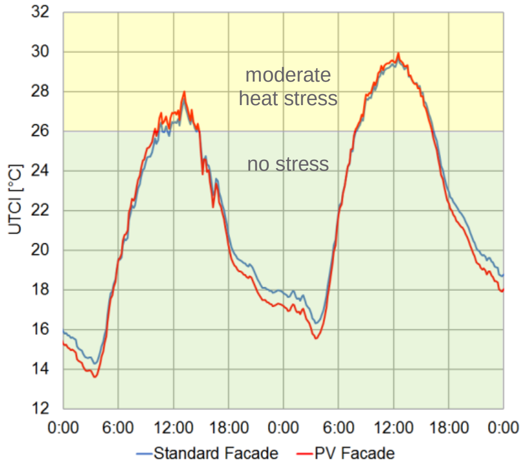

Figure 8: Thermal stress: UTCI for two consecutive hot summer days (07.-08. Aug. 2016, Vienna). Comparison of standard thermal insulated versus PV façade.

painted panels, have been installed. The measured albedo was 0.75. For a clear sky day in August, the white area caused an increased yield of ~13 % during most of the day. Only in the morning and the afternoon the yield dropped due to shadowing. Given, that the measurement plane was facing to the south and the white surface is rather small compared to the total street surface (370 m^2 central, plus 200 m^2 on sides), the simulated results seem plausible.

Concerning the optimization of surfaces inside an urban canyon regarding maximum PV yield, one can say: For the optimum scenario, all surfaces should be reflecting 100 %. However, the optimum is limited by the technical feasibility to produce surfaces as well as the human comfort. The latter concerns mainly the visual comfort due to glare, which was not assessed in this study. Another important criterion is the thermal comfort and the climatic effects.

4.3 Human comfort

One measure for the thermal comfort of humans is the so called Universal Thermal Climate Index (UTCI). This measure is influenced mainly by the air temperature, wind speed, humidity, the visible part of irradiation and the infrared portion of the irradiance. The UTCI is given in units of °C and representing the air temperature of a reference condition which causes the equivalent thermal stress [9].

Fig. 8 shows simulations, using TEB [10], and comparing building façades with thermal insulation as it is usual standard in Austria versus an insulated façade with BIPV installation. The two days shown are hot summer days (07. – 08. August 2016) in Vienna. While during the day the UTCI is slightly increased with PV installation, during night time the UTCI is around 1°C lower. This is mainly because of the relatively large emissivity of the PV module.

In contrast, increasing the ground albedo in an urban canyon has a larger effect in the thermal comfort of pedestrians (see Fig. 9). The higher amount of irradiance reflected onto the human body is increasing the UTCI, especially at clear sky condition in the direct sun. In the graph two times per day the UTCI changes immense: At around 6:00 in the morning, when a building shadow passes the test point and exposes it to the direct sun. And

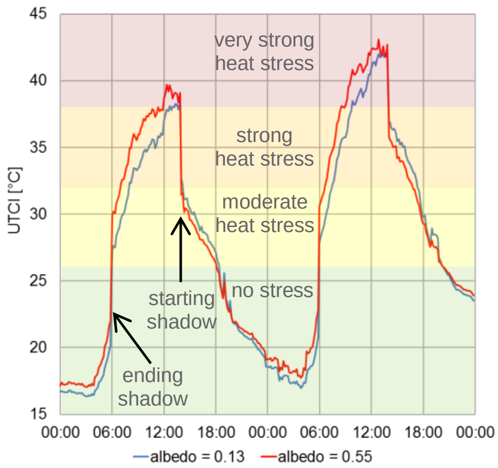

Figure 9: UTCI for two consecutive hot summer days (19.-20. June 2017, Vienna). Comparison of ground surface albedo of 0.13 versus 0.55.

later, at around 14:30, the test point lies in shadow again. However, for the following afternoon hours the UTCI for the darker ground surface is larger than for the brighter surface. The darker surface is heated up more and is

therefore emitting more infrared radiation. Once the darker surface has cooled down enough, the UTCI is again lower compared to the brighter surface.

It was not possible to assess the visual comfort for humans in the situation of high reflecting surfaces. However, it is expected that the visual stress will increase. Though, the extent of disturbance remains un-quantified.

5 CONCLUSIONS

It was found that it is technically possible and feasible to produce street surfaces with an albedo of up to 0.56. The effect of such higher reflecting surfaces in an urban canyon on the PV yield as well as the human comfort, compared to usual ground surfaces with an albedo of 0.13, was investigated.

Inside an urban canyon with a building-height to street-width ratio of 1:1 (20 m:20 m), which is typical for e.g. Vienna, the increase of ground albedo from 0.13 to 0.56 is expected to increase the PV yield by around 18 % for an east facing wall under clear sky condition. Over one year under typical Viennese weather conditions it was estimated, that the PV yield would be around 24 – 29 % larger for the same increase of reflectivity.

Therefore, it can be concluded, that BIPV on façades in an urban environment can significantly benefit from optimizing the albedo of surrounding surfaces. Further, it was concluded, that thinfilm PV technologies such as CI(G)S based ones have no benefit compared to crystalline silicon technologies under the given location and climatic condition.

Simulations of the human comfort showed, that the assessment of thermal stress on a pedestrian passing a BIPV installation and walking on a higher reflecting pavement is complex. While the thermal stress during a hot summer day is not much increased, different changes to the urban landscape have negative, but also positive effects. Many aspects, (e.g. albedo, thermal storage or shading), but also the climatic condition have to be considered for a well-made decision.

For a more accurate assessment of the PV yield it is suggested that the algorithms for estimating reflected irradiance will be further improved. E.g. the view-factor and the shaded ground surfaces should be considered in the model. Nevertheless, this case study shows that it is reasonable to install BIPV on façades in cities.

6 ACKNOWLEDGEMENT

The research leading to these results has received funding from the energy research programme (Stadt der Zukunft 3. Ausschreibung 2015) under grant agreement number 854691.

Many thanks to Fredrik Lindberg for his support with UMEP.

7 REFERENCES

[1] H. Lee, H. Mayer, D. Schindler, Importance of 3-D radiant flux densities for outdoor human thermal comfort on clear-sky summer days in Freiburg,Southwest Germany, Meteorologische Zeitschrift 23 **3** (2014) 315–330.

[2] R. Compagnon, J. Goyette-Pernot, Visual Comfort in Urban Spaces. In: RUROS – Rediscovering the Urban Realm and Open Spaces, Co-ordinated by CRES, Department of Buildings. http://alpha.cres.gr/ruros/ (2004)

[3] F. Lindberg, P. Jonsson, T. Honjo, et al., Solar energy on building envelopes – 3D modelling in a 2D environment, Sol. Energy 115 (2015) 369–378.

[4] F. Lindberg, C.S.B Grimmond, A. Gabey, et al., UMEP - An integrated tool for city-based climate services. Submitted to Environmental Modelling and Software. (2017)

[5] T. Huld, G. Friesen, A. Skoczek, et al., A power-rating model for crystalline silicon PV modules, Sol. Energy Mater. Sol. Cells 95 **12** **(**2011) 3359–3369.

[6] T. Huld, R., Gottschalg, H.G., Beyer, et al., Mapping the performance of PV modules, effects of module type and data averaging, Sol. Energy 84 **2** **(**2010) 324–338.

[7] H. Häberlin, Photovoltaik - Strom aus Sonnenlicht für Verbundnetz und Inselanlagen, VDE Verlag (2007).

[8] L. Eduardo, Energy Collected and Delivered to PV Modules, Handbook of Photovoltaic Science and Engineering, Wiley, 2nd Ed., pp. 984–1042.

[9] P. Bröde, D. Fiala, K. Blazejczyk, et al., Calculating UTCI Equivalent Temperatures, 13th Intl. Conf. on Environmental Ergonomics (2009)

[10] V. Masson, A physically-based scheme for the urban energy budget in atmospheric models, Bound-Layer Meteorol. 94 (2000) 357–397.

5 Conference Contributions

5.1 Poster Contributions

PV Tagung 2016, Villach (Austria): results from the measurements and evaluation of surface reflectivities.

5.2 Oral Presentations

- EUPVSEC 2017, Amsterdam: see Publication III.

- EGU 2019, Vienna: see Publication I.

6 Other Contributions

Contributions in other publications that are not part of this PhD (for copies see the Appendix A):

S. M. Oswald, M. Revesz, H. Trimmel, P. Weihs, S. Zamini, A. Schneider, M. Peyerl, S. Krispel, H. E. Rieder, E. Mursch-Radlgruber, and F. Lindberg: Coupling of urban energy balance model with 3–D radiation model to derive human thermal (dis)comfort. *Int J Biometeorol.* 2019. 63(6):711–722.

H. Trimmel, P. Weihs, S. Faroux, H. Formayer, P. Hamer, K. Hasel, J. Laimighofer, D. Leidinger, V. Masson, I. Nadeem, S. M. Oswald, M. Revesz, and R. Schoetter. Thermal conditions during heat waves of a mid-European metropolis under consideration of climate change, urban development scenarios and resilience measures for the mid-21st century. *Meteorologische Zeitschrift*, 2019. doi: 10.1127/metz/2019/0966. URL `ttps://www.schweizerbart.de/papers/metz/detail/prepub/91938/Thermal_conditions_during_heat_waves_of_a_mid_Euro?af=crossref`.

H. Trimmel, P. Weihs, S. Faroux, H. Formayer, C. Gützer, K. Hasel, D. Leidinger, A. Lemonsu, V. Masson, I. Nadeem, S. Oswald, M. Revesz, and R. Schoetter. Influence of urban growth of the city Vienna on the thermal comfort of its habitants. [Poster] [EGU General Assembly 2019, Vienna, 7.-12. April 2019], *Geophysical Research Abstracts*, 21, 14726–14726.

References

C. Ahrens. *Meteorology Today*. Brooks Cole, 9ed edition, 2008. ISBN 0495555738,9780495555735.

A. Calcabrini, H. Ziar, O. Isabella, and M. Zeman. A simplified skyline-based method for estimating the annual solar energy potential in urban environments. *Nature Energy*, 4(3):206, Mar. 2019. ISSN 2058-7546. doi: 10.1038/s41560-018-0318-6.

C. Chatzipoulka, R. Compagnon, and M. Nikolopoulou. Urban geometry and solar availability on façades and ground of real urban forms: using London as a case study. *Solar Energy*, 138:53–66, Nov. 2016. ISSN 0038-092X. doi: 10.1016/j.solener.2016.09.005.

C. Chatzipoulka, R. Compagnon, J. Kaempf, and M. Nikolopoulou. Sky view factor as predictor of solar availability on building façades. *Solar Energy*, 170:1026–1038, Aug. 2018. ISSN 0038-092X. doi: 10.1016/j.solener.2018.06.028.

C. Demain, M. Journée, and C. Bertrand. Evaluation of different models to estimate the global solar radiation on inclined surfaces. *Renewable Energy*, 50:710–721, Feb. 2013. ISSN 0960-1481. doi: 10.1016/j.renene.2012.07.031.

Dr. Valentin EnergieSoftware GmbH. PV*SOL advanced Manual Version 6.0 – Design and Simulation of Photovoltaic Systems, 2013. URL `https://www.valentin-software.com/sites/default/files/downloads/handbuecher/en/manual-eng_0.pdf`. accessed on 2015-07-29.

E. Dvorak. PV im dicht verbauten Gebiet - Treiber und Hemmnisse aus Sicht der Stadt Wien, June 2016. URL `http://tppv.at/tppv/wp-content/uploads/2016/07/06_Dvorak_PV-im-dichtverbauten-Gebiet.pdf`.

H. Fechner, C. Mayr, A. Schneider, M. Rennhofer, and G. Peharz. Technologie-Roadmap für Photovoltaik in österreich. Report for energy and environmental research 15/2016, Bundesministerium für Verkehr, Innovation und Technologie, Austria, Vienna, Austria, June

2016. URL https://nachhaltigwirtschaften.at/resources/edz_pdf/1615_technologie_roadmap_photovoltaik.pdf.

S. Freitas, C. Catita, P. Redweik, and M. C. Brito. Modelling solar potential in the urban environment: State-of-the-art review. *Renewable and Sustainable Energy Reviews*, 41:915–931, Jan. 2015. ISSN 1364-0321. doi: 10.1016/j.rser.2014.08.060.

C. A. Gueymard. Direct and indirect uncertainties in the prediction of tilted irradiance for solar engineering applications. *Solar Energy*, 83(3):432 – 444, 2009. ISSN 0038-092X. doi: http://dx.doi.org/10.1016/j.solener.2008.11.004. URL http://www.sciencedirect.com/science/article/pii/S0038092X08002983.

J. Hofierka and M. Zlocha. A New 3-D Solar Radiation Model for 3-D City Models. *Transactions in GIS*, 16(5):681–690, 2012. ISSN 1467-9671. doi: 10.1111/j.1467-9671.2012.01337.x.

T. Huld and A. Amillo. Estimating PV Module Performance over Large Geographical Regions: The Role of Irradiance, Air Temperature, Wind Speed and Solar Spectrum. *Energies*, 8(6):5159–5181, June 2015. doi: 10.3390/en8065159.

T. Huld, R. Gottschalg, H. G. Beyer, and M. Topič. Mapping the performance of PV modules, effects of module type and data averaging. *Solar Energy*, 84(2):324–338, Feb. 2010. ISSN 0038-092X. doi: 10.1016/j.solener.2009.12.002.

T. Huld, G. Friesen, A. Skoczek, R. P. Kenny, T. Sample, M. Field, and E. D. Dunlop. A power-rating model for crystalline silicon PV modules. *Solar Energy Materials and Solar Cells*, 95(12):3359–3369, Dec. 2011. ISSN 0927-0248. doi: 10.1016/j.solmat.2011.07.026.

IEA. Technology Roadmap: Solar Photovoltaic Energy, 2014 edition. Technical report, OECD/IEA, Paris, 2014. URL https://www.iea.org/publications/freepublications/publication/technology-roadmap-solar-photovoltaic-energy---2014-edition.html.

IEA. IEA-PVPS Annual Report 2018. Technical report, IEA International Energy Agency, July 2019. URL `http://www.iea-pvps.org/index.php?id=6&eID=dam_frontend_push&docID=4827`. ISBN 978-3-90642-84-8.

P. Ineichen, O. Guisan, and R. Perez. Ground-reflected radiation and albedo. *Solar Energy*, 44(4):207–214, Jan. 1990. ISSN 0038-092X. doi: 10.1016/0038-092X(90)90149-7. URL `http://www.sciencedirect.com/science/article/pii/0038092X90901497`.

N. Jakica. State-of-the-art review of solar design tools and methods for assessing daylighting and solar potential for building-integrated photovoltaics. *Renewable and Sustainable Energy Reviews*, 81:1296–1328, Jan. 2018. ISSN 1364-0321. doi: 10.1016/j.rser.2017.05.080.

D. King, J. Kratochvil, W. Boyson, and W. Bower. Field Experience With A New Performance Characterization Procedure For Photovoltaic Arrays. In *Proc. 2nd World Conf. and Exhib. on Photovolt. Sol. Energy Conv.*, pages 1947–1952, Vienna, 1998.

D. King, W. Boyson, and J. Kratochvil. Photovoltaic Array Performance Model. Technical Report Report SAND2004-3535, Sandia National Laboratories, 2004.

S. Krawietz, J. Poortmans, G. Masson, F. Pause, J. Palm, and R. Schlatmann. BIPV Position Paper - Building Integrated Photovoltaics (BIPV) as a core Element for Smart Cities, Dec. 2016.

B. Kubicek, G. Mütter, Y. Voronko, and T. Krametz. Using an Optimized Analytic Predictor as an Error Indicator in Multi-Megawatt PV-Plants. In *Proc. 29th Eur. Photovolt. Sol. Energy Conf. and Exhib.*, pages 2609–2611, Amsterdam, 2014. ISBN 3-936338-34-5. doi: 10.4229/EUPVSEC20142014-5BV.1.13.

F. Lindberg, P. Jonsson, T. Honjo, and D. Wästberg. Solar energy on building envelopes – 3D modelling in a 2D environment. *Solar Energy*, 115: 369–378, May 2015. ISSN 0038-092X. doi: 10.1016/j.solener.2015.03.001.

Magistrat der Stadt Wien. Energie! voraus - Energiebericht der Stadt Wien. Technical report, Magistrat der Stadt Wien, Magistratsabteilung 20 - Energieplanung, Vienna, 2019. URL `https://www.wien.gv.`

at/stadtentwicklung/energie/pdf/energiebericht2019.pdf. Daten 2017/Berichtsjahr 2019.

H. Malberg. *Meteorologie und Klimatologie: eine Einführung ; mit 56 Tabellen*. Springer, Berlin, 4., aktualisierte und erw. aufl edition, 2002. ISBN 978-3-540-42919-7. OCLC: 248746654.

A. Matzarakis. Die thermische Komponente des Stadtklimas. Technical Report 6, Universität Freiburg, Freiburg, July 2001. URL https://portal.uni-freiburg.de/meteo/forschung/publikationen/berichte/report6.pdf.

A. Matzarakis, F. Rutz, and H. Mayer. Modelling radiation fluxes in simple and complex environments—application of the RayMan model. *International Journal of Biometeorology*, 51(4):323–334, Mar. 2007. ISSN 0020-7128, 1432-1254. doi: 10.1007/s00484-006-0061-8. URL https://link.springer.com/article/10.1007/s00484-006-0061-8.

E. Maxwell, T. Stoffel, and R. Bird. Measuring and Modeling Solar Irradiance on Vertical Surfaces. Technical Report SERI/TR-215-2525, Solar Energy Research Institute, July 1986.

A. Mohajerani, J. Bakaric, and T. Jeffrey-Bailey. The urban heat island effect, its causes, and mitigation, with reference to the thermal properties of asphalt concrete. *Journal of Environmental Management*, 197: 522–538, July 2017. ISSN 0301-4797. doi: 10.1016/j.jenvman.2017.03.095. URL http://www.sciencedirect.com/science/article/pii/S0301479717303201.

F. J. W. Osseweijer, L. B. P. van den Hurk, E. J. H. M. Teunissen, and W. G. J. H. M. van Sark. A comparative review of building integrated photovoltaics ecosystems in selected European countries. *Renewable and Sustainable Energy Reviews*, 90:1027–1040, July 2018. ISSN 1364-0321. doi: 10.1016/j.rser.2018.03.001. URL http://www.sciencedirect.com/science/article/pii/S1364032118300716.

Y. Qin. Urban canyon albedo and its implication on the use of reflective cool pavements. *Energy and Buildings*, 96:86–94, June 2015. ISSN 0378-7788. doi: 10.1016/j.enbuild.2015.03.005.

V. Quaschning. *Volker Quaschning: Regenerative Energiesysteme*. Hanser Verlag, 7 edition, 2011. ISBN 978-3-446-42732-7. URL `https://www.volker-quaschning.de/publis/regen/index.php`.

S. Ransome, J. Sutterlueti, and S. Sellner. PV technology differences and discrepancies in modelling between simulation programs and measurements. In *2012 38th IEEE Photovoltaic Specialists Conference (PVSC)*, pages 3061–3066, June 2012. doi: 10.1109/PVSC.2012.6318228.

P. Redweik, C. Catita, and M. Brito. Solar energy potential on roofs and facades in an urban landscape. *Solar Energy*, 97:332–341, Nov. 2013. ISSN 0038-092X. doi: 10.1016/j.solener.2013.08.036.

M. Revesz, S. Oswald, H. Trimmel, A. Schneider, P. Weihs, S. Zamini, M. Peyerl, and S. Krispel. PVOPTI-Ray: Optimisation of Reflecting Materials and Photovoltaic Yield in an Urban Context. In *Proceedings of 33rd European Photovoltaic Solar Energy Conference and Exhibition*, pages 2130–2134, Amsterdam, Sept. 2017. ISBN 3-936338-47-7. doi: 10.4229/EUPVSEC20172017-6DO.11.4. URL `http://www.eupvsec-proceedings.com/proceedings?paper=40833`.

M. Revesz, S. M. Oswald, H. Trimmel, P. Weihs, and S. Zamini. Potential increase of solar irradiation and its influence on PV facades inside an urban canyon by increasing the ground-albedo. *Solar Energy*, 174:7–15, Nov. 2018. ISSN 0038-092X. doi: 10.1016/j.solener.2018.08.037.

M. Revesz, S. Zamini, S. M. Oswald, H. Trimmel, and P. Weihs. SEBEpv – New digital surface model based method for estimating the ground reflected irradiance in an urban environment. *Solar Energy*, 199:400–410, Mar. 2020. ISSN 0038-092X. doi: 10.1016/j.solener.2020.01.075. URL `http://www.sciencedirect.com/science/article/pii/S0038092X20300827`.

D. Robinson and A. Stone. Solar radiation modelling in the urban context. *Solar Energy*, 77(3):295–309, Sept. 2004. ISSN 0038-092X. doi: 10.1016/j.solener.2004.05.010.

Sa PVsyst. PVsyst 5.21 Contextual Help, 2012. URL `http://files.pvsyst.com/pvsyst5.pdf`. accessed on 2015-07-29.

M. Santamouris. Cooling the cities – A review of reflective and green roof mitigation technologies to fight heat island and improve comfort in urban environments. *Solar Energy*, 103:682–703, May 2014. ISSN 0038-092X. doi: 10.1016/j.solener.2012.07.003. URL `http://www.sciencedirect.com/science/article/pii/S0038092X12002447`.

S. Sellner, J. Sutterlueti, L. Schreier, and S. Ransome. Advanced PV module performance characterization and validation using the novel Loss Factors Model. In *2012 38th IEEE Photovoltaic Specialists Conference (PVSC)*, pages 002938–002943, June 2012. doi: 10.1109/PVSC.2012.6318201.

H. Taha. Urban climates and heat islands: albedo, evapotranspiration, and anthropogenic heat. *Energy and Buildings*, 25(2):99–103, Jan. 1997. ISSN 0378-7788. doi: 10.1016/S0378-7788(96)00999-1.

M. Šúri, T. A. Huld, and E. D. Dunlop. PV-GIS: a web-based solar radiation database for the calculation of PV potential in Europe. *International Journal of Sustainable Energy*, 24(2):55–67, June 2005. ISSN 1478-6451. doi: 10.1080/14786450512331329556.

P. Weihs, S. Zamini, S. Krispel, S. Oswald, M. Peyerl, M. Revesz, A. Schneider, and H. Trimmel. Optimierung reflektierender Materialien und Photovoltaik im Stadtraum bezüglich Strahlungsbilanz und Bioklimatik. Technical Report 18/2018, Bundesministerium für Verkehr, Innovation und Technologie, Wien, 2018. URL `https://nachhaltigwirtschaften.at/de/sdz/publikationen/schriftenreihe-2018-18-pvoptiray.php#biblio`.

A Appendix

Copies of contributions not directly related to this PhD, as listed in section 6.

A.1 Other Contribution: I

S. M. Oswald, M. Revesz, H. Trimmel, P. Weihs, S. Zamini, A. Schneider, M. Peyerl, S. Krispel, H. E. Rieder, E. Mursch-Radlgruber, and F. Lindberg:

Coupling of urban energy balance model with 3–D radiation model to derive human thermal (dis)comfort. *Int J Biometeorol.* 2019. 63(6):711–722. doi:10.1007/s00484-018-1642-z

International Journal of Biometeorology (2019) 63:711–722
https://doi.org/10.1007/s00484-018-1642-z

ORIGINAL PAPER

Coupling of urban energy balance model with 3-D radiation model to derive human thermal (dis)comfort

Sandro M. Oswald[1] · **Michael Revesz**[2] · **Heidelinde Trimmel**[1] · **Philipp Weihs**[1] · **Shokufeh Zamini**[2] · **Astrid Schneider**[2] · **Martin Peyerl**[3] · **Stefan Krispel**[3] · **Harald E. Rieder**[4] · **Erich Mursch-Radlgruber**[1] · **Fredrik Lindberg**[5]

Received: 11 May 2018 / Revised: 24 September 2018 / Accepted: 28 October 2018 / Published online: 5 December 2018

Abstract

While capabilities in urban climate modeling have substantially increased in recent decades, the interdependency of changes in environmental surface properties and human (dis)comfort have only recently received attention. The open-source solar long-wave environmental irradiance geometry (SOLWEIG) model is one of the state-of-the-art models frequently used for urban (micro-)climatic studies. Here, we present updated calculation schemes for SOLWEIG allowing the improved prediction of surface temperatures (wall and ground). We illustrate that parameterizations based on measurements of global radiation on a south-facing vertical plane obtain better results compared to those based on solar elevation. Due to the limited number of ground surface temperature parameterizations in SOLWEIG, we implement the two-layer force-restore method for calculating ground temperature for various soil conditions. To characterize changes in urban canyon air temperature (T_{can}), we couple the calculation method as used in the Town Energy Balance (TEB) model. Comparison of model results and observations (obtained during field campaigns) indicates a good agreement between modeled and measured T_{can}, with an explained variance of $R^2 = 0.99$. Finally, we implement an energy balance model for vertically mounted PV modules to contrast different urban surface properties. Specifically, we consider (i) an environment comprising dark asphalt and a glass facade and (ii) an environment comprising bright concrete and a PV facade. The model results show a substantially decreased T_{can} (by up to − 1.65 °C) for the latter case, indicating the potential of partially reducing/mitigating urban heat island effects.

Keywords SOLWEIG · PV energy balance · Surface temperature parameterization · UTCI

Electronic supplementary material The online version of this article (https://doi.org/10.1007/s00484-018-1642-z) contains supplementary material, which is available to authorized users.

✉ Sandro M. Oswald
sandro.oswald@boku.ac.at

[1] Institute of Meteorology, University of Natural Resources and Life Sciences (BOKU), Vienna, Austria

[2] AIT Austrian Institute of Technology GmbH, Vienna, Austria

[3] Smart Minerals GmbH, Vienna, Austria

[4] Wegener Center for Climate and Global Change and IGAM/Institute of Physics, University of Graz, Graz, Austria

[5] Department of Earth Sciences, University of Gothenburg, Gothenburg, Sweden

Introduction

Today about half of the world's population resides in urban areas. Future projections show pronounced urbanization rates and it is expected that by 2050, about two thirds of the world's population will be urban (UN 2014). Several studies report on increased thermal heat stress in urban microclimates, e.g., Grimmond et al. (2010). In order to adapt to climate change, some countries aim to reduce solar absorption in urban environments by maximizing the area of highly reflective surfaces through installation of the so-called white roofs. Also, at a time where sustainable energy production becomes more and more important, "solar cities" aim on maximizing "solar harvest", i.e., the solar yield from photovoltaic (PV) modules, by directing their roofs and facades towards the sun to avoiding shadowing. Reflections from the ground and surrounding buildings cause an increase of the solar radiation directed to the PV module, thus increased PV yield (Kotak et al. 2015; Lindberg et al. 2015). The role of PV modules in a city or as a facade in an urban canyon was discussed in the work of Brito et al. (2017). This study has shown that for specific study areas, the non-baseload electricity demand can be satisfied by cost-effective PV investments on roofs and facades at today's market conditions for up to 10 months of the year. Further, winter mid-day electricity demand can only be achieved if the solar yield of PV facades is taken into account.

In terms of human thermal stress, this increase in reflection can cause more discomfort. Human (dis)comfort is commonly described by various bioclimatic indices. The Universal Thermal Climate Index (UTCI) (Fiala et al. 2001; Bröde et al. 2011; Blazejczyk et al. 2011) aggregates many of these in one standardized metric. The UTCI is based on complex multi-node thermophysiological models and allows to predict whole body thermal effects (e.g., hypothermia and hyperthermia; heat and cold discomfort) as well as localized effects (e.g., frostbite). Thereby, UTCI allows addressing all kinds of thermal stress and discomfort (e.g., extreme cold or warm) as well as conditions in which the human heat balance and the perceived outdoor temperature are affected by solar radiation. The accuracy of UTCI depends on a suite of input parameters; among these, especially a precise calculation of the mean radiant temperature T_{mrt} is of uttermost importance (Weihs et al. 2011).

To provide T_{mrt} with highest accuracy, we employ here an updated version (see below) of the open-source solar long-wave environmental irradiance geometry (SOLWEIG) model which is a part of the urban multi-scale environmental predictor (UMEP) (Lindberg et al. 2018). SOLWEIG is a state-of-the-art model which combines building and vegetation surface models and spatial variations of 3-D radiative fluxes in complex urban settings. SOLWEIG has been extensively evaluated in urban environments over the last decade (Lindberg et al. 2008; Lindberg and Grimmond 2011; Lindberg et al. 2016).

In its present configuration (Lindberg and Grimmond 2016), SOLWEIG uses only observed ambient air temperature, independent of its measurement height, to estimate the temperatures of surrounding surfaces (i.e., wall and ground temperature) via a simple parameterization scheme. Moreover, according to the authors' knowledge, to date, no evaluation and simulation tools are available for urban areas, which can estimate the effects of a broad rollout of photovoltaic facade and different ground surfaces in urban districts necessary to characterize the change of ambient air temperature and in general microclimate in urban street canyons.

This study aims on closing this gap by coupling SOLWEIG with parts of the Town Energy Balance (TEB) model (Masson 2000). Below, we detail the model setup as well as results from a recent field campaign for model evaluation. During this field campaign, measurements of short-wave radiation, wind speed, air, and surface temperatures were performed. The campaign took place between August 2016 and September 2017 on the campus of the University of Natural Resources and Life Sciences (BOKU) in Vienna.

The study focuses on (i) the simulation of canyon air temperature based on measured input parameters and its comparison to observed canyon air temperature in the study domain (see dashed yellow box in Figure S1 in the supplemental material); and (ii) evaluating the impact of potential changes in the surface structure parameters of wall and ground (i.e., albedo and energy balance of the PV module) on the canyon air temperature and human comfort.

Methods

Based on the standard meteorological input file of SOLWEIG, we developed a model structure which uses only the required and available variables (ambient air temperature T_a, wind speed U, relative humidity RH, barometric pressure p_a, and incoming short-wave global radiation G_h on a horizontal plane).

Instrumentations

For model development and evaluation, measurements which are routinely performed at the meteorological monitoring platform located at the rooftop of the Schwackhöfer-Haus (at approximately 26-m height above ground) have been used. Additional measurements have been performed within a street canyon nearby (southward-orientated at 3 m above ground). Figure 1a and b shows both platforms and the related measurements; Figure S1 in the supplemental material shows the measurement sites from the top (dark green ellipse = rooftop, green point = canyon). During the campaign, radiation measurements were performed with two types of pyranometer: on the rooftop with a MS-802 global radiation pyranometer (EKO Instruments) with a wavelength range of 285–3000 nm; in the urban canyon with a vertically mounted EMS 11 silicone diode sensor (EMS Brno) covering a wavelength range of 400–1100 nm. The ambient air temperature and relative humidity at the rooftop have been measured with a thermocouple type K combined with a humidity sensor (inside a radiation shield) in direct vicinity to the wind sensor (for speed and direction) on the rooftop (see Fig. 1a). Air temperature and wind speed measurements in the canyon were performed with a

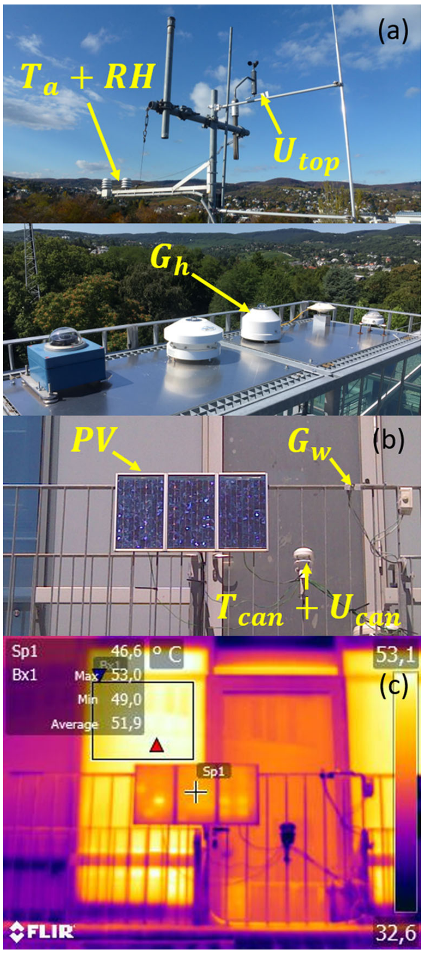

Fig. 1 Measurement setup used in this study. **a** The observational platform of the University of Natural Resources and Life Sciences (BOKU), located at the rooftop of the Schwackhöfer-Haus. **b** Additional instrumentation in the studied urban canyon. **c** Infrared picture of the setup shown in **b** taken on 19 June 2017 at 11:12 UTC. The acronyms in **a** and **b** indicate individual meteorological variables obtained; arrows point towards the corresponding instrument/sensor. These are ambient air temperature T_a and relative humidity RH; both measured with a thermocouple located 26 m above ground; wind speed U_{top} at the rooftop, measured with a Kroneis anemometer 27 m above ground; horizontal global radiation G_h, obtained with a MS-802 pyranometer (EKO Instruments); global radiation on a south-oriented vertical plane G_w in the urban canyon, obtained with an EMS 11 global radiation silicone diode sensor (EMS Brno); canyon air temperature T_{can} and canyon wind speed U_{can}, both obtained with a DS-2 sonic anemometer (METER Group, Inc). The three photovoltaic modules *PV* are of type SX10M (SOLAREX). In the upper left of panel **c**, surface temperatures of the PV modules (Sp1) and the building facade of the Schwackhöfer-Haus (Bx1) are given

DS-2 sonic anemometer (METER Group, Inc.) with a speed range of 0–30 m s^{-1} and an accuracy of 0.3 m s^{-1} (see Fig. 1b). The measurement outputs of the individual sensors in the urban canyon have been aggregated to 10-min averages to match the temporal resolution of the routine rooftop measurements.

The surface temperatures were additionally measured with an infrared camera of type FLIR E60bx (FLIR Systems), which has an accuracy of $\pm$ 2% between 0 and 650 °C (see Fig. 1c).

The potential electricity production inside the urban canyon was determined with three PV modules of type SX10m (SOLAREX). The surface temperature was measured with three thermocouples on the back side of the PV modules.

Parameterization of wall surface temperature

Bogren et al. (2000) proposes to estimate the surface temperatures T_s (horizontal or vertical) via a linear relationship between maximum solar elevation and the maximum difference between measured T_a and T_s under clear-sky conditions (Lindberg et al. 2008). Here, we propose a different approach, using global radiation measured on a south-oriented vertical plane G_w instead of solar elevation. G_w is calculated as

$$G_w = G_h \frac{sin(\alpha + \beta)}{sin(\alpha)} \tag{1}$$

where β is the tilt angle of the vertical plane measured from the horizontal and α is a function of the geographical latitude ϕ and the declination angle δ given by

$$\begin{aligned}\delta =\ & (180/\pi) \cdot (0.006918 - 0.399912 \cdot cos(B) \\ & + 0.070257 \cdot sin(B) - 0.006758 \cdot cos(2B) \\ & + 0.000907 \cdot sin(2B) - 0.002697 \cdot cos(3B) \\ & + 0.00148 \cdot sin(3B)), \qquad (2)\\ \alpha =\ & 90 - \phi - \delta \qquad (3)\end{aligned}$$

where $B = (n-1)\frac{360}{365}$ with the nth day of the year (Spencer 1971; PVEducation 2017).

To obtain the wall surface temperature T_w, we apply the amplitude from the before mentioned linear relationship to a sinusoidal wave function with maximum temperature difference at 15:00 (local time) (Lindberg et al. 2016).

Parameterization of ground surface temperature

To calculate the ground temperature T_g, we apply the force-restore method following Blackadar (1976) with a two-layer approximation, i.e., with a parameterization of the sensible heat flux H_s (2nd term in Eq. 4) and the ground heat flux

H_g (3rd term in Eq. 4). The change in T_g per time step is given as:

$$\frac{\partial T_g}{\partial t} = \frac{F}{S\,z_g} - a_{FR}\left(T_g - T_{as}\right) - \Omega\left(T_g - T_m\right) \quad (4)$$

Here, F represents the net radiation balance at the ground surface (which can be directly calculated with SOLWEIG), S is the soil heat capacity given as a product of a materials density ρ and its specific heat capacity c, Ω is the angle velocity of the Earth, and a_{FR} which is a time-of-day dependent factor (3×10^{-4} s^{-1} for daytime, 1×10^{-4} s^{-1} for nighttime). T_m is the approximately constant temperature of the bottom slab. The depth of the thermal active layer z_g is calculated using time period τ and thermal conductivity λ (Stull 1988):

$$z_g = \sqrt{\frac{\tau\,\lambda}{4\,\pi\,S}} \quad (5)$$

It follows that the near-surface air temperature T_{as} has to be simulated based on measurements of T_a on the rooftop. To model such continuous time series of T_g at time step $(t+1)$, we apply the Euler method with a given T_g at time step (t) and the rate of change from Eq. 4 times a value i for the size of every step:

$$T_g(t+1) = T_g(t) + \frac{\partial T_g}{\partial t} \cdot i \quad (6)$$

Parameterization of urban canyon air temperature

As detailed above, we are interested in the air temperature near the ground surface T_{as}. For simplification, we set T_{as} as $\widehat{T}_{can}$ which is calculated in analogy to the TEB model.

$$\widehat{T}_{can} = \frac{\frac{T_g}{RES_g} + \frac{2h}{w}\frac{T_w}{RES_w} + \frac{T_a}{RES_{top}}}{\frac{1}{RES_g} + \frac{2h}{w}\frac{1}{RES_w} + \frac{1}{RES_{top}}} \quad (7)$$

Note we did not parameterize the anthropogenic sensible heat flux and snow cover terms given the general lack of traffic at the case study site and summer time conditions. Further required terms for estimating $\widehat{T}_{can}$ are $\frac{h}{w}$, the canyon aspect ratio (building height h to street width w) and RES, the aerodynamic resistance for the ground (RES_g), wall (RES_w), and rooftop (RES_{top}), respectively, given as:

$$RES_g = RES_w = \frac{c_p\,\rho_a}{\left(11.8 + 4.2\sqrt{U_{can}^2 + (u_* + w_*)^2}\right)} \quad (8)$$

$$RES_{top} = \left(U_{top}\,C_d\right)^{-1} \quad (9)$$

whereby U_{can} (parameterized as in the TEB model) and U_{top} (measured) are the wind speeds for canyon and rooftop, respectively. The characteristic scale of turbulent wind $u_* + w_*$ is calculated using T_a, U_{top}, and the drag coefficient C_d (computed with the roughness length $z0_{town} = \frac{h}{10}$ and $\widehat{T}_{can}$ of the previous time step) (Moigne 2012). For estimating the surface heat flux, we consider the rate of warming $\left(\frac{\partial T_a}{\partial t}\right)_r$ at the rooftop as representative for the whole convective boundary layer:

$$u_* + w_* = \sqrt{C_d}\,U_{top} + \left[\frac{g\,h^2}{T_a}\left(\frac{\partial T_a}{\partial t}\right)_r\right]^{1/3} \quad (10)$$

where g is the gravitational constant (Arya 2001).

Energy balance model for PV modules

Following the concept of the heat dynamics model for building-integrated photovoltaic (BIPV) systems of Lodi et al. (2012), we introduce a modified energy balance model for PV module(s) mounted in urban canyons. As model input, we use besides global radiation information (see above) the measured surface temperature on the back side of the PV module $T_{b_{PV}}$, and information from a 2-D sonic anemometer. At our study site, the thermal radiative heat transfer between the back side of the PV module and the gray glass facade of the Schwackhöfer-Haus (see Fig. 1b) behind can be calculated following:

$$Ql_b = \frac{A_{PV}\,\sigma}{\frac{1}{\varepsilon_{b_{PV}}} + \frac{1}{\varepsilon_w} - 1}\left(T_{b_{PV}}^4 - T_w^4\right) \quad (11)$$

where A_{PV} represents the area of the photovoltaic module with a value of 0.11 m^2. $\varepsilon_{b_{PV}}$ and ε_w are the emissivity for the back side of PV modules and the facade of the Schwackhöfer-Haus, respectively. T_{PV}, the front temperature of the PV module (which might be higher than $T_{b_{PV}}$), can be calculated following:

$$T_{PV} = T_{b_{PV}} + \frac{G_w}{1000\ \mathrm{W\ m^{-2}}}\,\Delta T \quad (12)$$

where ΔT is the temperature difference between the front and back sides of the PV module. ΔT is set to 1.9 °C at an irradiance level of 1000 W m^{-2} (King et al. 2004).

Now, the long-wave radiation exchange Ql_f between the sky, ground, the opposite building (Exner-Haus, see Figure S1 in the supplemental material), and the front side of the PV module is given as:

$$\begin{aligned} Ql_f = {} & A_{PV}\,\sigma\,\Big(\Psi_{sky}\,\varepsilon_c\,T_{sky}^4 + \Psi_g\,\varepsilon_c\,T_g^4 \\ & + \Psi_b\,\varepsilon_c\,T_b^4 - \varepsilon_{gl}\,T_{PV}^4\Big) \end{aligned} \quad (13)$$

The parameter Ψ is the view factor for surrounding surfaces. Figure S2 in the supplemental material shows a fisheye lens picture of the PV module perspective combined with three digitalized images for the sky, for the ground, and for buildings. The respective area percentage calculation yields a sky view factor of $\Psi_{sky} = 0.23$, ground view factor $\Psi_g = 0.43$, and a building's view factor of $\Psi_b = 0.35$. For the emissivity ε_c, we assume a combined value of 0.95. Due to the available information of dew point temperature T_{dew} on the rooftop, the sky temperature T_{sky} can be calculated using the method of Duffie and Beckman (2013). The temperature of the Exner-Haus T_b, which is shaded throughout the day, is set to T_a (Lindberg and Grimmond 2011).

To determine the convective heat transfer Qc between the front (Eq. 14) and back sides (Eq. 15) of the PV module and the surrounding air, we apply Newton's law of cooling following Palyvos (2008) and Sharples (1984):

$$Qc_f = A_{PV}\,(7.35 + 3.75 \cdot U_{can})\,(T_{can} - T_{PV}), \tag{14}$$

$$Qc_b = A_{PV}\,(1.8 + 1.93 \cdot U_{can})\,(T_{can} - T_{b_{PV}}) \tag{15}$$

The absorbed solar radiation is estimated through the transmittance-absorptance product $(\tau\alpha)_{PV} \cong 1.01\,\tau_{gl}\,\alpha_{PV}$ (Duffie and Beckman 2013) and the incidence angle modifier $\mathrm{IAM}(\theta_{aoi})$ (Barker and Norton 2003):

$$Q_s = A_{PV}\,1.01\,\tau_{gl}\,\alpha_{PV}\,G_w\,\mathrm{IAM}(\theta_{aoi}) \tag{16}$$

The remaining term of the heat transfer process is transformed solar energy (i.e., electricity production of the PV module), which is given as a function of T_{PV}:

$$Q_e = A_{PV}\,G_w\,\mathrm{IAM}(\theta_{aoi})\,\eta_{ref}\,\left[1 - \beta_0\left(T_{PV} - T_{PV,ref}\right)\right] \tag{17}$$

where η_{ref} is the reference PV module efficiency (determined by laboratory measurements), β_0 is a temperature coefficient (see Table 1), and $T_{PV,ref} = 25\ ^\circ\mathrm{C}$ is the reference temperature at 1000 W m^{-2} (manufacturer provided).

Continuous Time Stochastic Modeling for unknown parameters

Continuous Time Stochastic Modeling (CTSM) is widely used to estimate unknown parameters of non-linear systems (Jazwinski 1970; Nielsen et al. 2000). Following the scheme of a gray box model, which combines prior physical knowledge and information from measurements, one can use a set of stochastic differential equations (SDEs) of form

$$dX_t = f(X_t, U_t, t, \Theta)\,dt + W(X_t, U_t, \Theta)\,d\omega_t \tag{18}$$

and a set of discrete time observation equations of form

$$y_k = M(X_k, U_k, t_k, \Theta) + e_k \tag{19}$$

where t is the time, X_t is a vector of state variables, U_t is a vector of input variables, Θ is a vector of unknown parameters, and y_k is a vector of output variables. $f(\cdot)$, $W(\cdot)$, and $H(\cdot)$ are non-linear functions, ω_t is a Wiener process, and e_k is the Gaussian white noise with the covariance $\sum_t$. The CTSM package in R (Juhl 2016) applies a maximum likelihood estimation of a time series with joint probability density function

$$L(\Theta) = \left(\prod_{k=1}^{N} p(y_k \mid \Upsilon_{k-1}, \Theta)\right) p(y_0 \mid \Theta) \tag{20}$$

with $\Upsilon_N = [y_0, y_1, ..., y_k, ..., y_N]$ as a time series of N observations. CTSM-R computes the likelihood function and uses an optimization method to locate the most probable set of parameters (Juhl et al. 2016).

Given the relatively small area of the PV module used in this study (compared to, e.g., modules used in Jones and Underwood (2001) and Lodi et al. (2012)), we considered a single-state model to predict the average cell temperature. In our case, the unknown parameters are the absorptivity of the cells inside PV modules α_{PV} and the heat capacity C_{PV}. The non-linear system for the photovoltaic energy balance model to estimate these parameters is given as:

$$\begin{aligned} dT_{PV} &= C_{PV}^{-1}\,\big(Qc_f + Qc_b + Ql_f \\ &\quad + Ql_b + Q_s - Q_e\big)\,dt + W\,d\omega_t, \\ T_{PV,m} &= T_{PV} + e_k \end{aligned} \tag{21}$$

Once the unknown parameters are determined, the Euler method from Eq. 6 can be used to calculate the estimated PV module temperature $\widehat{T}_{PV}(i)$ based on knowledge of global radiation (on a vertical plane), wind speed, and ambient air temperature at the rooftop, the angle of incidence of the current step (i), and the back-side PV module temperature with the canyon air temperature from the previous time step $(i-1)$.

Results

Model evaluation for wall, ground, and air temperature

As shown in Lindberg et al. (2016), the surface temperature parameterization in SOLWEIG affects the mean radiant temperature. Thus, precise measurements of the temperature of surrounding surfaces are needed to accurately simulate the canyon air temperature.

To this aim, infrared measurements (with a FLIR E60bx) were taken of the facade behind the PV modules around the time of maximum solar elevation. Due to the possible settings in FLIR Tools (FLIR Systems 2016), the position where pictures were taken was 5 m in front looking normal to the wall of the Schwackhöfer-Haus and the emissivity was set to $\varepsilon_w = 0.95$.

Following Lindberg et al. (2016), we show in Fig. 2a the difference in wall surface temperature T_w and air (in our case canyon) temperature T_{can}, as a function of the maximum solar elevation. The regression coefficients found

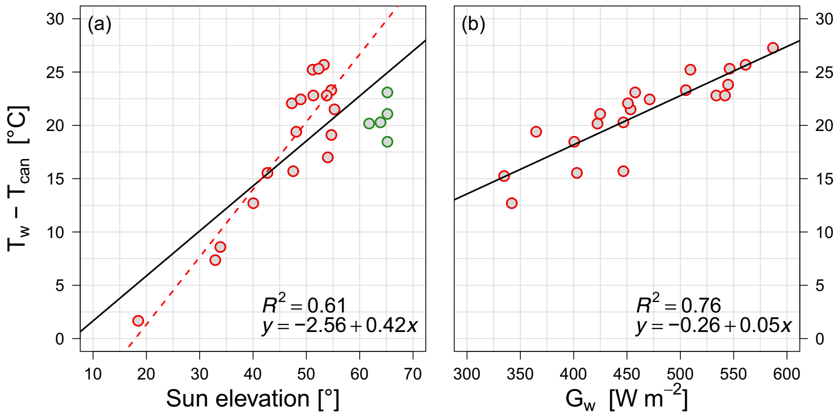

Fig. 2 Scatter plots of the difference in temperature between the wall surface temperature (T_w) and canyon air temperature (T_{can}) as a function of **a** the solar elevation and **b** global radiation on a south-facing vertical wall (G_w). The green points in panel **a** mark the outliers from the theoretical curve (dashed red line) describing higher surface temperature at higher solar elevation. The squared Pearson correlation coefficient (R^2) and the regression analysis with the coefficients are provided in each panel. Note the number of measurements in **a** and **b** are not the same as global radiation measurements have not been available on 2 days

in the present analysis are in close agreement with those originally described by Lindberg et al. (2016). Despite a general agreement, a few individual measurements (marked in green) deviate from the theoretical curve (dashed red line) describing higher surface temperature at higher solar elevation. However, the study of Lindberg et al. (2016) considered only temperatures at solar elevation below 56 ° due to the higher geographic latitude in Sweden compared to Vienna. Figure 2b shows a new method regarding the difference of T_w and T_{can} as a function of the observed values G_w. The explained variance of the temperature difference is strongly improved using G_w as predictor (compare $R^2 = 0.61$ in panel (a) with $R^2 = 0.76$ in panel (b)).

Calculating the ground temperature with the force-restore method, we apply the following quantities: the heat capacity of asphalt given as $S_{asphalt} = 920$ J kg^{-1} K^{-1} $\cdot$ 2120 kg m^{-3} = 1.95 × 10^6 J m^{-3} K^{-1} and the thermal conductivity $\lambda_{asphalt} = 0.7$ W m^{-1} K^{-1} (Lumitos 2017). T_m was set as an average of the daily mean of T_a and the annual average temperature in 2 m depth of 12 °C to account for seasonal ground temperature variations (possible maximum temperature was measured in 2-m depth of 18.6 °C) (ZAMG 2018). To obtain F in Eq. 4 with highest accuracy in SOLWEIG, measurements of the albedo of the Schwackhöfer-Haus (gray panels faced with glass in the upper part of Figure S3 in the supplemental material) yielded a value of 0.27.

The canyon aspect ratio was calculated taking the average height of both buildings and a street width of 17 m which yields a value of $\frac{h}{w} = \frac{20.2\text{ m}}{17\text{ m}} \simeq 1.19$. As now all required parameters for the calculation of the canyon air temperature $\widehat{T}_{can}$ are available, we derive it following Eq. 7.

Figure 3 provides a time series of the measured and simulated air temperature inside and above the urban canyon. We show the estimates for $\widehat{T}_{can}$ for both the currently implemented SOLWEIG scheme (CS) and the here proposed calculation scheme (PS). While both, CS and PS agree quite well with the measurements of T_{can}, a closer comparison reveals structural differences among the two approaches. Estimates from CS agree closer with observations during morning hours (before 10:00 UTC), while estimates from PS are closer to the measured canyon air temperature around noon and during the afternoon/early evening (until about 19:00 UTC). A disadvantage of CS compared to PS is the circumstance that the ground temperature decreases immediately to T_a due to the shadow matrix. This is clearly visible in Figure S4 (supplemental material) where at around 14:00 UTC, $T_{asphalt}$ (CS) rapidly decreases due to shading of the canyon (by the bridge marked with yellow lines in Figure S1). The two outliers in CS between 18:00 and 20:00 UTC stem from the fractional cloud cover function as described in Lindberg et al. (2008). Due to application of the parameterization throughout the night, the simulated air temperatures are too low, especially at the end of the time series after a pronounced heat wave.

The statistical analysis of the modeled versus observed canyon air temperature for CS and PS is shown in Fig. 4a and b, respectively. While both parameterization schemes work generally well, PS shows an improved explained variance (squared Spearman's rank correlation coefficient) compared to CS. More importantly though, the root mean

Fig. 3 Time series of the air temperature (T) measured at the rooftop (T_a, red) and inside the urban canyon (T_{can}, green), and simulated canyon air temperature with the currently implemented SOLWEIG scheme (CS) ($\widehat{T}_{can}$, orange, dashed line) and the proposed calculation scheme (PS) ($\widehat{T}_{can}$, orange, solid line). Time series of the difference between T_{can} and $\widehat{T}_{can}$, respectively, is shown in the lower part (brown dashed (CS) and solid (PS) lines)

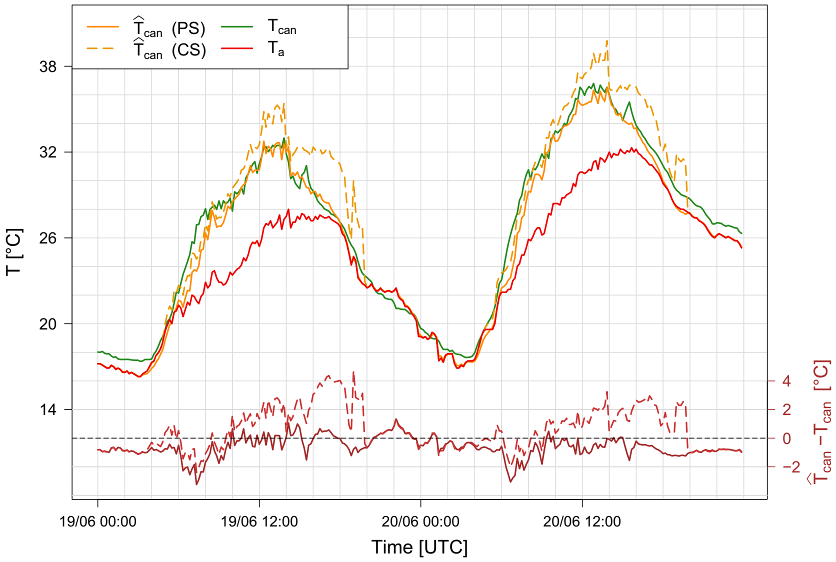

square error (RMSE) for PS is reduced compared to CS. In summary, the here-presented calculation scheme (PS) performs better than the standard scheme (CS). Nevertheless, also PS shows slight underestimations in the heating phase of the urban canyon.

Parameter estimation and simulation for PV modules

As manufacturers commonly do not provide optical or thermal specifications of a PV module, this information was compiled through literature review (see Table 1). The initial value of C_{PV} for the CTSM system was estimated using a value given in Jones and Underwood (2001) with a total heat capacity of 2918 J K^{-1} and a total area of 0.51 m^2. Assuming the mounted PV modules are very similar to the ones in Jones and Underwood (2001), the heat capacity of each module is 2918 J K^{-1} $\cdot$ $\frac{0.11\,\mathrm{m}^2}{0.51\,\mathrm{m}^2}$ $\approx$ 650 J K^{-1} (scaled by total area). The final value of C_{PV} is given in Table 1. α_{PV} was also estimated by CTSM using an initial value of Moralejo-Vàzquez et al. (2015).

Lodi et al. (2012) suggests parameter estimation based on data from partly cloudy days, given that the modeled heat transfer processes are less correlated under cloudy than under clear-sky conditions. For the present study, parameter estimation is based on data taken on 18 June 2017 between

Fig. 4 Scatter plots of measured (T_{can}) and simulated ($\widehat{T}_{can}$) canyon air temperature for **a** the proposed calculation scheme and **b** the currently implemented SOLWEIG scheme. Each panel provides the squared Spearman's rank correlation coefficient (R^2) and the root mean square error (RMSE)

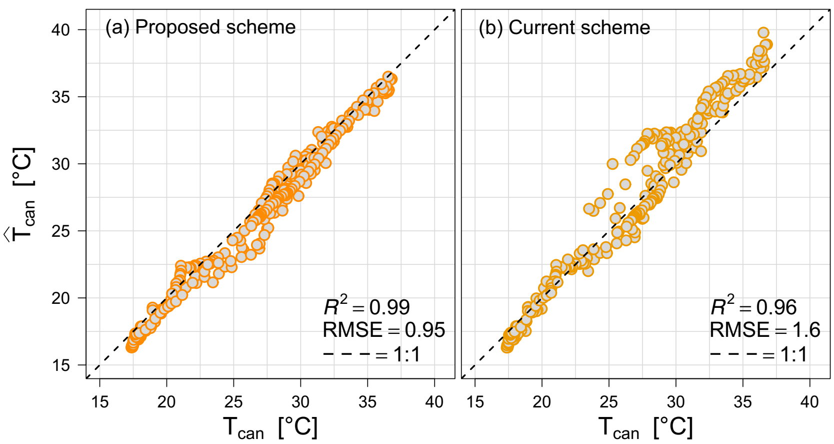

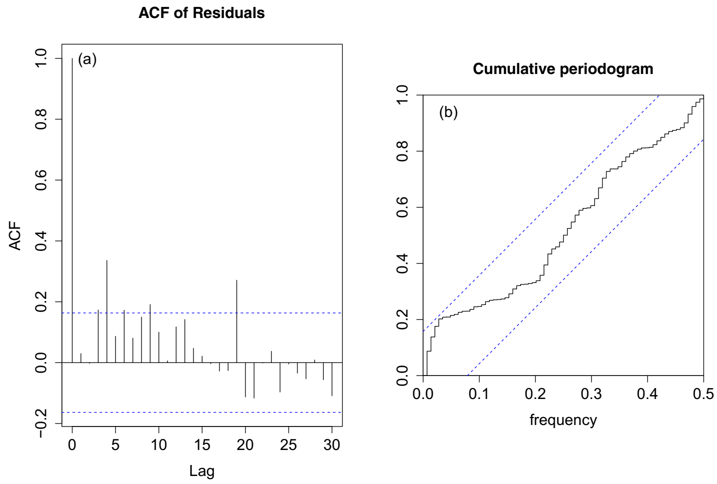

Fig. 5 **a** The auto-correlation function (ACF) and **b** the cumulated periodogram of the residuals for the continuous time stochastic model used for the mounted photovoltaic module. The blue dashed lines mark the 95% confidence limits for random noise

00:00 and 23:50 UTC with 10-min temporal resolution. Measurements include several input values for the CTSM system including G_w, U_{can}, T_a, T_{can}, T_{dew}, and T_{bPV}. Ground temperature T_g in front of the PV module and wall temperature T_w behind the PV module have been simulated with the PS scheme in SOLWEIG. T_g was averaged over an area of $7 \cdot 7$ m^2 (see Figure S1 in the supplemental material, red square), seen as the distance from the PV module to parked cars. In Fig. 5, we show the white noise verification of the model considering the auto-correlation function (ACF, panel (a)) and the cumulative periodogram (panel (b)). Here, the blue dashed lines mark the confidence level of 95% under the hypothesis that the model residuals are white noise. The PS describes heat transfer in and around the PV module enough sufficiently. We note in passing that for characterizing a larger PV unit, the model would need to be expanded to a two-state model as used for example by Lodi et al. (2012).

Applying the estimated parameters (Table 1) in Eq. 21 combined with the Euler method, the PV module temperature is predicted. The output of the simulated $\widehat{T}_{bPV}$ is compared with the measured T_{bPV} for 18 to 20 June 2017 in Fig. 6a. In panel (b), we show the difference between model prediction and observations. The model shows most satisfactory results on June 18, a day with partial cloud cover. In contrast, larger differences are found for 19 and 20 June 2017, which have been characterized by prevailing clear-sky conditions. Clear-sky days are more difficult to model due to overall higher temperatures and reflections of obstacles in the environment (see second sun in Figure S3 in the supplemental material). However, the statistical analysis of the CTSM-based system (provided in Fig. 7) shows good agreement throughout the time series, with an explained variance of $R^2 = 0.99$ and a RMSE = 1.2 °C (N = 432).

Simulations for various surface conditions

Urban planning strives to reduce the urban canyon air temperature and generally undesirable effects of the urban heat island. Therefore, the UTCI can describe human thermal comfort inside different surface structures and is thus an important planning quantity.

This study seeks to model the urban thermal environment at a study site in Vienna, Austria. We compare the influence of the current urban structure at the study site (dark asphalt on the ground combined with a glass facade) with those of a ground of bright concrete combined with a

Table 1 Technical specifications of the three PV modules used in this study

Type of solar cell		Poly-crystalline[1]
Total aperture area	0.11	m^2
Voltage at MPP[2]	16.80	V
Current at MPP[2]	0.59	A
Nominal power	10.00	W
PV module efficiency[3] η_{ref}	8.07	%
Temperature coefficient β_0	0.50	% K^{-1}
Absorptivity of cell α_{PV}	0.84	
Emissivity of glass[4] ε_{gl}	0.91	
Transmittance of glass[5] τ_{gl}	0.90	
Emissivity of back side[4] ε_{bPV}	0.85	
Heat capacity C_{PV}	754.95	J K^{-1}

[1] p-Si
[2] Maximum Power Point
[3] Average of all three PV modules
[4] (Armstrong and Hurley 2010)
[5] (Herrando et al. 2014)

Fig. 6 Time series of **a** the temperature (T) measured inside the urban canyon (T_{can}, green) and at the back side of the PV module ($T_{b_{PV}}$, blue) and simulated at the back side of the PV module ($\widehat{T}_{b_{PV}}$, red) and **b** the difference ($\Delta T_{b_{PV}}$) between the measured and simulated back-side photovoltaic module temperature

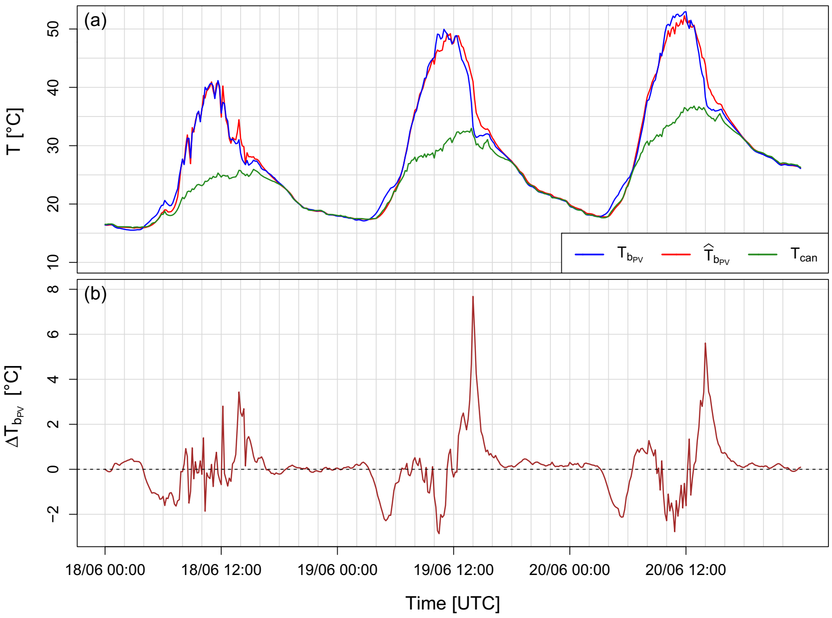

photovoltaic facade. To this aim, we assume conditions where PV modules cover the whole southern wall of the building in the study domain, as the distance between the PV modules and the back-side wall is large enough to assume that the convective heat transfer is the same as used in the CTSM system. The largest uncertainty of this assumption is that we do not have knowledge about the surface temperature of the back-side wall which is an input variable for thermal radiative heat transfer. Therefore, we need to make assumptions for T_w. Here, we assume that it can be calculated with the same regression coefficients as given in Fig. 2b but considering addition of an average value of $\widehat{T}_{can}$, T_a, and daily average of T_a (considering that the daily average will not change its value, only the amplitude varies). Further, we make the assumption that the calculated U_{can} as in the TEB model can be taken as wind speed for calculating the UTCI.

After defining the new modeling systems, a comparison of the canyon air temperature between different surface conditions can be done. For such calculations, the albedo κ of each surface has to be defined. The albedo value for asphalt $\kappa_g = 0.18$ was chosen based on Lindberg et al. (2016). The value for concrete $\kappa_g = 0.56$ was measured in the work of Krispel et al. (2017) and the value for the PV modules $\kappa_{PV} = 0.10$ was taken from Moralejo-Vàzquez et al. (2015).

Figure 8a, b, and c shows time series of $\widehat{T}_{can}$ and the UTCI for these different surface conditions including an additional simulation for UTCI with T_a. The related differences, $\Delta\widehat{T}_{can}$ and ΔUTCI, are shown in Fig. 8d, e, and f, respectively. Our results show that a bright ground surface and a slightly decreased wall temperature (see Figures S4 and S5 in the supplemental material) can substantially reduce air temperature (by up to − 1.30 °C) and the UTCI (by up to − 1.10 °C) in the sun between 7:00 and 14:00

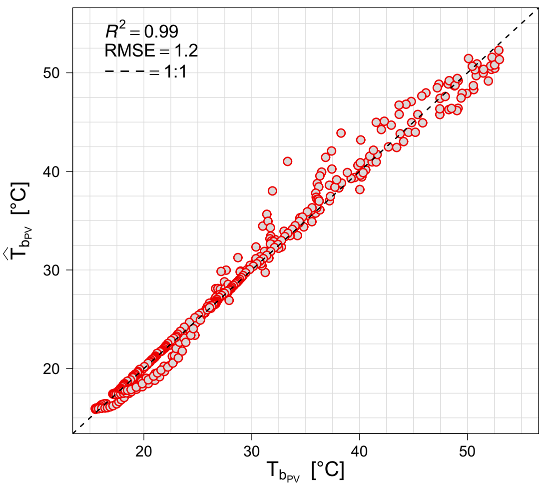

Fig. 7 Scatter plot of the measured temperature ($T_{b_{PV}}$) and simulated temperature ($\widehat{T}_{b_{PV}}$) of the PV module. The upper-left corner provides the squared Spearman's rank correlation coefficient (R^2) and the root mean square error (RMSE)

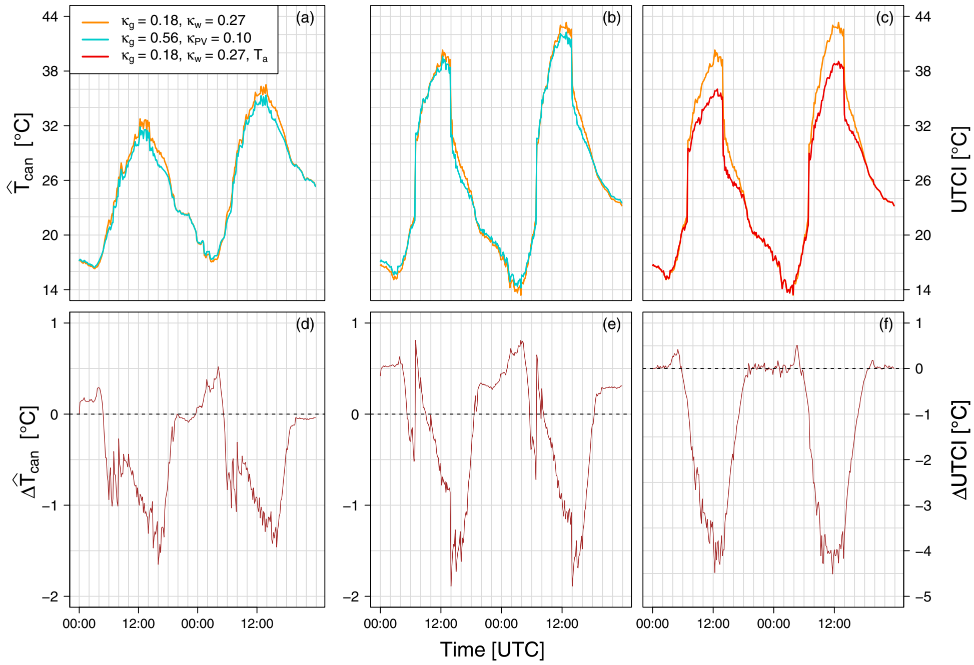

Fig. 8 Time series of **a** the modeled urban canyon air temperature ($\widehat{T}_{can}$), (**b**, **c**) the modeled Universal Thermal Climate Index (UTCI) with $\widehat{T}_{can}$ (orange and cyan), and the air temperature measured at the rooftop T_a (red) between 19 and 20 June 2017. The legend in panel **a** shows the reflectance (κ) for different surfaces ($\kappa_g = 0.18$ for asphalt, $\kappa_w = 0.27$ for glass facade, $\kappa_g = 0.56$ for concrete, and $\kappa_{PV} = 0.10$ for photovoltaic facade). Panels **d**, **e**, and **f** provide the difference between each surface condition regarding $\widehat{T}_{can}$ and UTCI, respectively

UTC. Even larger reductions are found in the shade between 14:00 and 16:00 UTC for both canyon air temperature (by up to − 1.65 °C) and UTCI (by up to − 1.85 °C). Further, Fig. 8f shows that an air temperature measured at a site which is not related to the actual surrounding surfaces results in a highly erroneous estimate of thermal (dis)comfort. In our case, ΔUTCI simulated with T_a shows a difference up to − 4.50 °C and misses the very strong occurring heat stress (defined as UTCI between 38 and 46 °C) on the first day of the simulation period (see Fig. 8c).

These results indicate that even small, local changes to the surface and thus albedo can have a measurable effect on air temperature and UTCI in an urban canyon. While this decrease between − 1 and − 2 °C seems to be noticeable but yet small, it shall not be underestimated in its effect on human comfort in a warmer future climate.

Discussion and conclusions

This study seeks to improve the simulation of air temperature in urban canyons. To this aim, field measurements have been performed in 2016 and 2017, to evaluate/update the wall and ground temperature parameterization and an energy balance model for photovoltaic (PV) modules within the solar and long-wave environmental irradiance geometry (SOLWEIG) model and couple it with parts of the Town Energy Balance (TEB) model.

For the parameterization of the wall surface temperature, we take infrared pictures of the Schwackhöfer-Haus at the University of Natural Resources and Life Sciences (BOKU), Vienna, with a FLIR E60bx to evaluate the accuracy of the current calculation scheme in SOLWEIG. Results show a clear overestimation of the surface temperature at solar elevation angles over 56 ° ($R^2 = 0.61$). We use global radiation measurements on a vertical plane instead to generate new regression coefficients ($R^2 = 0.76$).

We implement an updated calculation scheme for simulating ground temperature, which allows considering surface with user-specified albedo value and thermal conductivity properties. To develop this scheme, we used the force-restore method combining the radiation, sensible, and ground heat flux with the Euler method to estimate a time series of the ground temperature.

At the BOKU site, the ambient air temperature has been measured routine at the rooftop (26-m height above ground) but outputs show a difference up to 6 °C to the measured canyon air temperature (3 m height above ground). This huge difference is compensated with parts of the TEB model calculating the canyon air temperature.

We compare the performance of the currently implemented SOLWEIG scheme (CS) and the here-proposed calculation scheme (PS). The results of the canyon air temperature show a better performance of PS, particularly a substantial reduction in RMSE. While the PS shows generally satisfactory skill in predicting temperatures inside the studied urban canyon, we note that further updates are needed for the representation of open areas, street crossings, and different canyon orientations. Further, an implementation of the glazing ratio for buildings would also increase the overall quality of SOLWEIG.

Considering the importance of sustainable energy production and climate warming, we perform scenario calculations to investigate effects of potential changes to the wall surface inside an urban canyon. We do so by evaluating a heat transfer single-state model for a vertically mounted photovoltaic (PV) module.

A comparison between model results for current surface conditions (dark asphalt on the ground combined with a glass facade) and possible modification conditions (ground covered with bright concrete and a PV facade) was performed. The results indicate a robust decrease in canyon air temperature by up to − 1.65 °C for the modified canyon environment. To estimate human thermal comfort, we focus to calculate the Universal Thermal Climate index (UTCI). UTCI decreases by approx. − 1.00 °C in the sun and − 1.85 °C in the shade considering a change from present to modified conditions. We note in passing that future work should focus on effects of brighter surfaces for potentially increased human thermal stress.

We note in closing that additional field experiments for PV facades or building-integrated PV systems on large scales (e.g., a size of 60 · 20 m^2 like the south-facing wall of the Schwackhöfer-Haus) would strongly increase the quality of energy balance models, as the one presented here, and the possibility to mitigate, at least partially, urban heat island effects.

Acknowledgements Open access funding provided by University of Natural Resources and Life Sciences Vienna (BOKU). The authors thank Meteo France and Valéry Masson for providing the Town Energy Balance model. The authors are grateful to Christian Gützer (University of Natural Resources and Life Sciences (BOKU), Vienna) for the technical support. This work received financial support from the University of Natural Resources and Life Sciences (BOKU) in Vienna.

Funding information This work was supported by the project "Optimizing reflecting materials and photovoltaics in urban areas regarding the radiation balance and bioclimatic" funded by the Austrian Research Promotion Agency (FFG) and the project "Influence of urban expansions on the urban heat island in Vienna" funded by the Klima- und Energiefonds.

Abbreviations a, time-of-day dependent factor (force-restore method) (1/s); A, area (m^2); B, day of the year dependent factor (declination angle) (−); c, specific heat capacity (J/); C, heat capacity (J/K); C_d, drag coefficient (−); CS, currently implemented SOLWEIG scheme; CTSM, continuous time stochastic model; e, Gaussian white noise (−); f, non-linear function; F, net radiation balance (W/m^2); g, gravitational constant (m/s^2); G, global radiation (W/m^2); h, building height (m); $\overline{h}$, average building height (m); H, heat flux (W/m^2); i, value for the size of every step (Euler method) (−); IAM, incidence angle modifier (−); M, non-linear function; n, day of the year (−); N, number of observations (−); p, pressure (hPa); PS, proposed calculation scheme; Q, heat transfer (W/m^2); Qc, convective heat transfer (W/m^2); Ql, long-wave heat transfer (W/m^2); RES, aerodynamic resistance (s/m); RH, relative humidity (%); S, soil heat capacity (J/m^3 K); t, time (s); T, measured temperature (°C); $\hat{T}$, modeled temperature (°C); $u_* + w_*$, turbulent wind (m/s); U, wind speed (m/s); w, street width (m); W, non-linear function; y, discrete time observation; z, depth of thermal layer (m); z_0, roughness length (m).

Greek symbols α, absorptivity (−); β, tilt angle of a vertical plane from the horizontal (°); β_0, temperature coefficient of photovoltaic module (%/K); δ, declination angle (°); ΔT, temperature difference (K); ε, emissivity (−); η, photovoltaic module efficiency (%); θ_{aoi}, angle of incidence (°); Θ, vector of unknown parameters; κ, reflectance (−); λ, thermal conductivity (W/(m K)); ρ, material density (kg/mÂş); σ, Stefan-Boltzmann constant (W/(m^2 K^4)); Σ, covariance; Υ, time series of N observations; ϕ, geographical latitude (°); Ψ, view factor (−); ω, Wiener processs; Ω, Earth's angle velocity (1/s).

Subscripts a, air; as, near-surface air; $asphalt$, index for asphalt properties; b, back side; b_{PV}, back side of photovoltaic module; c, combined value; can, urban canyon; dew, dew point; e, electricity; f, front side; g, ground; gl, glass; h, horizontal plane; m, approximately constant value; p, constant pressure; PV, photovoltaic module; r, rate; ref, reference; s, solar; sky, sky; top, rooftop; w, wall.

References

Armstrong S, Hurley WG (2010) A thermal model for photovoltaic panels under varying atmospheric conditions. Appl Therm Eng 30(11-12):1488–1495

Arya P (ed.) (2001) Introduction to micrometeorology, Academic Press

Barker G, Norton P (2003) Building america system performance test practices: part 1 – photovoltaic systems, technical report, Office of Scientific and Technical Information (OSTI)

Blackadar AmKa (1976) Modeling the nocturnal boundary layer, Reprints third symp. Atmospheric turbulence, diffusion and air quality, Raleigh, Am Meteorol Soc, pp 46–49

Blazejczyk K, Epstein Y, Jendritzky G, Staiger H, Tinz B (2011) Comparison of UTCI to selected thermal indices. Int J Biometeorol 56(3):515–535

Bogren J, Gustavsson T, Karlsson M, Postgard U (2000) The impact of screening on road surface temperature. Meteorlogical Applications 7(2):97–104

Brito MC, Freitas S, Guimarães S, Catita C, Redweik P (2017) The importance of facades for the solar PV potential of a mediterranean city using liDAR data. Renew Energy 111:85–94

Bröde P, Fiala D, Błażejczyk K, Holmér I, Jendritzky G, Kampmann B, Tinz B, Havenith G (2011) Deriving the operational procedure for the universal thermal climate index (utci). Int J Biometeorol 56(3):481–494

Duffie JA, Beckman WA (2013) Solar engineering of thermal processes. Wiley, New York

Fiala D, Lomas KJ, Stohrer M (2001) Computer prediction of human thermoregulatory and temperature responses to a wide range of environmental conditions. Int J Biometeorol 45(3):143–159

FLIR Systems Inc. (2016) http://www.flir.com

Grimmond CSB, Blackett M, Best MJ, Barlow J, Baik J-J, Belcher SE, Bohnenstengel SI, Calmet I, Chen F, Dandou A et al (2010) And The international urban energy balance models comparison project: first results from phase 1. J Appl Meteorol Climatol 49(6):1268–1292

Herrando M, Markides CN, Hellgardt K (2014) A UK-based assessment of hybrid PV and solar-thermal systems for domestic heating and power: system performance. Appl Energy 122:288–309

Jazwinski AH (1970) Stochastic processes and filtering theory, Elsevier, pp vii–viii

Jones AD, Underwood CP (2001) A thermal model for photovoltaic systems. Sol Energy 70(4):349–359

Juhl R (2016) Ctsmr: Ctsm for r. R package version 0.6.10

Juhl R, Moller J, Madsen H (2016) ctsmr - continuous time stochastic modeling in r, The R Journal

King DL, Boyson WE, Kratochvil JA (2004) Photovoltaic array performance model, http://energy.sandia.gov/download/21046/

Kotak Y, Gul MS, Muneer T, Ivanova SM (2015) Investigating the impact of ground albedo on the performance of pv systems

Krispel S, Peyerl M, Maier G, Weihs P (2017) Urban heat islands - reduktion von innerstädtischen wärmeinseln durch whitetopping. Bauphysik 39(1):33–40

Lindberg F, Grimmond CSB, Gabey A, Huang B, Kent CW, Sun T, Theeuwes NE, Järvi L, Ward HC, Capel-Timms I (2018) Urban multi-scale environmental predictor (umep): an integrated tool for city-based climate services. Environ Model Softw 99:70–87

Lindberg F, Grimmond CSB (2011) The influence of vegetation and building morphology on shadow patterns and mean radiant temperatures in urban areas: model development and evaluation. Theor Appl Climatol 105(3-4):311–323

Lindberg F, Grimmond CSB (2016) Solweig, http://urban-climate.net/umep/SOLWEIG

Lindberg F, Holmer B, Thorsson S (2008) SOLWEIG 1.0 – modelling spatial variations of 3d radiant fluxes and mean radiant temperature in complex urban settings. Int J Biometeorol 52(7):697–713

Lindberg F, Jonsson P, Honjo T, Wästberg D (2015) Solar energy on building envelopes - 3d modelling in a 2d environment. Sol Energy 115:369–378

Lindberg F, Onomura S, Grimmond CSB (2016) Influence of ground surface characteristics on the mean radiant temperature in urban areas. Int J Biometeorol 60(9):1439–1452

Lodi C, Bacher P, Cipriano J, Madsen H (2012) Modelling the heat dynamics of a monitored test reference environment for building integrated photovoltaic systems using stochastic differential equations. Energy and Buildings 50:273–281

Lumitos GmbH (2017) http://www.chemie.de/

Masson V (2000) A Physically-based scheme for the urban energy budget in atmospheric models. Bound-Layer Meteorol 94(3):357–397

Moigne PL (2012) Surfex scientific documentation

Moralejo-Vàzquez FJ, Martín-chivelet N, Olivieri L, Caamaño-martín E (2015) Luminous and solar characterization of PV modules for building integration. Energy and Buildings 103:326–337

Nielsen JN, Madsen H, Young PC (2000) Parameter estimation in stochastic differential equations: an overview. Annu Rev Control 24:83–94

Palyvos JA (2008) A survey of wind convection coefficient correlations for building envelope energy systems' modeling. Appl Therm Eng 28(8-9):801–808

PVEducation (2017) http://pvcdrom.pveducation.org/SUNLIGHT/MODTILT.HTM

Sharples S (1984) Full-scale measurements of convective energy losses from exterior building surfaces. Build Environ 19(1):31–39

Spencer JW (1971) http://www.mail-archive.com/sundial@uni-koeln.de/msg01050.html

Stull RB (ed.) (1988) An introduction to boundary layer meteorology, Springer Netherlands

UN (2014) World urbanization prospects, United Nations. visited on https://esa.un.org/unpd/wup/Publications/Files/WUP2014-Highlights.pdf

Weihs P, Staiger H, Tinz B, Batchvarova E, Rieder H, Vuilleumier L, Maturilli M, Jendritzky G (2011) The uncertainty of UTCI due to uncertainties in the determination of radiation fluxes derived from measured and observed meteorological data. Int J Biometeorol 56(3):537–555

ZAMG HoheWarte (2018) Meteorological measurements, data set from 1981 to 2017, Central Institution for Meteorology and Geodynamics

A.2 Other Contribution: II

H. Trimmel, P. Weihs, S. Faroux, H. Formayer, P. Hamer, K. Hasel, J. Laimighofer, D. Leidinger, V. Masson, I. Nadeem, S. M. Oswald, M. Revesz, and R. Schoetter. Thermal conditions during heat waves of a mid-European metropolis under consideration of climate change, urban development scenarios and resilience measures for the mid-21st century. *Meteorologische Zeitschrift*, 2019. doi: 10.1127/metz/2019/0966. URL `ttps://www.schweizerbart.de/papers/metz/detail/prepub/91938/Thermal_conditions_during_heat_waves_of_a_mid_Euro?af=crossref`.

Meteorol. Z. (Contrib. Atm. Sci.), PrePub DOI 10.1127/metz/2019/0966

DACH 2019

Thermal conditions during heat waves of a mid-European metropolis under consideration of climate change, urban development scenarios and resilience measures for the mid-21st century

Heidelinde Trimmel[1,6*], Philipp Weihs[1], Stéphanie Faroux[2], Herbert Formayer[1], Paul Hamer[6], Kristofer Hasel[1,4], Johannes Laimighofer[5], David Leidinger[1], Valéry Masson[2], Imran Nadeem[1], Sandro M. Oswald[1,3], Michael Revesz[1] and Robert Schoetter[2]

[1]Institute of Meteorology and Climatology, University of Natural Resources and Life Sciences (BOKU), Vienna, Austria
[2]CNRM, Université de Toulouse, Météo-France, Toulouse, France
[3]Zentralanstalt für Meteorologie und Geodynamik (ZAMG), Vienna, Austria
[4]Department of Meteorology and Geophysics, University of Vienna, Vienna, Austria
[5]Institute of Statistics, University of Natural Resources and Life Sciences (BOKU), Vienna, Austria
[6]Norsk institutt for luftforskning (NILU), Kjeller, Norway

(Manuscript received June 9, 2019; in revised form October 25, 2019; accepted October 28, 2019)

Abstract

In this study we produce two urban development scenarios estimating potential urban sprawl and optimized development concerning building construction, and we simulate their influence on air temperature, surface temperatures and human thermal comfort. We select two heat waves representative for present and future conditions of the mid 21st century and simulations are run with the Town Energy Balance Model (TEB) coupled online and offline to the Weather Research and Forecasting Model (WRF). Global and regional climate change under the RCP8.5 scenario causes an increase of daily maximum air temperature in Vienna by 7 K. The daily minimum air temperature will increase by 2–4 K. Changes caused by urban growth or densification mainly affect air temperature and human thermal comfort locally where new urbanisation takes place and does not occur significantly in the central districts. A combination of near zero-energy standards and increasing albedo of building materials on the city scale accomplishes a maximum reduction of urban canyon temperature achieved by changes in urban parameters of 0.9 K for the minima and 0.2 K for the maxima. Local scale changes of different adaptation measures show that insulation of buildings alone increases the maximum wall surface temperatures by more than 10 K or the maximum mean radiant temperature (MRT) in the canyon by 5 K. Therefore, measures to reduce MRT within the urban canyons like tree shade are needed to complement the proposed measures. This study concludes that the rising air temperatures expected by climate change puts an unprecedented heat burden on Viennese inhabitants, which cannot easily be reduced by measures concerning buildings within the city itself. Additionally, measures such as planting trees to provide shade, regional water sensitive planning and global reduction of greenhouse gas emissions in order to reduce temperature extremes are required.

Keywords: urban sprawl, climate change, heat waves, urban scenarios, resilience, TEB, WRF, UTCI

1 Introduction

The urban environment influences the atmospheric conditions at the surface in various ways. Air temperature is higher mainly at night in comparison to rural areas, which is well known as the urban heat island effect, (UHI, Landsberg, 1981; Oke, 1982; Grimmond et al., 2010). In addition, vapour pressure or specific humidity can be lower due to reduced water availability, and the radiation and wind fields are strongly altered by the three-dimensional building structures (Grimmond et al., 2010).

These effects might further increase due to strong urbanization trends, which includes densification and growth of existing urban agglomerations. For instance, until 2030, the population within the metropolitan area of Vienna is expected to increase by 10 % (ÖROK, 2017). This will cause an increase in the demand for gross floor area resulting in urban densification and/or urban expansion. However, even under current conditions, the population in Vienna is suffering from heat

*Corresponding author: Heidelinde Trimmel, Institute of Meteorology and Climatology, University of Natural Resources and Life Sciences (BOKU), Gregor Mendelstrasse 33, 1180 Vienna, Austria, e-mail: heidelinde.trimmel@boku.ac.at

stress during the summer months (Matzarakis et al., 2011; Muthers et al., 2010; MA 22, 2018). In the present article, we research the impact of the projected urban development in Vienna on human thermal comfort.

Rises in air temperature that can be expected due to climate change (APCC, 2014) present an additional threat to human thermal comfort in the urban realm. Air temperature has been rising and is expected to continue to rise globally within the next century (IPCC, 2013). In eastern Austria, mean air temperature has risen by 2 K since 1880, which is more than double the 0.85 K rise recorded globally (Auer et al., 2014). Emission scenario A1B projects that by the end of the 21st century mean air temperature increases of 3.5 K above the level of the reference period 1961–1990 are expected in Austria (APCC, 2014; Gobiet et al., 2014). Cities themselves contribute to climate change by the emissions caused by e.g., ground and air traffic, industrial processes, heating, electricity generation, waste and production of building material (De Pee et al., 2018; Bardow and Green, 2018; Kennedy et al., 2009).

Heat waves have been recognized as a lethal threat to humans around the world within the last decades (McMichael et al., 2003; Valleron and Boumendil, 2004; Kim and Kyselý, 2009; Grimmond et al., 2010: Gabriel and Endlicher, 2011) and also Vienna (Hutter et al., 2007). Additionally, the combination of the elevated air temperature during heat waves and high irradiation (Otani et al., 2017; Schreier et al., 2013), humidity (Steadman, 1979a, b) or air pollution (Kalisa et al., 2018; Schnell and Prather, 2017; Zhang et al., 2017) poses a threat to human health.

It has been found that the heat wave length and intensity will increase in the future, e.g., for Paris (Lemonsu et al., 2013) and also for Vienna (Formayer et al., 2007). Kyselý days are defined as days of a heatwave period, which is characterised by at least three subsequent days with daily maximum air temperature larger than 30 °C and continues until the daily maximum air temperature drops below 25 °C or until the mean daily maximum air temperature of the period drops below 30 °C (Kyselý et al., 2000). An increase of the number of Kyselý days by up to a factor of 10 from 1961–1990 to the end of the 21st century is expected by Formayer et al. (2007) for Vienna (Scenario A2, Model: HadRM3H; Jones et al., 2001). This alarming fact has caused various heat warning systems to be developed (Michelozzi et al., 2004; Tan et al., 2007).

To be able to project the thermal strain caused by future heat waves and urban growth it is necessary to have the appropriate tools that can take into account as many of the involved physical processes as possible (especially in the context of a changing climate). This includes microscale processes such as reflections within the urban canyon, wind reduction, energy uptake and storage in roads and buildings resolved, e.g., by the town and energy balance scheme TEB (Masson, 2000; Masson et al., 2002; Bueno et al., 2012; Pigeon et al., 2014). Furthermore, representations of evapotranspiration by urban vegetation, which have been implemented in TEB (Lemonsu et al., 2012; DeMunck et al., 2013), city scale effects caused by spatial inhomogeneity (e.g., potential thermal breezes), and topography (e.g., topographically-generated or modified winds) are of key importance. Finally, the interaction between the surface layer and the atmosphere and its effects on the evolution of the urban boundary layer are crucial (Oke, 1987; Stull, 1988, Bornstein and Lin, 2000; Grimmond et al., 2010) as it is done in atmospheric models, e.g., the weather research and forecasting model WRF (Skamarock et al., 2008).

In this study we will work with resilience measures, because we want to point out that the aim of urban development should be to make the city more resilient – or to better cope and maintain function during climatic extremes (Zommers and Alverson, 2018). Resilience covers the more holistic approach of urban planning (Sharifi and Yamagata, 2018; Ürge-Vorsatz et al., 2018). Here, we will apply some basic changes in material properties as a first and important step to help to reduce thermal strain in urban agglomerations and thus increase resilience.

To measure the subjective perception of temperature there are many indices describing human thermal comfort (PMV (Fanger, 1970), PET (Mayer and Höppe, 1987), UTCI (Fiala et al., 2001; Bröde et al., 2012; Jendritzky et al., 2012)), heat stress or apparent temperature (humidex, wind chill, wet-bulb globe temperature). Generally important factors for the human organism are the radiation received by humans, the ambient air temperature, humidity and wind speed (Mayer and Höppe, 1987). There is a positive relationship between human thermal stress and increasing MRT for the warm part of the thermal comfort spectrum. In this thermal comfort range the relation to air temperature and water vapour pressure even increases with higher air temperatures (Dou, 2014). In this study the Universal Thermal Climate Index (UTCI) is used.

The aim of this article is, to present:

1. The setup of a mesoscale meteorological model coupled to an urban energy balance model (Section 2.1)
2. Future urban scenarios for Vienna (Section 2.3 and 2.4)
3. The change of the 2 m air temperature for a selected present and a future heat wave on city level (Section 3.1):
   - Daily maximum temperature, as a factor for human thermal strain
   - Daily minimum temperature, to quantify the nocturnal canopy urban heat island (CUHI) magnitude
   - The influence of urban sprawl and densification

4. Analysis of the effects of different resilience measures on a local level (Section 3.2):
   - Energy flux differences, which are transferred from the urban surface to the atmospheric model
   - The surface temperatures of roof, wall and road, to understand the air temperature changes
5. Analysis of canyon parameters to estimate thermal strain in the idealized canyon (Section 3.3)

We do not address the detail planning within the street canyons, but urban development regarding urban material choice, distribution and density of built land on a scale > 100 m.

2 Materials and methods

2.1 Modelling Framework

In this study, the open-source mesoscale atmospheric model WRFv3.9.1 (Skamarock et al., 2008) is used in combination with an urban canopy model called the Town Energy Balance (TEB; Masson, 2000; Masson et al., 2002) model. Both models are coupled and run online. Additionally, offline simulation runs were done by forcing TEB as it is integrated in SURFEXv8 (Boone et al., 2017) with the output of WRF-TEB.

WRF is used to downscale the ECMWF Analysis Data Set for present-day conditions (temporal resolution of 6 hours, horizontal resolution of 9 km (https://www.ecmwf.int/en/forecasts/datasets/set-i) via two intermediate nests (3 km and 1 km resolution) using one-way grid nesting to a 333 m resolution domain covering the city of Vienna (Figure A-1). There are 40 vertical levels in the WRF simulations, thereof 7 below 1000 m. For the topographical elevation, the SRTM1Arc:30 m data set is used. The Yonsei University Scheme is used for the Planetary Boundary Layer scheme together with the NOAH Land Surface Model to model the land-atmosphere interaction. For the land cover information, the Corine data (EEA, 2012) was reclassified to USGS classes (30 non-urban, 3 urban) (Table B-1) in order to be consistent with WRF (Schicker et al., 2016).

For the future heat wave conditions, we use selected events from regional climate model simulations forced by different representative concentration pathways (RCPs) to force our WRF-TEB simulations. The details of the regional climate model simulations, the heat wave selection process, and the coupling with WRF are described in Section 2.5.

Our different future urban development scenarios representing urban densification and sprawl are created by modifying the Corine land surface dataset using specific information regarding expected urban growth. The details of these urban development scenarios, and how they are created and applied is described in Section 2.4.

TEB version 1.1550 is implemented in the Weather Research and Forecasting (WRF) model. The Town Energy Balance (TEB) model developed by Masson (2000) is a physically based single-layer urban canopy scheme that is designed for urban surface parameterization of atmospheric models. The building energy model (BEM) that has been integrated in the TEB scheme (Bueno et al., 2012) is also deployed in the coupling. BEM-TEB makes it possible to represent the energy effects of buildings and building systems on the local urban climate and to provide estimations of the building energy consumption at the city scale with a resolution of down to 100 m.

The TEB scheme takes meteorological parameters at the lowest level of WRF as input. These parameters are air temperature and specific humidity, wind speed and direction, air pressure, direct and diffuse downwelling solar radiation, downwelling longwave radiation and precipitation. In return, TEB provides roof, road and wall temperature, emissivity, latent, sensible heat and momentum fluxes to the WRF model as output. In addition, 2-m temperature, 2-m humidity, and 10-m wind are obtained from the diagnosed TEB canyon temperature, humidity, and wind, respectively.

The URBPARAM.TBL and registry files in WRF have also been modified to accommodate urban parameters required by TEB-BEM and to write out urban parameters in the model output. All necessary conversions (e.g., specific humidity to mixing ratio) are done. We use the canyon temperature calculated by TEB for the calculation of the 2 m air temperature of WRF-TEB within urban areas. The coupled model WRF-TEB uses the same spatial resolution as the original WRF.

Offline simulations using SURFEXv8 were done due to different reasons. First, the simulation time was much faster and so more resilience measures could be simulated, as would have been possible with the online version, second some resilience measures (green roofs and photovoltaic on roofs) have not been implemented in WRF-TEB, but in SURFEXv8 and third SURFEXv8 offers the calculation of the thermal index UTCI. We analysed various results from the offline simulations: the energy fluxes, surface temperature, canyon air temperature, mean radiant temperature and UTCI. Here, mainly shaded UTCI is used, which is the UTCI calculated only from influences by diffuse radiation, without the direct component. Therefore, it can also be calculated when no buildings are present. The direct component is so pronounced, that in this study we found that there is no way to improve the UTCI in the sun during summer heat waves, only conditions can be made more bearable in the shadow.

2.2 Validation and uncertainties

The energy fluxes and surface temperatures of roof, wall and road temperatures calculated by TEB have been validated by Masson et al. (2002) for Vancouver and Mexico City. For Mexico City the road and roof temperatures showed a bias of 4 and 1.9 K, and a RMSE of 4.2 and 4.5 K. The radiation, turbulent (sensible+latent) and storage fluxes showed a bias of 10, −3 and 13 W m^{-1}, respectively, and a RMSE of 32, 25 and 38 W m^{-1}. For Vancouver the wall and roof temperatures showed a bias of 2.3 and 2.5 K and a RMSE of 3 and 7.3 K. Further TEB was validated for Marseille (Lemonsu et al., 2004), Ouagadougou (Offerle et al., 2005) and cold climates, which is not relevant here. The BEM was validated by Pigeon et al. (2014) for Paris. In addition, we validated the 2 m air temperature in different Viennese urban canyons and found a mean absolute error for WRF-TEB between 0.99 and 1.51 K, and the RMSE was between 1.3 and 1.89 (Table A-1).

The water vapour pressure calculated from WRF-TEB is compared to measurements at Wien Hohe Warte (Figure A-7) and Wien Innere Stadt (Figure A-8). An RMSE of 2.68 and 2.03, a bias of 1.55 and 0.28, respectively, were found. Under the circumstances described above, the imprecisions lead to an uncertainty of 0.2–0.3 K in the UTCI.

If we use the meteorological conditions of the future heat wave to estimate the forward propagation of a potential error of air temperature in the range of the calculated RMSE of 1.9 K, then we find that the UTCI increases directly with the air temperature, so this error would result in an increase of 1.9 K in UTCI as well.

The MRT and UTCI calculated by TEB was compared with the results of the higher spatially resolved model SOLWEIG. The validation is described in more detail in Annex A.

2.3 Definition of urban parameters of Vienna

In order to run the simulations, the urban parameters were derived for Vienna. First, they were obtained for the finest available scale, then aggregated on block scale of the Viennese municipal land use map (Realnutzungskartierung – https://www.wien.gv.at/stadtentwicklung/grundlagen/stadtforschung/siedlungsentwicklung/realnutzungskartierung/pdf/rnk-2012.pdf). This method was oriented on the study by Cordeau (2016) and a graphical overview can also be found in the Annex (Figure B-1). The surface ratios of built, sealed and unsealed surface were derived from the highly detailed vector land cover data set (Flächenmehrzweckkarte – Viennese building height model (Baukörpermodell – https://www.wien.gv.at/stadtentwicklung/stadtvermessung/geodaten/bkm). Building roughness height was estimated as 1/10$^{\text{th}}$ of building height. The vertical to horizontal wall ratio was calculated using the above-mentioned vector data sets. The physical building parameters were derived by linking a dataset of building age and typology with typical building parameters obtained from different studies (Berger et al., 2012; Amtmann and Altmann-Mavaddat, 2014) and the OIB (Austrian Institute of Construction Engineering). More information about the mapping of physical building parameters can be found in Annex B. Because the selected outer model domain covers 417 km × 297 km (Figure A-1) and thus is much larger than the area for which the LCZ map could be produced and WRF is not able to include all LCZ classes, so the Corine 2012 data set was used in this study. Unlike the LCZs and the UrbanAtlas, Corine 2012 is available for all WRF domains, and there is existing methodology for how to use Corine in WRF (Pineda et al., 2004; Schicker et al., 2016). Corine is updated every 6 years. After this there might be even update cycles of 5 years, which makes it a very useful dataset.

While the standard version of WRF reclassifies Corine to USGS classes and thereby regroups all urban classes of Corine (1–11) to one urban class (Pineda et al., 2004), WRF-TEB is enhanced to support the use of 3 urban classes. In order to take into account non-built and vegetated urban areas, some urban classes of Corine are reclassified to USGS Nature classes (Table B-1). The parameters are thus extracted for these classes. The final model setup is listed in Table B-2.

2.4 Urban Scenarios

In this study next to the actual Corine land use data set two adapted "future" Corine data sets were created which show differing urban distributions (see Annex C). A further additional five scenarios, where only urban parameters were changed are prepared (2.4.2). An overview of the parameters used is given in Table 1. The "reference scenario" (REF) is the base scenario and shows the distribution of urban area according to the Corine 2012 data set, generalized to USGS Classes (Fig. 1a). The two urban development scenarios "urban sprawl" (SPR) and "optimized city" (OPT) both assume the same increase of population and estimated gross floor area demand (see Annex C, Table C-1), but under different spatial distribution (see Annex C, Table C-2). SPR assumes the same material property as REF. OPT uses modified urban parameters as described in Section 2.4.1.

2.4.1 Change in material properties

Apart from the spatial changes, the OPT scenario differs in two aspects, which are intended to represent selected effective resilience measures which can potentially be implemented in Vienna to counteract climate change and to reduce the urban heat island within the possibility of the modelling framework (Table 1). This reduction is aimed to be achieved mainly by reduction of heat uptake by increasing reflection and by preventing heat transfer into the building and not by increasing the latent heat flux to avoid sultriness, which can play an important role at high air temperatures (Steadman, 1979a, b). Tree shade, which is a very important measure to improve human thermal comfort at street level could not be included in the study due to model constraints. It is assumed that the same resilience measures are applied to all three urban categories to obtain maximum effects.

Table 1: Overview of all presented scenarios: reference scenario (REF), the urban development scenarios: urban sprawl (SPR), optimized city (OPT), the resilience measure scenarios: increased albedo (ALB), decreased thermal conductivity of urban materials (INS), increased urban density (DEN), implementation of green roofs (GRR), installation of photovoltaic panels on roofs (PVR).

Name of urban scenario:	REF	SPR	OPT	ALB	INS	DEN	GRR	PVR
Total built urban area [km^2]	929	1115	939	929	929	929	929	929
relative to "REF" [%]	100 %	120 %	101 %	100 %	100 %	100 %	100 %	100 %
built area in urban category:								
low density residential [%]	22	22	24.2	22	22	24.2	22	22
high density residential [%]	46	46	46.2	46	46	46	46	46
commercial [%]	16	16	24.2	16	16	24.2	16	16
Thermal conductivity, roof [W/mK]	1.7	1.7	0.1	1.7	0.1	1.7	1.7	1.7
Thermal conductivity, wall [W/mK]	1.4	1.4	0.1	1.4	0.1	1.4	1.4	1.4
Thermal conductivity, ground [W/mK]	0.9	0.9	0.4	0.9	0.4	0.9	0.9	0.9
Albedo, roof [–]	0.15	0.15	0.68	0.68	0.15	0.15	0.154	0.1
Albedo, wall [–]	0.2	0.2	0.3	0.3	0.2	0.2	0.2	0.2
Albedo, ground [–]	0.138	0.138	0.3	0.3	0.138	0.138	0.138	0.138
Green roof fraction [–]	0	0	0	0	0	0	1	0
Photovoltaic fraction on roofs [–]	0	0	0	0	0	0	0	1
WRF-TEB online forcing for SURFEX offline simulations	REF	SPR	OPT	REF	REF	REF	REF	REF

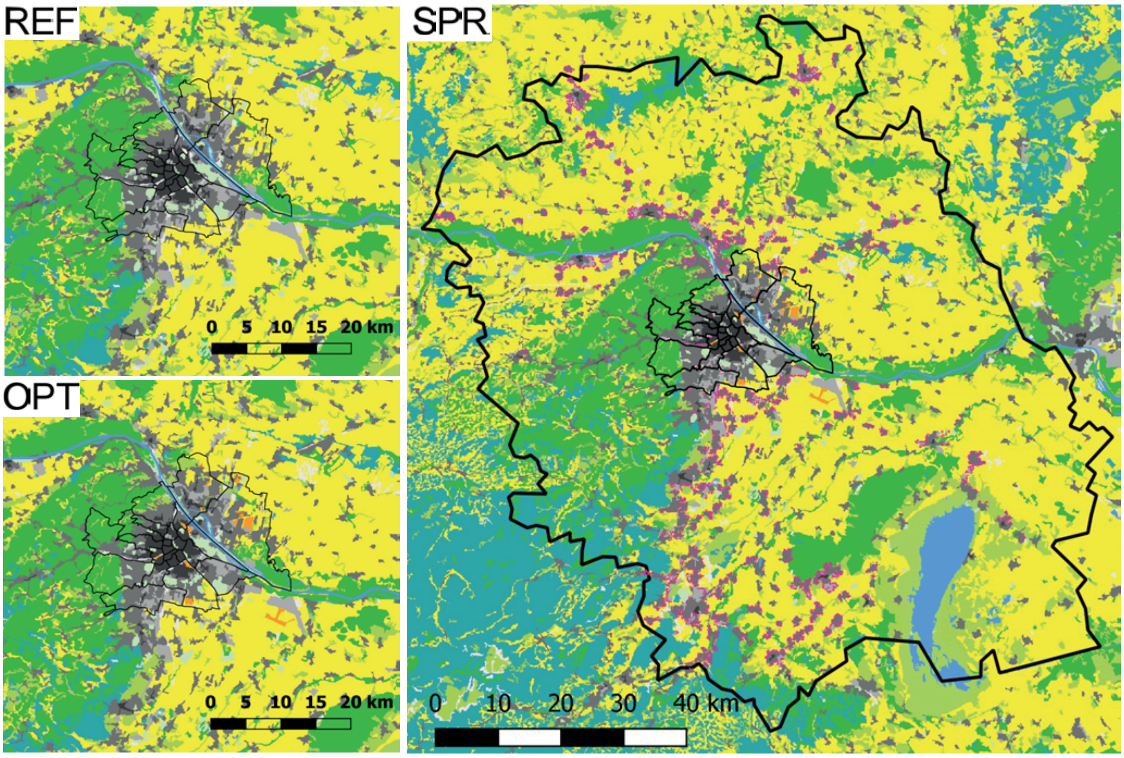

Figure 1: Spatial location of urban area in the three urban development scenarios: a) REF (up left), b) SPR (right) and c) OPT (down left). Actual urban areas are dark, middle and bright grey (high density residential, low density residential and commercial). Additional urban sprawl areas are purple. Known development areas are orange. Vegetation areas: yellow: dryland cropland and pasture (USGS class 2), bright green: mixed dryland/irrigated cropland and pasture (USGS class 4), brown-green: crops, shrubs, woodland mosaic (USGS classes 6+9), dark-green: deciduous forest (USGS class 11), blue-green: mixed forest (USGS class 15). The green areas surrounding the lake Neusiedel (south east of the region) is herbaceous wetland. The district borders of Vienna are thin black lines. The thick black line shows the border of stadtregion+ (PGO 2011).

The pre-1919 structure of Vienna is rather uniform, consisting of mainly brick, partly lime stone walls of about 50 cm thickness. They are not insulated, have double glazing windows and a steep roof constructions covered with clay bricks. The more recent buildings are more diverse regarding morphology as well as physical parameters related to building construction practices (e.g., the main wall material and insulation material).

The first measure consists of enhancing the building insulation. The thermal conductivity of the roof and walls is decreased to 0.1 W/mK, which is the nearly zero-energy standard and required for all new buildings after 2020 according to the Energy Performance of Buildings Directive EPBD (http://data.europa.eu/eli/dir/2018/844/oj; Amtmann and Altmann-Mavaddat, 2014). The thermal conductivity of windows is decreased to 0.9 W/mK, which is a typical value used in refurbishment of multistoried buildings (Amtmann and Altmann-Mavaddat, 2014). The thermal conductivity of roads is decreased to 0.4 W/mK, which is the lower boundary for medium concrete (https://www.engineeringtoolbox.com/thermal-conductivity-d_429.html). This change in material properties leads to a strong reduction of heat uptake by urban materials during the day, which is expected to cool the city during the evening, thus it might be an important factor for more effective cooling of rooms that have heated up. During the day, the well insulated urban structure is expected to take up less energy, which could lead to higher air temperatures during the day.

The second measure is intended to counteract the higher air temperature during the day due to the enhanced building insulation. The albedo of the walls and roads is only slightly increased from 0.2 and 0.13, respectively, to 0.3, which increases reflection of solar radiation, but also can help to reduce air temperatures (Krispel et al., 2017; Weihs et al., 2018). The albedo of the roof is increased to 0.68, which is technically possible and more effective in order to reduce sensible heat flux, as has been investigated in various studies (Taha et al., 1997; Morini et al., 2016; Žuvela-Aloise et al., 2018). Fallmann et al. (2016) showed further that such measures are not likely to have known negative effects on the boundary layer height and pollutant concentrations. The albedo increase mainly counteracts the increase in air temperature during sunlit hours. Therefore, all negative effects of decreased thermal conductivity should be mitigated. Ramamurthy et al. (2015) analyzed the effectiveness insulation and high reflective roofs with an urban canopy model and suggests a combination. We note that the increase in albedo values does not depend on water availability and space demands, but it does compete with available surface areas for photovoltaic and green roof surfaces.

2.4.2 Resilience measures

The different resilience measures used in the OPT scenario are simulated separately in order to allow for a precise attribution of their effect. In the following, the reduction of thermal conductivity is referred hereinafter as INS, the increase of albedo as ALB, and the densification caused by changes of built area from 0.22 (low residential areas) and 0.16 (commercial areas) to 0.242 as DEN. In addition, further potential mitigation and adaptation measures are investigated. These are a green roof (referred hereinafter as GRR) and a photovoltaic roof (referred hereinafter as PVR) scenario. For the GRR, the green roof module is used (De Munck et al., 2013). An extensive roof coverage using sedum is assumed. For PVR, the photovoltaic roof module is used (Masson et al., 2014) assuming an efficiency of 20 % and an albedo of 10 % for the solar panels. An overview of all employed scenarios is given in Table 1. All these measures are applied on 100 % of the roof surface, which is a first and rather extreme approximation to estimate the potential maximum effects of such resilience measures. Apart from being adaptation measures, which mitigate the urban heat island by reducing air temperatures by conversion of sunlight to either electric current or photosynthesis and evapotranspiration at roof level, PVR is an effective mitigative measure, which helps to avoid greenhouse gas emissions. Green roofs, as active soil and vegetation layer could help to mitigate high green house gas concentrations in the atmosphere as a carbon sink (Li and Babcock, 2014).

2.5 Present and future heat wave

An analysis of 15-yearly events is done in order to select suitable heat waves from external data that can be used to force the WRF simulations. The selected heat waves are 15 year return period events taken from the historical climate period (1988–2017, centred at 2002, “hw15yACT”) and also a future climate period (2036–2065, centred at 2050, “hw15ySCE”). The selection is based on the average daily maximum 2 m air temperature of heat waves (5 days). The historical heat wave is selected using observational data at the station Wien Hohe Warte supplied by the Austrian weather service ZAMG. The 5 day average daily maximum air temperature is calculated for the last 30 years (1988 to 2017) and the return period of these 5 day events is estimated using the Generalized Extreme Value Distribution (GEV; Fisher and Tippett, 1928). Due to the strong positive trend of more than 2 K within the last three decades for daily maximum air temperature, the data are detrended before applying the GEV.

As a reference heat wave for present-day modelling we choose the most intense 5 day heat wave of 1988–2017, which occurred in summer of 2015 with a 5 day temperature maximum mean of 36.3 °C (Table 2). According to the GEV distribution this event represents a heat wave with a return period of 15 years.

The regional climate change scenarios are based on the ensemble ÖKS 15 (Leuprecht et al., 2017; BMNT, 2016), a selection of 26 regional climate model scenarios from EURO-CORDEX (Jacob et al., 2014), derived

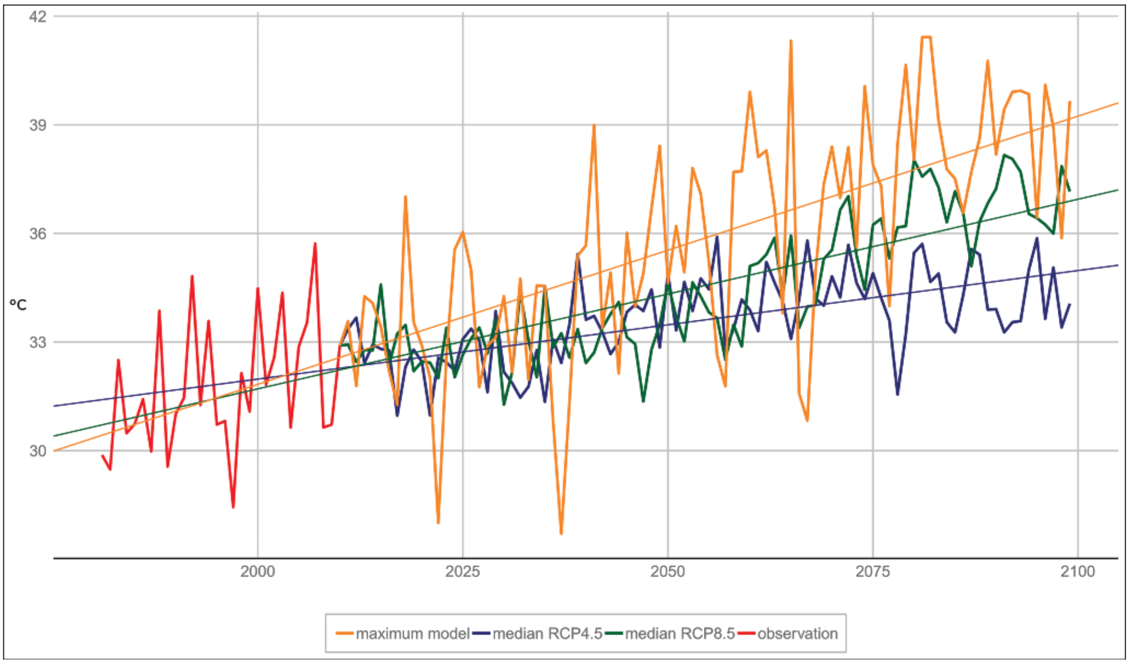

Figure 2: Maximum 5 day heat wave temperature (average of the daily temperature maximum of five consecutive days) per year at Vienna Hohe Warte observed (red), median of all scenarios forced with RCP4.5 (blue), median of all scenarios forced with RCP8.5 (green), scenario with the strongest trend of the whole ensemble (orange) and linear trend lines.

Table 2: Average daily maximum 2 m air temperature of heat waves (5 days) with 1, 2 and 15 year return periods derived from the station observations of Vienna Hohe Warte for the period 1988–2017 (first row) and climate change signals (2036–2065 versus 1988–2017) for this indicator based on the ÖKS 15 scenarios (Leuprecht et al., 2017) at a 1 km^2 grid cell at the same location.

Emission scenario/Return period	1 year	2 year	15 year
Observation (1988–2017) [°C]	28.7	31.6	36.3
RCP 4.5 ensemble median [K]	1.5	2.2	2.5
RCP 8.5 ensemble median [K]	1.8	2.7	2.2
Ensemble maximum [K]	5.9	3.7	4.8

from different global (Taylor et al., 2012) and regional climate models and forced with the emission scenarios RCP4.5 and RCP8.5. The ÖKS15 ensemble provides bias-corrected and localized (1 km) scenarios for daily minimum and maximum temperature, daily precipitation and daily radiation. Bias correction was done using a quantile mapping as described in Switanek et al. (2017). As only the daily maximum temperature is used for the quantification of the meteorological trend of the maximum temperature during 5 day heat waves, the spatial resolution of 1 km is sufficient.

For every ensemble member of ÖKS 15, we calculate the annual maximum 5-day mean of the daily maximum air temperature for the grid cell representing Hohe Warte in Vienna. Using the same GEV method we calculate the heat wave air temperature for return periods of 1, 2 and 15 year events for the historical period 1988–2017 and the future period of 2036–2065. In Fig. 2, the development of the maximum 5-day heat wave air temperature per year is shown for observations (red), the ensemble median of all scenarios forced with RCP4.5 (blue), RCP8.5 (green) and the scenario with the strongest trend in heat wave air temperature of the whole ensemble (orange).

The observed heat wave air temperature at Wien Hohe Warte for 1, 2 and 15 year events of the period 1988–2017 and the climate change signal until the middle of the 21st century is given in Table 2. There are no large differences for the ensemble means between the two emission scenarios until the middle of the century. For the 15 year event, the RCP4.5 ensemble shows even a 0.3 K stronger warming than RCP8.5. However, there is a more pronounced warming seen when the more extreme heat waves occur. The 1 year events show a warming between 1.5 and 1.8 K and the 2 and 15 year events have a warming between 2.2 and 2.7 K. For the ensemble maximum scenario this relation is not seen and the strongest warming is for the 1 year event.

For the selection of the future scenario we chose the historical 15 year event heat wave air temperature (36.3 °C) and added the climate change signal of the 15 year event from the most extreme scenario (4.8 K). This choice can be interpreted as a plausible worst case scenario until the middle of the 21st century. This ex-

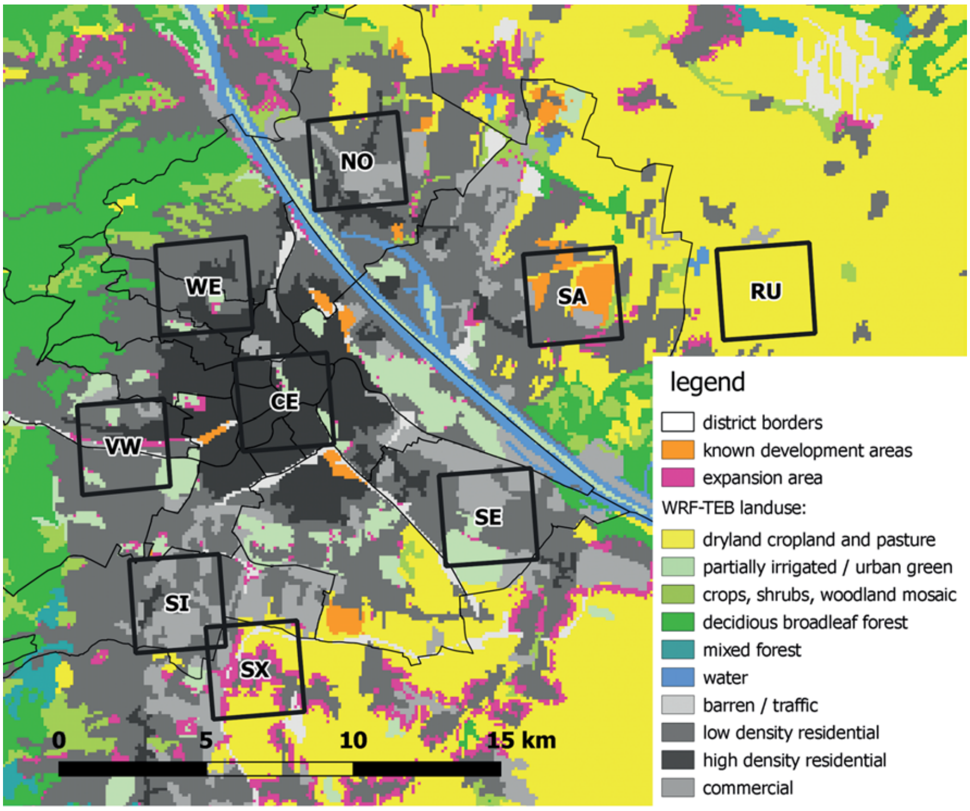

Figure 3: Subregions chosen for further analysis (clockwise): Central Districts (CE), North-Rim (NO), New development areas: Seestadt Aspern (SA), South-eastern rim (SE), South-industrial (SI), South expansion (SX), Valley of Wien (VW), West – elevated low density residential (WE), Rural area (RU).

Table 3: Mean values for Town Fraction (FRAC_TOWN) as they were calculated within this study, Built fraction [-] (D_BLD), Unsealed fraction [-] (D_GARDEN), Building height [m] (D_BLD_HEIG) and Vertical to horizontal wall factor [-] (D_WALL_O_H) for the Subregions of Fig. 3.

	CE	NO	RU	SA	SE	SI	SX	VW	WE
FRAC_TOWN	0.95	0.9	0.05	0.46	0.89	0.95	0.47	0.84	0.88
D_BLD	0.43	0.23	0.16	0.21	0.19	0.21	0.19	0.25	0.25
D_GARDEN	0.19	0.5	0.54	0.53	0.53	0.52	0.53	0.47	0.47
D_BLD_HEIG	18.75	11.44	11.2	10.68	10.9	11.13	10.85	12.11	11.85
D_WALL_O_H	1.75	1.11	0.5	1.08	0.83	1	0.89	1.2	1.27

treme climate scenario should also maximise the impact of the change of the urban structure (temperature increase) and should help to identify possible interactions between climate and land-use changes.

The lateral boundary conditions for a heat wave that fulfils the air temperature criteria (41.3 °C average 5 day daily maximum air temperature) are taken from a high-resolution regional climate scenario simulation. This simulation is based on the global model GFDL-CM3 (Donner et al., 2011) forced with the RCP8.5 emission scenario and downscaled with the WRF model (Michalakes et al., 2001) with an optimized set up for the Alpine region (Arnold et al., 2011). The regional model has a 10 km^2 spatial resolution and was run for the Alpine region and the whole 21st century. In addition to the 5-day period, a spin-up period of two–three days is used.

2.6 Study regions

For the presentation of the results, 9 areas of 9×9 model grid cells each (total of each area: 81 cells, 9 km^2) are chosen to represent the variety within Vienna (Fig. 3, Table 3). The main subregion covers the central districts.

The magnitude of the urban heat island is quantified by calculating the spatial mean difference in the daily minimum values in 2 m air temperature between the grid cells of the central districts subregion (CE) and the rural (RU) subregion. The new development areas around Seestadt Aspern (SA) are chosen to quantify the change caused by the erection of this new built urban area. North-Rim (NO), South-industrial (SI), South-eastern rim (SE), are chosen as areas with high industrial coverage, which is likely to be densified, but are in suburban areas in different cardinal directions and thus exposed to different wind regimes. South expansion (SE) is chosen as another suburban area where urban densification is unlikely but urban sprawl is likely. Furthermore, a subregion in the west-elevated low density residential (WE) was chosen as representative for the climatological situation in the areas influenced by the far reaching forested and hilly areas west of Vienna and without change in the land use. Finally, an area in the Valley of Wien (VW) shall give information about changes in this area, which is climatologically distinct due to a valley breeze.

3 Results

Two reference heat waves were run for present (hw15yACT) and future (hw15ySCE) conditions. They were selected by their air temperature value. They both have very low wind speeds during the night (1 m/s) – so there is hardly any air advected (Figure D-1). During the day the wind ranges between 3 and 4 m/s. For hw15yACT it is from East to Southeast, for hw15ySCE it is from East to Northeast (Figure D-1). There were some disturbances in the downward shortwave flux at the ground surfaces (Figure D-2). So, these days were excluded together with the spin up time. Consequently, for hw15yACT 9, 10, 12 and 13 August 2015 (day 4, 5, 7 and 8) is used. For hw15ySCE 7 and 8 July 2069 (day 7 and 8) is used. The minima and maximum values for 2 m air temperature, MRT, canyon air temperature and UTCI shade are calculated using all daily extremes of each of the 81 grid cells of the cloud free days of the selected period. For the present heat wave these are 324 values (4 days), for the future heat wave there are 162 values (2 days).

The air advected from either of these directions stems mainly from agricultural plains. The 2 m air temperature in these agricultural regions are rather uniform with spatial differences smaller than 1 K for hw15yACT and 2 K for hw15ySCE (Figure D-3). Also, the simulated humidity field is uniform with spatial deviations from less than 2 g kg^{-1} (Figure D-4). The future heat wave shows temperatures above 40 °C with a mixing ratio of 10 g kg^{-1} (mean water vapour pressure of 13.5 hPa). Both simulations have a surface pressure below 1000 hPa. For the present heat wave the dew point temperature did not surpass critical levels to cause sultriness. Also, for the future heat wave non-sultry conditions are expected. Soil moisture is declining near the surface during the heat wave (Figure D-5).

3.1 Viennese future heat load (T_{max}) and UHI (T_{min})

3.1.1 Reference scenario

The average daily maximum air temperature simulated by WRF-TEB (T_{max}) increases by about 7 K between the historical and future heat wave (Fig. 5). Simulated average daily minimum air temperature (T_{min}) increases between 2 and 4 K (Fig. 5). In the central districts the mean increases are 6.7 K and 3.2 K, respectively. The median values are slightly higher (6.8 K and 3.4 K). The variation of T_{min} between the different areas is higher than that of T_{max}. The urban-rural difference of the T_{min} between Vienna city centre (CE) and the eastern agricultural areas (RU) for the present heat wave is 3.0 K. For the future heat wave, the urban-rural difference is greatly increased to 4.6 K (Fig. 4, 5, 6).

3.1.2 Future urban scenarios

The urban scenarios show a larger effect on minimum than on maximum air temperature (Fig. 5, 6). The influence on air temperature is generally less than 1 K, which is low compared to the air temperature increase due to climate change projected by the climate models (Fig. 5, 6). While SPR increases T_{min}, OPT decreases T_{min} for hw15yACT (Fig. 4 upper middle and right) and for hw15ySCE (Fig. 6). For SPR, the T_{max} changes less than 0.1 K (Fig. 5). For OPT, the T_{max} decreases in the range of 0.5 K for the subregions CE, SI, SX, VW and WE (Fig. 5).

3.2 Effects of resilience measures

The components of the OPT scenario (ALB, INS, DEN) as well as GRR and PVR are further analyzed.

First, the general influence on the town heat fluxes is shown for CE (3.2.1). Then the surface temperature of roof, ground and wall show more information (3.2.2).

3.2.1 Town energy fluxes in the central districts

At daytime for the ALB scenario, a reduction of up to 180 W/m^2 in net radiation and of about 100 W/m^2 in sensible heat flux is simulated. The effects are relatively constant throughout the heat wave (Fig. 7a). The INS scenario shows during the day on the one hand a decrease of the ground heat flux up to 150 W/m^2, but an increase of the same magnitude of the sensible heat flux. During nighttime, the sensible heat flux is decreased up to 100 W/m^2 (Fig. 7b) and thus also air temperature is lower at night. The change in energy balance is mainly negative, with a declining trend. Also, the difference of sensible heat flux during the day shows a declining trend towards the end of the heat wave. For the DEN scenario, the ground heat flux increases by 100 W/m^2 during the day and decreases by 30 W/m^2 during the night (Fig. 7c). The implementation of green roofs (GRR) increases net radiation by up to 80 W/m^2 during the day – an effect

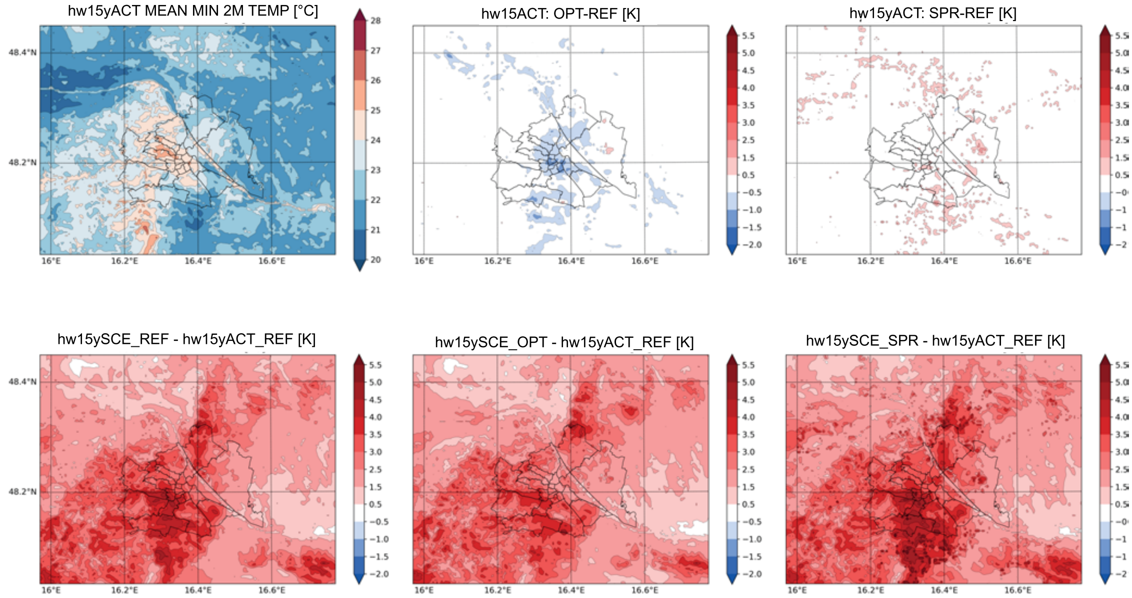

Figure 4: Mean minimum of the selected cloud free days for each grid cell for the daily 2 m minimum air temperature for the present heat wave hw15yACT (upper left). Differences between reference scenario hw15yACT and urban development scenarios OPT (middle) and SPR (right) (upper panels). Differences between reference scenario for present (hw15yACT) and future (hw15yrSCE) for the REF (left), OPT (middle) and SPR (right) urban development scenario (lower panels).

that diminishes to the end of the heat wave (Fig. 7d). The latent heat flux increases by up to 230 W/m^2, the sensible heat flux decreases by up to 100 W/m^2. The implementation of solar panels (PVR) decreases both the sensible heat flux and the net radiation by about 100 W/m^2 (Fig. 7e).

3.2.2 Surface temperatures of roof, wall and road in the central districts

On the roof five resilience measures show different properties. This causes a different increase in roof surface temperature during the day (Fig. 8a). The strongest diurnal amplitude is seen in INS. GRR and ALB both have cooler roof surfaces than REF. PVR stays coolest under the assumptions of this study.

The surfaces within the canyon are only altered in ALB and INS, therefore only these resilience measures are shown for wall and road. On the unsealed fraction there are no changes done. The wall surfaces show that INS strongly alters the wall surface temperature compared to REF. During daytime, there is an increase by more than 10 K and during night a decrease of up to 5 K (Fig. 8b).

The road surface temperatures show the least changes, but also here it can be seen that INS increases the maximum surface temperature whereas ALB decreases it (Fig. 8c).

3.3 Canyon parameters and human thermal stress

Finally, the parameters relevant to quantify human thermal stress or comfort are analyzed within the street canyon. For the canyon wind speed no changes greater than 0.5 m/s have been found. Also, the canyon humidity changes are $\ll 0.01$ kg/kg. For the MRT and canyon air temperature there do exist notable changes. During heat waves after MRT, the air temperature has a great impact on determining whether the UTCI reaches thermal stress levels or stays in the human thermal comfort region. Therefore, the effect of the separate measures on the mean radiant temperature and canyon air temperature was analyzed. In Fig. 9 timeseries of MRT and canyon air temperature during the whole heat wave hw15ySCE are shown for the central districts (CE). Table 4, 5 and 5 give additional information about the minima and maxima in the subregions.

3.3.1 MRT

The MRT maxima for the reference scenario increase by 6.6 K in the shade and 7.6 K in the sun between the present and future scenario for the central districts (Table 4a). For GRR, DEN and PVR the difference in MRT maxima to the reference scenario was less than 0.2 K (Table 4b, 4c) for all subregions. For ALB the mean increase of maximum MRT is 2.3 (Table 4c, Fig. 9a) for CE. For INS the MRT increased during day up to 8 K

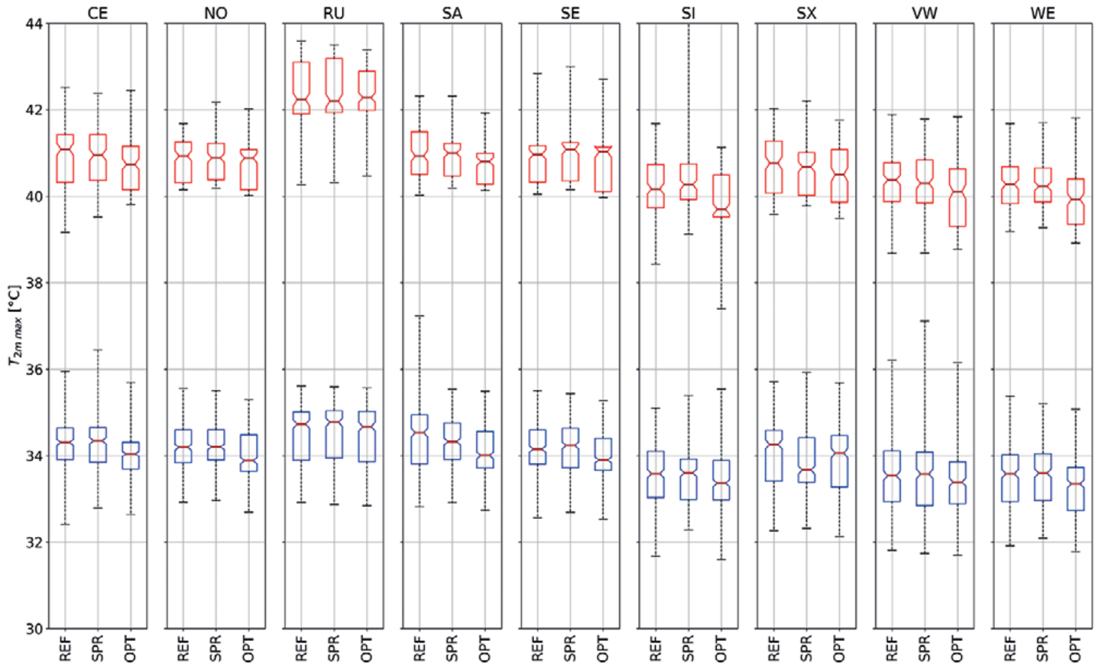

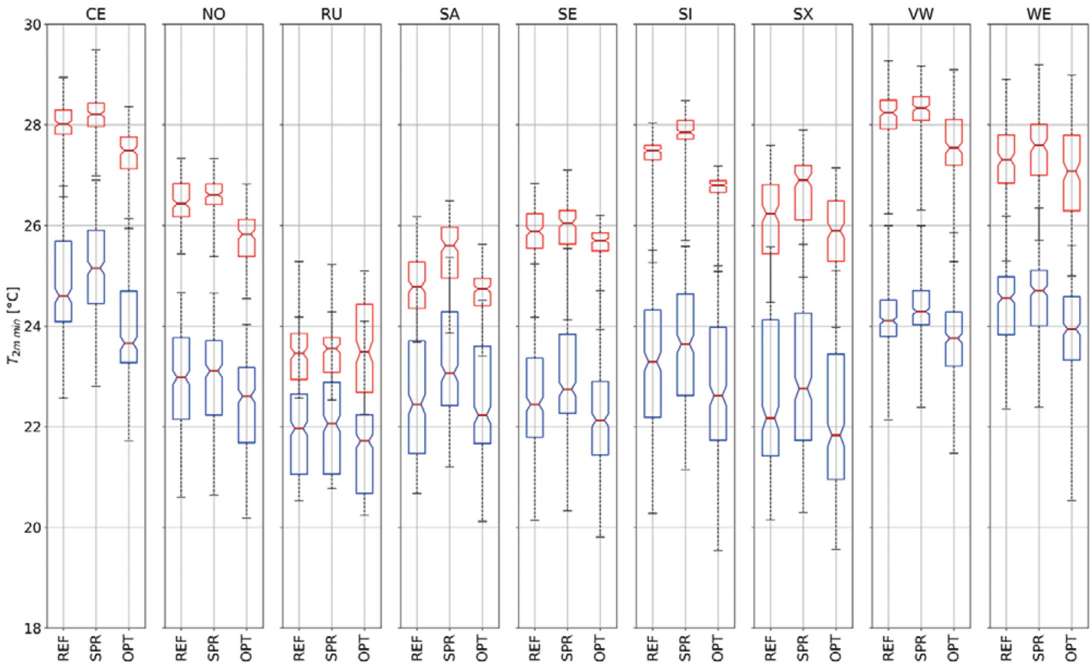

Figure 5 and 6: 2 m air temperature for the selected cloud free days of the chosen climate episode for present (hw15yACT, blue) and future (hw15ySCE, red) and the 3 different urban development scenarios (sh. Table 1) for daily maximum temperature (above) and daily minimum temperature (below) in the 9 different subregions (Fig. 3): Central Districts (CE), North-Rim (NO), New development areas: Seestadt Aspern (SA), South-eastern rim (SE), South-industrial (SI), South expansion (SX), Valley of Wien (VW), West – elevated low density residential (WE), Rural area (RU).

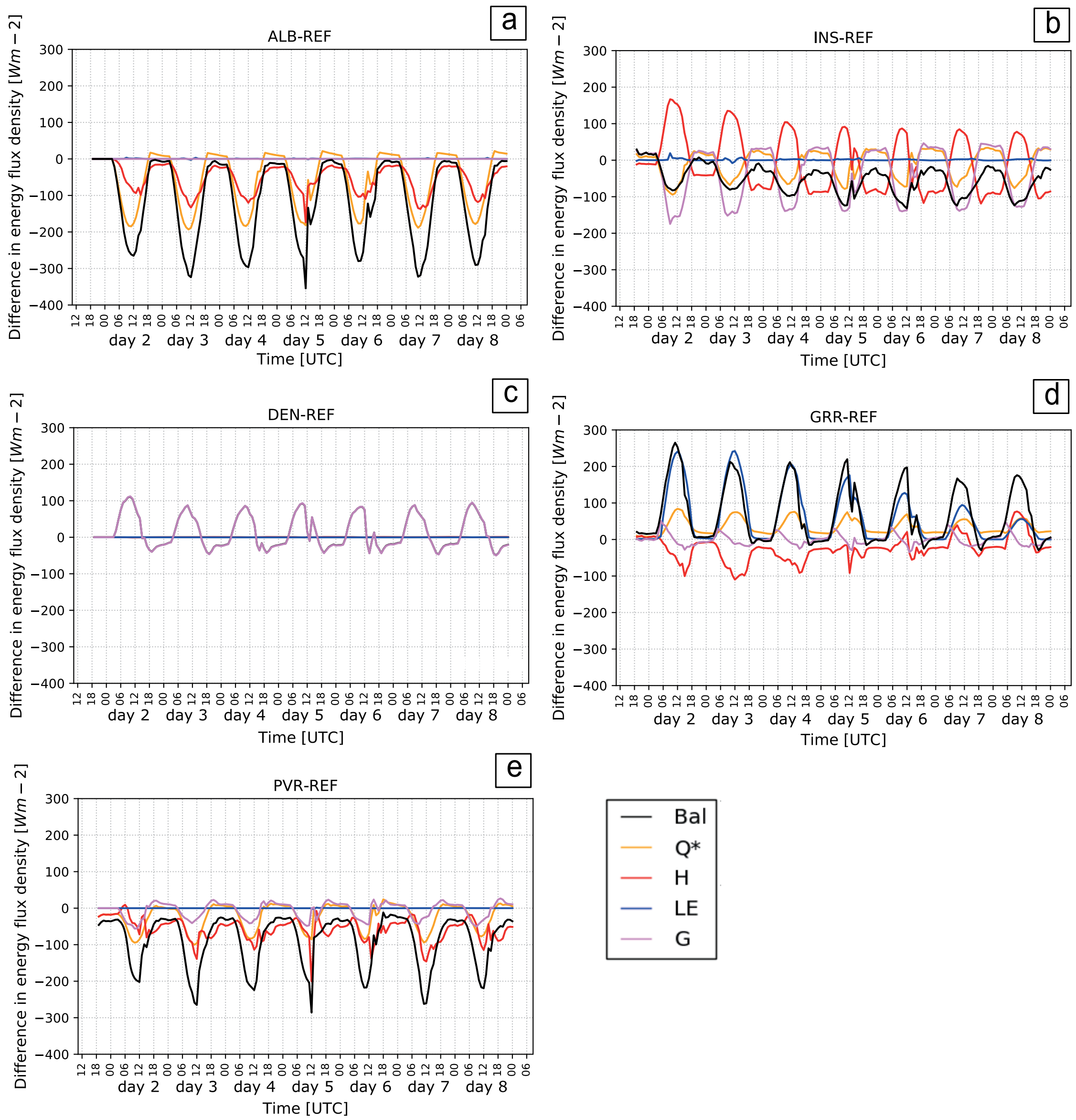

Figure 7: Timeseries differences compared to reference (REF) of radiation balance (Q*), sensible (H), latent (LE) (positive downwards), ground (G) heat flux and energy balance (Bal) during the hw15ySCE in the Central Districts (CE) for different measures: ALB (increased albedo), INS (insulation), DEN (density), GRR (green roof) and PVR (photovoltaic roof)

and decreased at night up to 3 K (Fig. 9b) for CE. On average this is an increase of 5 K (Table 4c) for CE. Both the daily maxima and minima of both variables show a declining trend for CE (Fig. 9b).

3.3.2 Canyon air temperature

For SPR the maximum canyon air temperature increases by 0.2 K (Table 5b) in the central districts (CE). For OPT, both the minimum and maximum canyon temperature decrease by 0.2 and 0.9 K in CE (Table 5b, 5c) respectively. In the new urbanized areas (SA) itself the maximum and minimum canyon temperature increase by 0.7 and 1.0 K for SPR. In the OPT scenario, the mean increase is only 0.5 K and 0.3 K in SA (Table 5b, 5c) while for the median of the 2 m air temperature calculated by WRF-TEB there is even a decrease (Fig. 5 and 6).

For ALB the canyon air temperature maxima and minima decrease by not more than 0.2 K and 0.1 K, respectively in all subregions (Table 5b, 5c). For INS

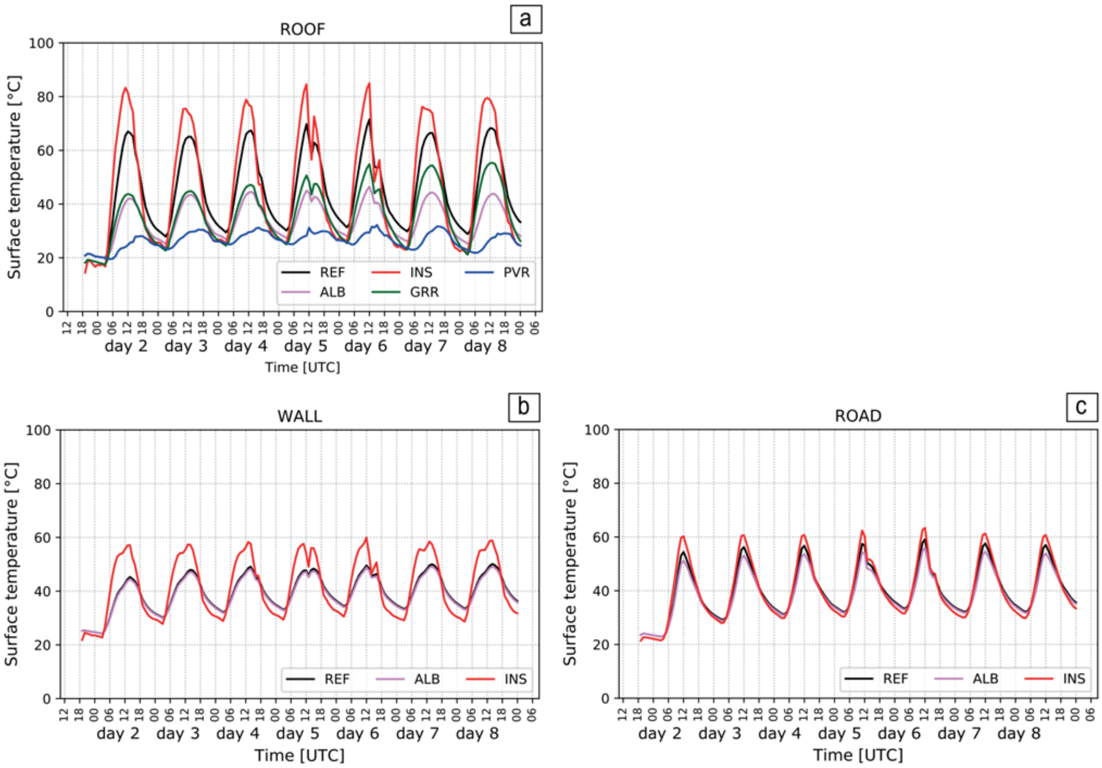

Figure 8: Time series of the surface temperature of roof (a), wall (b) and road (c) of the resilience measures where changes have been applied to these surfaces – during the future episode (hw15ySCE) for the Central Districts (CE).

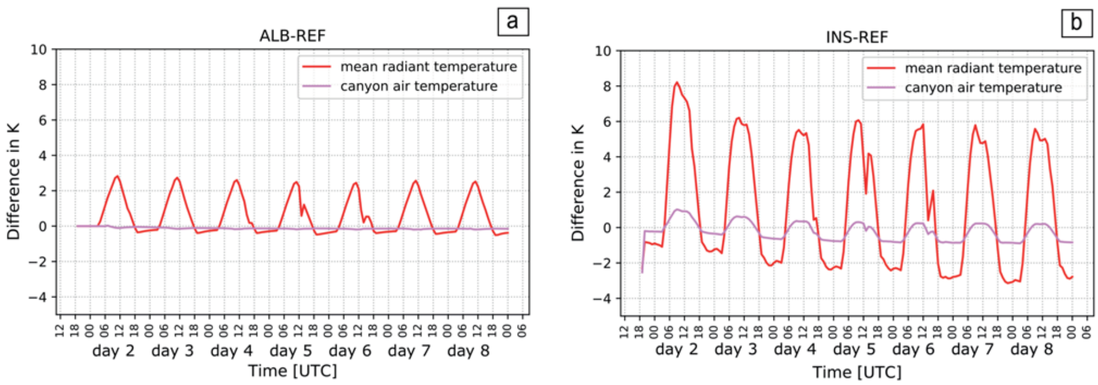

Figure 9: Difference of time series of two elements of UTCI, changed by the resilience measures: Mean radiant temperature in the shade and canyon air temperature during the future episode (hw15ySCE) for the Central Districts (CE).

the maximum canyon temperature does not increase by more than 0.1 K while the minimum canyon temperature decreases up to 0.8 K, where 0.8 K are only reached in the central districts (Table 5b, 5c). For DEN the changes for maximum and minimum canyon air temperature are below 0.1 K in all subregions (Table 5b, 5c). For GRR both maximum and minimum canyon air temperature decrease by 0.1 K and 0.2 K, respectively, in CE and are lower in all other subregions (Table 5b, 5c). For PVR both maximum and minimum canyon air temperature decrease by 0.2 K and 0.2 K in CE and are lower in all other subregions (Table 5b, 5c), respectively.

Table 4: a) absolute maximum and minimum radiant temperature (MRT) values [°C] of the actual (hw15yACT – "ACT") and future heat wave (hw15ySCE – "SCE") of the reference run and differences [K] of b) maximum MRT in the sun c) maximum MRT in the shade and d) minimum MRT (shade = sun) to the reference run hw15ySCE for the cloud free days of the selected episode, for all urban scenarios and *resilience measures* spatial mean in the 9 different subregions (Fig. 3): Central Districts (CE), North-Rim (NO), New development areas: Seestadt Aspern (SA), South-eastern rim (SE), South-industrial (SI), South expansion (SX), Valley of Wien (VW), West – elevated low density residential (WE), Rural area (RU) – which is *only based on 4 values. Differences over +/−1 are marked red/blue.

a) MRT		CE	NO	RU*	SA	SE	SX	SI	VW	WE
REF ACT	Shade, max	47.8	50.8	50.4	51.9	50.9	51.3	51.0	50.5	50.7
REF ACT	Shade, min	27.5	23.6	20.2	23.2	22.3	22.6	23.2	24.1	24.7
REF ACT	Sun, max	73.2	75.9	75.2	76.5	75.8	76.2	76.1	75.6	24.8
REF SCE	Shade, max	54.4	56.6	54.2	57.07	56.0	55.1	55.4	55.8	56.1
REF SCE	Shade, min	30.9	25.9	21.1	25.16	24.2	24.6	25.8	27.3	27.4
REF SCE	Sun, max	80.8	82.4	80.6	82.73	81.9	81.4	81.7	81.9	82.1
b) maximum MRT in the sun, differences to REF (both: hw15ySCE)										
SPR		−0.1	−0.1	0.3	−0.9	0.1	0.3	0.2	0.0	0.0
OPT		0.6	0.2	0.5	−0.5	0.4	0.5	0.5	0.4	0.6
ALB		*1.9*	*1.5*	*1.6*	*1.4*	*1.5*	*1.6*	*1.6*	*1.6*	*1.6*
INS		*4.0*	*2.3*	*1.3*	*2.2*	*1.9*	*1.6*	*1.8*	*2.2*	*2.4*
DEN		*0.0*	*0.1*	*0.1*	*0.0*	*0.1*	*0.1*	*0.1*	*0.1*	*0.1*
GRR		*−0.1*	*−0.0*	*−0.0*	*−0.0*	*−0.0*	*−0.0*	*−0.0*	*−0.1*	*−0.1*
PVR		*−0.1*	*−0.1*	*−0.0*	*−0.1*	*−0.1*	*−0.1*	*−0.1*	*−0.1*	*−0.1*
c) maximum MRT in the shade, differences to REF (both: hw15ySCE)										
SPR		−0.1	−0.1	0.6	−1.3	0.1	0.5	0.3	0.1	0.1
OPT		0.3	−0.1	0.6	−1.1	0.2	0.4	0.6	0.3	0.50
ALB		*2.3*	*1.8*	*2.0*	*1.8*	*1.8*	*1.9*	*1.9*	*2.0*	*1.9*
INS		*5.0*	*3.0*	*1.7*	*2.8*	*2.6*	*2.0*	*2.3*	*2.8*	*3.0*
DEN		*0.0*	*0.1*	*0.1*	*0.0*	*0.1*	*0.1*	*0.1*	*0.1*	*0.1*
GRR		*−0.1*	*−0.1*	*−0.0*	*−0.1*	*−0.0*	*−0.0*	*−0.1*	*−0.1*	*−0.1*
PVR		*−0.2*	*−0.1*	*−0.0*	*−0.1*	*−0.1*	*−0.1*	*−0.1*	*−0.1*	*−0.1*
d) minimum MRT, differences to REF (both: hw15ySCE)										
SPR		0.0	0.2	0.1	2.2	0.1	0.8	0.1	0.1	0
OPT		−0.4	0.2	0.2	2.3	0.3	0.2	0.1	0.2	0.3
ALB		*−0.3*	*−0.3*	*−0.2*	*−0.2*	*−0.3*	*−0.3*	*−0.3*	*−0.3*	*−0.3*
INS		*−3.1*	*−2.6*	*−1.9*	*−2.6*	*−2.5*	*−2.5*	*−2.6*	*−2.6*	*−2.8*
DEN		*0.0*	*0.5*	*0.4*	*0.6*	*0.5*	*0.5*	*0.5*	*0.5*	*0.5*
GRR		*−0.2*	*−0.1*	*−0.1*	*−0.1*	*−0.1*	*−0.1*	*−0.1*	*−0.1*	*−0.1*
PVR		*−0.2*	*−0.1*	*−0.1*	*−0.1*	*−0.1*	*−0.1*	*−0.1*	*−0.1*	*−0.1*

3.3.3 Universal Thermal Comfort Index (UTCI)

Both MRT and canyon air temperature influence the magnitude of UTCI. Here, mainly UTCI shade is used. The maximum future UTCI in the sun for hw15ySCE is included as reference in Table 6e. Values of 51.0 °C in the central districts (CE) and 49.6 °C in the rural region (RU) are extremely heat stressed (Bröde et al., 2012), so that we did not think it feasible to reduce it to a comfortable range by applying resilience measures. Between the present (hw15yACT) and future (hw15ySCE) heat wave there is already an increase of 5.3–6.3 K for the absolute maximum UTCI shade averaged over the different subregions (Table 6a). The absolute minimum UTCI changes least in the rural areas, but within the urban areas can increase up to 3 K (Table 6c).

Compared to the reference scenario (REF), in the urban sprawl scenario (SPR), the UTCI increases excluding SA (maximum UTCI by less than 0.1, minimum UTCI by up to 0.4), whereas in the optimized urban development scenario (OPT), the UTCI is reduced (maximum by up to 0.2 K, and the minimum by up to 0.7 K) in most areas. The largest differences are simulated in the new development areas (SA) where new urban districts are constructed on formerly unbuilt land (Table 6b, 6d). Here also in the OPT scenario there are increases of maximum and minimum UTCI by 0.9 K and 0.4 K, respectively. In the SPR scenario in the new development areas (SA) the UTCI maximum increases by 0.6 K and the minimum by 1.3 K. Also, in other areas of potential spread of settlement area, especially the minimum UTCI is increased, e.g., in South expansion areas (SX) by 0.4 K (Table 6d).

For ALB the average daily maximum UTCI increases by 0.2 K, while the average daily minimum decreases by 0.1 K in CE (Table 6b, 6d). For INS the daily maximum UTCI increases by 1.2 K, while the daily minimum decreases by 1.2 K in CE (Table 6b, 6d).

Table 5: a) absolute maximum and minimum canyon air temperature values [°C] of the future heat wave (hw15ySCE) for the reference run. b) differences [K] for the maximum canyon air temperature and c) differences [K] for the minimum canyon air temperature to the reference run hw15ySCE. average values for the cloud free days of the selected episode for all urban scenarios and *resilience measures* spatial mean in the 9 different subregions (Fig. 3): Central Districts (CE), North-Rim (NO), New development areas: Seestadt Aspern (SA), South-eastern rim (SE), South-industrial (SI), South expansion (SX), Valley of Wien (VW), West – elevated low density residential (WE), Rural area (RU) – which is *only based on 4 values. Differences over +/−0 0.25 are marked red/blue.

a) canyon air temperature	CE	NO	RU*	SA	SE	SX	SI	VW	WE
REF max	43.8	42.6	42.2	42.3	42.3	42.2	42.1	42.3	42.1
REF min	29.9	27.4	24.2	25.9	26.5	27.5	28.3	29.3	28.2
b) maximum canyon air temperature, differences to REF (both: hw15ySCE)									
SPR max	−0.0	−0.0	−0.0	0.7	0.1	0.1	−0.0	0	0.0
OPT max	−0.2	−0.1	−0.3	0.5	0.1	−0.2	−0.1	−0.2	−0.1
ALB max	*−0.2*	*−0.1*	*−0.1*	*−0.1*	*−0.1*	*−0.1*	*−0.2*	*−0.1*	*−0.1*
ISO max	*0.1*	*0.1*	*0.0*	*0.1*	*0.1*	*0.1*	*0.0*	*0.1*	*0.1*
DEN max	*0*	*0.0*	*−0.0*	*0.0*	*0.0*	*0.0*	*0.1*	*0.0*	*0.1*
GRR max	*−0.1*	*−0.0*	*−0.0*	*−0.0*	*−0.0*	*−0.0*	*−0.0*	*−0.0*	*−0.1*
PVR max	*−0.2*	*−0.1*	*−0.0*	*−0.0*	*−0.1*	*−0.1*	*−0.0*	*−0.1*	*−0.1*
c) minimum canyon air temperature, differences to REF (both: hw15ySCE)									
SPR min	0.2	0.3	0.2	1.0	0.0	0.3	0.3	0.1	0.2
OPT min	−0.9	−0.8	−0.1	0.3	−0.1	−0.3	−0.7	−0.8	−0.5
ALB min	*−0.1*	*−0.1*	*−0.1*	*−0.1*	*−0.1*	*−0.1*	*−0.1*	*−0.1*	*−0.1*
ISO min	*−0.8*	*−0.3*	*−0.0*	*−0.3*	*−0.3*	*−0.3*	*−0.3*	*−0.3*	*−0.3*
DEN min	*0.0*	*0.1*	*0.1*	*0.1*	*0.1*	*0.1*	*0.1*	*0.1*	*0.0*
GRR min	*−0.2*	*−0.1*	*−0.1*	*−0.1*	*−0.1*	*−0.0*	*−0.1*	*−0.1*	*−0.1*
PVR min	*−0.2*	*−0.1*	*−0.1*	*−0.1*	*−0.1*	*−0.1*	*−0.1*	*−0.1*	*−0.1*

For DEN the changes of UTCI of both maxima and minima are below 0.1 K on average in the central districts, where no densification takes place. In the densified districts with widespread commercial/industrial areas (SE, SI and NO), canyon air temperature is increasing, but changes are still below 0.1 K. The daily maximum UTCI increases only below 0.1 K whereas the daily minimum UTCI increases by 0.2 K (Table 6b, 6d). For GRR the daily maximum UTCI decreases by 0.1 K whereas the daily minimum UTCI decreases by 0.2 K (Table 6b, 6d) in CE. For PVR the daily maximum UTCI decreases by 0.2 K and the daily minimum UTCI by 0.2 K (Table 6b, 6d) in CE.

Most scenarios show a significant difference to the reference in their extreme values with $p \ll 0.05$ using the T-Test for related samples in the central districts. Only SPR does not show a significant difference in minima and maxima UTCI when the central districts are compared.

4 Discussion

4.1 Global climate change and influence on the Vienna region

4.1.1 Air temperature (T_{max} and T_{min}):

The lateral boundary conditions of the future heat wave are taken from regional climate scenarios, which are based on the global model GFDL-CM3 (Donner et al., 2011) forced with the RCP8.5 emission. The air temperature calculated for the selected 9 km^2 subregions of Vienna using 3 nests in this study increases by up to 7 K for the T_{max} and 2 to 4 K for the T_{min} values from the heat waves hw15y2015ACT to hw15ySCE. This means that both heat waves have Kyselý days (Kyselý et al., 2000) and tropical nights (T_{min}>20 °C). This shows a strong increase in T_{max} for extreme heat waves compared to the mean annual air temperature increase of 3.5 K published by APCC (2014) and Gobiet et al. (2014), which also refers to A1B instead of the more extreme RCP8.5. For France increases of 6–13 K for different regions by 2100 have been projected by Bador et al. (2017). Seneviratne et al. (2018) found positive air temperature anomalies of 8 K for Central Europe for the 21st century. Soil moisture – temperature feedbacks after early and intensified depletion of root-zone soil moisture contribute significantly to the Central European strong increases in extreme temperature (Vidale et al., 2007; Vogel, 2018).

It is interesting to note that the projected increase in T_{max} (Fig. 5) is more than twice as strong as the increase projected for the mean annual temperature in Austria (3.5 K), while the T_{min} (Fig. 5) are projected to increase about the amount of the mean annual temperature. As a result, the daily temperature range is projected to increase. Such an increase in daily temperature range was also found by Cattiaux et al. (2015) and be could also be partly attributed to the decreasing surface evaporation due to soil moisture depletion in future European summers (Jasper et al., 2006). This also affects the ru-

Table 6: a) absolute maximum UTCI shade values [°C] of present (hw15yACT – cloud free days: 4, 5, 7, 8) and future (hw15ySCE – cloud free days: 7, 8) of the reference run followed by the difference [K] between the two heat waves and b) differences [K] to the reference run hw15ySCE average values for the cloud free days of the selected episode for all urban scenarios and *resilience measures* spatial mean in the 9 different subregions (Fig. 3): Central Districts (CE), North-Rim (NO), New development areas: Seestadt Aspern (SA), South-eastern rim (SE), South-industrial (SI), South expansion (SX), Valley of Wien (VW), West – elevated low density residential (WE), Rural area (RU). Differences over +/−0.5 are marked red/blue. c) and d) show the same for minimum UTCI shade, e) shows absolute maximum UTCI sun values for the hw15ySCE.

a) max UTCI shade	CE	NO	RU	SA	SE	SX	SI	VW	WE
hw15yACT	38.9	38.8	38.1	38.2	38.2	38.3	38.7	38.6	38.3
hw15ySCE	45.2	44.4	43.9	44.2	44.2	43.7	44.0	44.1	44.0
hw15ySCE-hw15yACT	6.3	5.6	5.8	5.6	6.0	5.4	5.3	5.5	5.7
b) max UTCI shade, differences to REF (both: hw15ySCE)									
SPR max	0.0	0.0	0.1	0.6	−0.1	0.1	−0.2	0.1	−0.0
OPT max	−0.1	−0.1	−0.0	0.4	−0.1	−0.0	−0.2	−0.1	0.2
ALB max	*0.2*	*0.3*	*0.2*	*0.3*	*0.3*	*0.3*	*0.3*	*0.3*	*0.3*
INS max	*1.2*	*0.8*	*0.3*	*0.6*	*0.6*	*0.5*	*0.5*	*0.7*	*0.7*
DEN max	*0.0*	*0.0*	*0.0*	*0.1*	*0.0*	*0.0*	*0.1*	*0.1*	*0.1*
GRR max	*−0.1*	*−0.0*	*0.5*	*0.1*	*−0.0*	*−0.0*	*−0.1*	*−0.0*	*−0.0*
PVR max	*−0.2*	*−0.1*	*0.5*	*0.0*	*−0.1*	*−0.0*	*−0.1*	*−0.1*	*−0.1*
c) min UTCI shade	CE	NO	RU	SA	SE	SX	SI	VW	WE
hw15yACT	26.6	23.5	21.7	23.3	22.0	23.1	23.9	24.4	25.3
hw15ySCE	28.8	25.8	22.1	24.5	24.9	25.4	26.4	27.4	26.9
hw15ySCE-hw15yACT	2.2	2.3	0.4	1.2	2.9	2.3	2.5	3.0	1.6
d) minimum UTCI shade, differences to REF (both: hw15ySCE)									
SPR min	0.2	0.3	0.3	1.3	0.0	0.4	0.2	0.1	−0.1
OPT min	−0.7	−0.5	0.1	0.9	0	−0.3	−0.6	−0.6	−0.4
ALB min	*−0.1*	*−0.1*	*−0.0*	*−0.0*	*−0.0*	*−0.1*	*−0.1*	*−0.1*	*−0.1*
INS min	*−1.2*	*−0.9*	*−0.8*	*−1.0*	*−0.7*	*−0.9*	*−0.8*	*−1.0*	*−0.8*
DEN min	*0.0*	*0.2*	*0.2*	*0.2*	*0.2*	*0.2*	*0.2*	*0.2*	*0.2*
GRR min	*−0.2*	*−0.1*	*−0.1*	*−0.1*	*−0.1*	*−0.1*	*−0.1*	*−0.1*	*−0.1*
PVR min	*−0.2*	*−0.1*	*−0.1*	*−0.1*	*−0.1*	*−0.1*	*−0.1*	*−0.1*	*−0.1*
e) maximum UTCI sun, absolute values									
hw15ySCE	51.0	50.3	49.5	50.0	50.0	49.4	49.7	49.8	49.8

ral surroundings, which are even more affected by reduced soil moisture than urban areas with high sealing fractions. Dryer soils have a lower heat capacity and can cool more strongly than wetter soils. Also, in this study a decrease of soil moisture was simulated (Figure D-5). This can explain the high values of T_{max} in the rural subregion during day but also the low values of T_{min} during night, thus this could be the reason of the increase of the future nocturnal urban-rural difference.

The nocturnal canopy UHI is expected to increase from 3 to 4.6 K which is caused rather by the lower increase of minimum temperatures in the rural areas than within the city.

The actual and future UHI is strongly dominated by the mesoscale thermal regime and especially the future UHI is affected by high temperature reinforced by dry fields in the surroundings, which is a known process during heat waves (Fischer and Seneviratne, 2007; Hartmann, 1994). Fischer and Seneviratne (2007) analyzed the interactions between soil moisture and atmosphere for the 2003 summer heat wave in Europe and found that precipitation deficits, early vegetation growth and positive radiation anomalies preceding the heat wave contributed to rapid loss of soil moisture. Zampieri et al. (2009) showed that drought in the Mediterranean region can favour heat waves conditions in Europe at a continental scale by change in atmospheric circulation and hot air mass advection. This would suggest, that soil moisture deficits ought to be reduced by suitable methods on a continent-scale rather than only regional scale. Duchez et al. (2016) and Kornhuber et al. (2017) name a stationary jet stream position, caused by global scale circulation patterns, that coincides with observed European temperature extremes, including the 2015 event.

4.1.2 Thermal comfort index UTCI

The Universal Thermal Climate Index (UTCI) is used by meteorological services to quantify outdoor human thermal comfort and has been included in TEB to provide standardized information about human thermal comfort for grid resolutions > 100 m and with highly parameterized building morphology. It takes into account whole body thermal effects thanks to a multi-node thermophysiological model. It is derived by the air temperature, water vapour pressure and MRT, which is a quantity that describes the shortwave and longwave radiation balance of the human body at 2 m and wind speed at 10 m height (Jendritzky et al., 2012; Weihs et al., 2012). In this study first WRF-TEB uses the different urban roughness of the three used building morphologies to calculate a 10 m wind, which is 10 m above the mean building height – so around 30 m agl in the city centre. Within the UTCI calculation a 6th order polynomial is used that assumes a uniform roughness length of 0.01 and a logarithmic profile, which reduces the 10 m wind to 70 % at 1.3 m. Although the roughness length is low this attenuation is very similar to the attenuation between above roof and within canyon wind speeds presented in Erell et al. (2011), which is based on Pearlmutter et al. (2005). They found an attenuation of around 60 % and 70 % caused by street canyons of a height/width ratio 0.66 and 1.0, as they are common in the Viennese city structure, which varies +/−10 % dependent on the wind direction or 'angle of attack'. The influence of the low roughness was further calculated by first applying the Hellman's exponential law (Urban and Kysely, 2014; Ketterer et al., 2017) with the maximum roughness assumed for Vienna (z0 = 2) to calculate a more realistic reduction of wind speed from the 10 m level to 1.3 agl. Using this second approach the average wind speeds occurring in heat waves analysed in this study of 2.2 m/s were reduced to 0.3 m/s. Then the 10 m wind was recalculated with the agreed UTCI logarithmic profile and a z0 of 0.01. For the future heat wave situation of an air temperature of 40 °C, an MRT shade of 50 °C, an average water vapour pressure of 13.5 hPa, this change in wind speed results in a UTCI change of 0.3 K during the period of maximum MRT. For water vapour pressure of 20 hPa the change is only 0.1 K UTCI.

A recent comparison has been done by Zare et al., 2018, which shows that UTCI and PET are highly correlated. Urban and Kysely (2014) found for two regions in Bohemia that the simplification and underestimation of urban roughness only affects the prediction during cold spells, while PET and UTCI are both suitable to predict thermal discomfort during heat waves.

The maximum UTCI changes during extreme heat waves projected for the climate period 2050 from strong (32–38 °C UTCI) to very strong (38–46 °C UTCI) heat stress. This goes with other studies regarding future human thermal comfort. For example, Muthers et al. (2010) projected that even heat-related mortality could increase up to 129 % in Vienna until the end of the century, if no adaptation takes place. Matzarakis and Endler (2010) showed for Freiburg an increase of days with heat stress (PET>35 °C) in the order of 5 % (from 9.2 % for 1961–1990) per year.

4.2 City scale urban scenarios

4.2.1 Urban sprawl scenario

Urban sprawl of the Viennese agglomeration affects urban energy fluxes and temperature mainly in areas where new urban fabric is constructed on formerly vegetated areas. The sensible heat flux increases by up to +400 W/m^2 (not shown in the Figures), T_{min} by 1 K and the daily minimum UTCI by 1.3 K. No significant differences are simulated in the central districts, and no significant influence on the nocturnal UHI was found.

Kohler et al. (2017) presented a similar study for the Strasbourg–Kehl urban region (France–Germany). They conclude that under realistic assumptions urban sprawl until the year 2030 will not affect the UHI intensity significantly. Significant warming was only observed at atmospheric grid cells for which the urban fraction was increased more than 20 % compared to the initial case.

4.2.2 Optimized urban scenario

The optimized urban development scenario (OPT), which includes densification, slightly reduces air temperatures during the day, but clearly reduces them at night by 0.9 K. This leads to a slight reduction of nocturnal UHI by about 0.5 K. Also, the daily minimum UTCI is reduced by up to 0.7 K. The changed material properties can therefore counteract the negative effects of densification, which shows that the existing densification strategy of the city of Vienna (MA 18 (2014a+b) is promising. Salamanca et al. (2012) simulated a reduction of 1–2 K in UHI by assuming high albedo roofs and increased insulation for Madrid using WRF. Also, in their study the reduction of the heat ejected by air conditioning systems is mentioned as an important factor.

4.3 Local resilience measures

No coupled WRF-TEB simulations have been made for the quantification of the effect of single resilience measures. For this reason, the meteorological parameters above the urban canopy layer from the REF simulation has been used as forcing for offline simulations with SURFEX. With this modelling approach, the potential modification of the meteorological parameters above the urban canopy layer is not considered, and only the local effects can be seen, as if the rest of the city would still be built as REF. This part of the analysis shows what effects are to be expected locally if certain measures are not realized on a city scale but only on a local scale.

4.3.1 Albedo increase (ALB)

Increase of albedo is widely discussed as a cheap and effective measure to mitigate urban heat during summer heat episodes. e.g., Rafael et al. (2016) simulated using the WRF-SUEWS modelling system and roofs with an albedo of 80 % for Porto (Portugal) a maximum reduction in sensible heat flux of 62.8 W/m^2. Ramamurthy et al. (2015) showed that the wintertime penalty of white roofs, also for cool climates with 5 times more heating degree days than cooling degree days is insignificant compared to the summertime benefits. Žuvela-Aloise et al. (2018) simulated using MUKLIMO for Vienna a reduction of up to 6 summer days when assuming a roof albedo of 70 %. In many cities this measure is widely discussed, e.g., Los Angeles (https://albedomap.lbl.gov/) or even has already been implemented (https://www.coolrooftoolkit.org/knowledgebase/white-roofs-in-brooklyn-new-york/). In Vienna itself there are no real life examples so far and potential legal difficulties and hindrances to implement bright roofs are yet unknown.

For street canyons, Weihs et al. (2018) found that wall albedo increases from 0.1 to 0.2 during periods of high solar irradiation in a canyon of height/width ratio 1 can reduce air temperature in the canyon by about 1 K, dependent on the canyon geometry and reduce UTCI by about the same value. Schrijvers et al. (2016) found a reduction in canyon air temperatures as well, and an increase of UTCI for high albedo values. For a height/width ratio of 0.5 Schrijvers et al. (2016) recommend a uniform albedo of 0.2, while for height/width ratio 1 they recommend a gradient from high albedo close to the roof to low albedo on the ground. Lee and Mayer (2018) found that during heat wave conditions also starting for low albedo values there is a positive linear relationship between albedo increases (0.2–0.8) within the canyon and the human thermal comfort index PET. Also, in this study the ALB scenario shows an increase in the UTCI human thermal comfort index. Therefore, only increases in roof albedo, not within the canyon are recommended.

4.3.2 Decreased thermal conductivity of urban materials (INS)

Increasing the albedo of a very low insulation roof from 0.05 to 0.75 is roughly equivalent to adding 14 cm of insulation thickness (Ramamurthy et al., 2015). While it is a challenge to maintain the reflective properties of a white roof, insulations have longer lasting effects (Ramamurthy et al., 2015). Roman et al. (2016) found that increasing insulation results in an increase in sensible heat flux and surface temperatures during the day and a reduction at night. Here the same patterns are found. Increases of daily maximum as well as decreases of minimum air temperature and UTCI of about 1 °C/1 K caused by insulation was found by Weihs et al. (2018) for historical climate. In this study, the daily maximum UTCI increases by more than 1.2 °C for a future heat wave with a 15 year return period. This is a clear negative effect of such a measure during daytime. However, the analysis of the energy fluxes during the heat wave shows that the longer the heat wave persists, the more the positive effects of building insulation prevail. Decreased thermal conductivity due to better building insulation is currently being adopted in widespread fashion in Vienna mainly to reduce the need for heating and reduce green house gas emissions during winter.

4.3.3 Increased building density (DEN)

Increase in building density within feasible ranges in Vienna has only limited effect on the sensible heat flux (an increase of 10 W/m^2 is simulated) and leads to a slight increase of the daily minimum UTCI (0.2 K) and maximum UTCI (up to 0.1 K). In the present study increasing height of buildings is not considered, as those are still restricted and there is still enough attic space to be developed and changes in building height are still low. Beyond 2050 it is possible that the building height will further increase and lead to a densification and could cause a damping of the diurnal air temperature and increased nocturnal temperatures (Coutts et al., 2007) caused by the reduced sky view. Without improving insulation this is likely to lead to an increase in mean air temperature and intensified UHI (Rad et al., 2017).

4.3.4 Evaporation of vegetation surfaces (GRR)

De Munck et al. (2018) found that green roofs have nearly no influence on street level air temperature, but are a good strategy to reduce energy consumption all year round. The evaporative cooling is strongly dependent on available soil moisture. Also, in this study the changes caused in the air canyon are marginal. The roof temperatures on the other hand are reduced by over 10 K. Also, here it could be seen, that the cooling potential of green roofs decline towards the end of the heat wave as latent heat flux goes down (Fig. 7d).

The maximum cooling generated during heat wave conditions caused by evapotranspiration of vegetation (not shading) within the city modelled by De Munck et al. (2018) varied between 0.5 and 2 K. The influence in terms of additional humidity caused by urban vegetation appears tolerable in comparison to the benefits. Additional water vapour pressure caused by forest vegetation compared to an open site in Oxford (UK) was quantified by Morecroft et al. (1998) to be below 2 hPa. As an extreme scenario Mahmood et al. (2008) could show that the influence of irrigation of agricultural fields during a long term measurement series increases the average near ground dew point temperature during growing season by 1.56 K in the North American Great Plains. Apart from this, the water vapour pressure of cities can also exceed the rural values due to different reasons (Kuttler et al., 2007). Maximum differences of 5 hPa between urban and rural (agricultural) areas were found by Fortuniak et al. (2006) for Łodz (Poland).

4.3.5 Photovoltaic panels on roofs (PVR)

The use of photovoltaic panels on roofs shows a slight reduction of temperature and thermal stress, which is in correspondence with findings from Masson et al. (2014), who found that solar panels can reduce the UHI by 0.2 K during day and 0.3 K at night. Weihs et al. (2018) found that photovoltaic used on roofs could lead to a temperature reduction of 1.5 K and a reduction of UTCI of 1.5 K. Therefore, this article encourages the use of photovoltaic on roofs within the city.

4.3.6 Shade and urban trees

(Tree) shade is a fundamental method to reduce mean radiant temperature (MRT) and thus improve human thermal comfort during clear sky conditions. Although we do not take into account the influence of tree shade on wall, road and canyon temperatures, we demonstrate the main influence of tree shade, which is the reduced direct radiation, by presenting the MRT in the sun and shade. So, the shade caused by buildings in this study can serve as a proxy for the influence of tree shade. By now tree shade has been implemented in one fork of TEB by Redon et al. (2017), but the code is not implemented in the main code tree yet. Wang et al. (2018) simulated the effect of radiative cooling (not evapotranspiration) of trees in the built environment of contiguous United States and found an average decrease in near surface air temperatures of 3.06 K. They show that not only do trees reduce incoming solar radiation during daytime they also increase radiative cooling at night. The ground heat flux is reduced in intensity in the shaded areas. Although the sensible heat flux is increased at night, it is strongly reduced during daytime. Matzarakis and Endler (2010) could show that by reducing global radiation by assuming tree shade in urban areas the number of days with heat stress could be reduced by more than 10 % in Freiburg. Ketterer and Matzarakis (2015) increased the number of trees in an area in Stuttgart and found a decrease in PET by 0.5 K at 22:00 CET but by maximum 27 K at 14:00 CET. Also, in this study we found a decrease of 26 K between the maximum MRT in the sun and in the shade.

The vitality of urban trees declined drastically over the last 3–4 decades (Bradshaw et al., 1995) and trees in Viennese parks (Drlik, 2010) and some species used in Viennese streets (Schimann, 2015; Neuwirth, 2015) and cities close to Vienna (Zeiler, 2015) are documented to be under stress due to multiple stressors including summer heat waves and there is likely to be a low shade transition phase between our historical tree stock dying and new more tolerant trees being planted and growing to a state where they can provide perceptible shade.

Generally urban green infrastructure improves air quality (Abhijith et al., 2017). Only in urban canyons air pollution can deteriorate (Abhijith et al., 2017), which can be avoided by reducing emissions.

5 Conclusions and Outlook

- We coupled WRF and TEB to simulate two urban development scenarios of Vienna, which are presented here, for two heat waves representative for present and future climatic conditions of the mid-21st century. Further extreme changes in building material parameters have been done to estimate the potential to reduce air temperatures and maintain human thermal comfort by altering buildings themselves.
- Global and regional climate change subject to the RCP8.5 scenario causes an increase in the mean daily maximum air temperature in Vienna by 7 K. The mean daily minimum air temperature will increase by 2–4 K. This increase is stronger than the global average. One important factor may be low soil water content in the agricultural region Northeast to Southeast of Vienna. This increase needs to be mitigated on a global level by reducing the emission of green house gases, but also land use on the regional level is of importance.
- City scale changes caused by urban growth or densification, which will mainly affect air temperature and human thermal comfort locally at the place where new urbanisation takes place and not to a significant degree in the central districts. Using a combination of adoption of nearly zero-energy building standard, as demanded by the European Union under the Energy Performance of Buildings Directive and increasing albedo of building materials on city scale, a maximum reduction of urban canyon temperature achieved by changes in urban parameters of 0.9 K for the minima and 0.2 K for the maxima is accomplished. The effects on human thermal comfort are even smaller with 0.7 K UTCI and 0.1 K UTCI respectively.
- Local scale changes of different adaptation measures show, that insulation of buildings used alone increases the maximum wall surface temperatures by more than 10 K or the maximum MRT in the canyon by 5 K.
- Therefore, measures to reduce MRT within the urban canyon preferably by tree shade, which was not possible to include in this study, are expected to complement the proposed measures and are urgently recommended.

This study concludes that the rising air temperatures expected by climate change puts an unprecedented heat burden on the Viennese inhabitants, which cannot easily be reduced by measures concerning buildings within the city itself. Therefore, in addition to those measures, small scale measures such as planting trees to provide shade, water sensitive planning in the agricultural plains surrounding Vienna and global measures such as the reduction of greenhouse gas emissions in order to reduce temperature extremes are required.

Acknowledgements

This research was mainly done within the project URBANIA (ACRP 8th call: KR14AC7K11944) funded by the Klima und Energiefond (KliEN). The finalization of the manuscript was done during a stay at NILU, Norway funded by the Marietta Blau scholarship of OeAD. We would like to thank Jürgen Preiss, the MA 18 and Beatrix Gasienica-Wawrytko for their feedback and comments. Finally, we want to thank the two reviewers who helped to improve the manuscript.

References

Abhijith, K.V., P. Kumar, J. Gallagher, A. McNabola, R. Baldauf, F. Pilla, B. Broderick, S. Di Sabatino, B. Pulvirenti, 2017: Air Pollution Abatement Performances of Green Infrastructure in Open Road and Built-up Street Canyon Environments – A Review. – Atmos. Env. **162**, 71–86 DOI:10.1016/j.atmosenv.2017.05.014.

Amtmann, M., N. Altmann-Mavaddat, 2014: Eine Typology österreichischer Wohngebäude. (in German) – Österreichische Energieagentur. – Austrian Energy Agency, TABULA/EPISCOPE, http://episcope.eu/fileadmin/tabula/public/docs/brochure/AT_TABULA_TypologyBrochure_AEA.pdf (last access: 05.08.2019).

APCC, 2014: Österreichischer Sachstandsbericht Klimawandel 2014 (AAR14). – Kromp-Kolb, H., N. Nakicenovic, K. Steininger, A. Gobiet, H. Formayer, A. Köppl, F. Prettenthaler, J. Stötter, J. Schneider, Verlag der Österreichischen Akademie der Wissenschaften, Wien, Österreich, 1096 pp.

Arnold, D., I. Schicker, P. Seibert, 2011: Towards high-resolution environmental modelling in the Alpine region. – In: Air Pollution Modeling and its Application XXI. 269–273, Springer.

Auer, I., U. Foelsche, R. Böhm, B. Chimani, L. Haimberger, H. Kerschner, K.A. Koinig, K. Nicolussi, C. Spötl, 2014: Vergangene Klimaänderung in Österreich, In: Österreichischer Sachstandsbericht Klimawandel 2014 (AAR14). – Austrian Panel on Climate Change (APCC), Verlag der Österreichischen Akademie der Wissenschaften, Wien, Österreich, 227–300.

Bador, M., L. Terray, J. Boé, S. Somot, A. Alias, A-L. Gibelin, B. Dubuisson, 2017: Future Summer Mega-Heatwave and Record-Breaking Temperatures in a Warmer France Climate. – Env. Res. Lett. **12**, 074025, 12, DOI:10.1088/1748-9326/aa751c.

Bardow, A., D. Green, 2018: Low-Carbon Process Industries Through Energy Efficiency and Carbon Dioxide Utilisation, European Commission – Directorate-General for Research and Innovation, https://publications.europa.eu/en/publication-detail/-/publication/df9afa95-025d-11e8-b8f5-01aa75ed71a1/language-en (last access: 05.06.2019).

Berger, T., H. Formayer, R. Smutny, C. Neururer, R. Passawa, 2012: Auswirkungen des Klimawandelsauf den thermischen Komfort in Bürogebäuden (in German). – Berichte aus Energie- und Umweltforschung 7/2012, Bundesministerium für Verkehr, Innovation und Technologie, https://www.nachhaltigwirtschaften.at/resources/hdz_pdf/endbericht_1207_thermischer_komfort.pdf (last access 05.09.2012).

Boone, A., P. Samuelsson, S. Gollvik, A. Napoly L. Jarlan, E. Brun, B. Decharme, 2017: The interactions between atmosphere land surface model with a multi-energy balance (ISBA-MEB) option in SURFEXv8 Part 1: Model description. – Geosci. Model Develop. **10**, 843–872 DOI:10.5194/gmd-10-843-2017.

Bornstein, R., Q. Lin, 2000: Urban heat islands and summertime convective thunderstorms in Atlanta: Three case studies. – Atmos. Env. **34**, 507–516.

Bradshaw, A., B. Hunt, T. Walmsley, 1995: Trees in the Urban Landscape: Principles and Practice. – NY:E&FNSpon, London, NewYork,.

Bröde, P., D. Fiala, K. Blazejcyk, I. Holmér, G. Jendritzky, B. Kampmann, B. Tinz, G. Havenith, 2012: Deriving the operational procedure for the universal thermal climate index (utci). – Int. J. Biometeorol. **56**, 481–494.

Bueno, B., G. Pigeon, L.K. Norford, K. Zibouche, C. Marachadier, 2012: Development and evaluation of a building energy model integrated in the TEB scheme. – Geosci. Model Develop. **5**, 433–448 DOI:10.5194/gmd-5-433-2012.

Bundesministerium für Nachhaltigkeit und Tourismus (BMNT), 2016: Endbericht ÖKS15 – Klimaszenarien für Österreich, Daten – Methoden – Klimaanalyse. – Zentralanstalt für Meteorologie und Geodynamik (ZAMG), Wegener Center für Klima und globalen Wandel (WEGC) und dem Interfakultären Fachbereich Geoinformatik der Universität Salzburg (Z_GIS), https://www.bmnt.gv.at/umwelt/klimaschutz/klimapolitik_national/anpassungsstrategie/klimaszenarien.html (last access: 20.05.2019).

Cattiaux, J., H. Douville, R. Schoetter, S. Parey, P. Yiou, 2015: Projected increase in diurnal and interdiurnal variations of European summer temperatures. – Geophys. Res. Lett. **42**, 899–907 DOI:10.1002/2014GL062531.

Cordeau, E. , 2016: Les îlots morphologiques urbains (IMU) (in French). – IAU îdF, https://www.iau-idf.fr/fileadmin/NewEtudes/Etude_1270/Les_ilots_morphologiques_urbains.pdf (last access: 05.08.2019).

Coutts, A.M., J. Beringer, N.J. Tapper, 2007: Impact of Increasing Urban Density on Local Climate: Spatial and Temporal Variations in the Surface Energy Balance in Melbourne, Australia. – J. Appl. Meteor. Climatol. **46**, 477–493 DOI:10.1175/JAM2462.1.

de Munck, C.S., A. Lemonsu, R. Bouzouidja, V. Masson, R. Claverie, 2013: The GREENROOF module (v7.3) for modelling green roof hydrological and energetic performances within TEB. – Geosci. Model Develop. **6**, 1941–1960. DOI:10.5194/gmd-6-1941-2013.

de Munck, C.S., A. Lemonsu, V. Masson, J. Le Bras, M. Bonhomme, 2018: Evaluating the impacts of greening scenarios on thermal comfort and energy and water consumptions for adapting Paris city to climate change. – Urban Climate **23**, 260–286. DOI:10.1016/j.uclim.2017.01.003.

de Pee, A., D. Pinner, O. Roelofsen, K. Somers, E. Speelman, M. Witteveen, 2018: Decarbonization of industrial sectors: the next frontier. – McKinsey & Company, https://www.mckinsey.com/business-functions/sustainability/our-insights/how-industry-can-move-toward-a-low-carbon-future (last access: 05.06.2019).

Donner, L.J., B.L. Wyman, R.S. Hemler, L.W. Horowitz, Y. Ming, M. Zhao, J.-C. Golaz, P. Ginoux, S.J. Lin, M.D. Schwarzkopf, J. Austin, G. Alaka, W.F. Cooke, T.L. Delworth, S.M. Freidenreich, C.T. Gordon, S.M. Griffies, I.M. Held, W.J. Hurlin, S.A. Klein, T.R. Knutson, A.R. Langenhorst, H.-C. Lee, Y. Lin, B.I. Magi, S.L. Malyshev, P.C.D. Milly, V. Naik, M.J. Nath, R. Pincus, J.J. Ploshay, V. Ramaswamy, C.J. Seman, E. Shevliakova, J.J. Sirutis, W.F. Stern, R.J. Stouffer, R.J. Wilson, M. Winton, A.T. Wittenberg, F. Zeng, 2011: The Dynamical Core, Physical Parameterizations, and Basic Simulation Characteristics of the Atmospheric Component AM3 of the GFDL Global Coupled Model CM3. – Journal of Climate **24**, 13, 3484–3519.

Dou, Y. , 2014: The influence of urban planning on urban thermal comfort. – Master Thesis, Wageningen University, the Netherlands, https://www.wur.nl/upload_mm/8/f/f/a3db8019-a442-4270-9a43-d7e06e834169_Dou_Yuehan_THE_LUP80436_201407.pdf (last access: 2019.08.29).

Duchez, A., E. Frajka-Williams, S.A. Josey, D.G. Evans, J.P. Grist, R. Marsh, G.D. McCarthy, B. Sinha, D.I. Berry, J.J.M. Hirschi, 2016: Drivers of Exceptionally Cold North Atlantic Ocean Temperatures and Their Link to the

2015 European Heat Wave. – Environmental Research Letters, **11**, 7, 074004.

Drlik, S., 2010: Klimawandelanpassung der Pflege und Erhaltung öffentlicher Grünanlagen in Grossstädten unter Berücksichtigung des Konzepts der Nachhaltigen Entwicklung, untersucht am Fallbeispiel Wien. (in German) – Dissertation, https://zidapps.boku.ac.at/abstracts/download.php?dataset_id=7703&property_id=107 (last access: 11.10.2019).

EEA (European Environment Agency), 2012: Corine land cover data set 2012, https://www.eea.europe.eu/data-and-maps/data/clc-2012-raster (last access: 23.05.2018).

Erell, E., D. Pearlmutter, T. Williamson, 2011: Urban Microclimate – Designing the Spaces Between Buildings. – Earthscan, Washington, USA, 266 pp.

Fallmann, J., R. Forkel, S. Emeis, 2016: Secondary effects of urban heat island mitigation measures on air quality. – Atmos. Env. **125**, 199–211, DOI:10.1016/j.atmosenv.2015.10.094.

Fanger, P.O. , 1970: Thermal Comfort, Analysis and Applications in Environmental Engineering. – McGraw-Hill Company, US, 244 pp.

Fiala, D., K.J. Loma, M. Stohrer, 2001: Computer prediction of human thermoregulatory and temperature responses to a wide range of environmental conditions. – Int. J. Biometeorol. **45**, 143–159.

Fischer, E.M., S.I. Seneviratne, 2007: Soil Moisture – Atmosphere Interactions during the 2003 European Summer Heat Wave. – J. Clim., 20, 5081–5099, DOI:10.1175/JCLI4288.1.

Fisher, R., L. Tippett, 1928: Limiting forms of the frequency distributions of the largest or smallest member of a sample. – Proc Camb Philos Soc. **24**, 180–190.

Formayer, H., P. Haas., M. Hofstätter., S. Radanovics, H. Kromp-Kolb, 2007: Räumlich und zeitlich hochaufgelöste Temperaturszenarien für Wien und ausgewählte Analysen bezüglich Adaptionsstrategien. – Bericht im Auftrag der Wiener Umweltschutzabteilung – MA 22 der Stadt Wien gemeinsam mit der MA 27 – EU-Strategie und Wirtschaftsentwicklung, https://www.wien.gv.at/wirtschaft/standort/pdf/temperaturszenarien.pdf (last access: 05.08.2019).

Fortuniak, K., K. Klysik, J. Wibig, 2006: Urban–Rural Contrasts of Meteorological Parameters in Lódz. – Theor. Appl. Climatol. **84**, 91–101, DOI:10.1007/s00704-005-0147-y.

Gabriel, K.M.A., W.R. Endlicher, 2011: Urban and rural mortality rates during heat waves in Berlin and Brandenburg, Germany. – Env. Poll. **159**, 2044–2050.

Gobiet, A., S. Kotlarski, M. Beniston, G. Heinrich, J. Rajczak, M. Stoffel, 2014: 21st century climate change in the European Alps – A review. – Sci. Total Env. **493**, 1138–1151 DOI:10.1016/j.scitotenv.2013.07.050.

Grimmond, C.S. B, M. Roth, T.R. Oke, Y.C. Au, M. Best, R. Betts, G. Carmichael, H. Cleugh, W. Dabberdt, R. Emmanuel, E. Freitas, K. Fortuniak, S. Hanna, P. Klein, L.S. Kalkstein, C.H. Liu, A. Nickson, D. Pearlmutter, D. Sailor, J. Voogt, 2010: Climate and More Sustainable Cities: Climate Information for Improved Planning and Management of Cities (Producers/Capabilities Perspective). – Proc. Env. Sci. **1**, 247–274.

Hartmann, D.L. , 1994: Global Physical Climatology. - Academic Press, 411 pp.

Hutter, H. P, H. Moshammer, P. Wallner, B. Leitner, M. Kundi, 2007: Heatwaves in Vienna: effects on mortality. – Wien Klin. Wochenschr. **119**, 223–227.

IPCC, 2013: The Physical Science Basis, Contribution of Working Group I to the Fifth Assessment Report of the Intergovernmental Panel on Climate Change. – In: Climate Change 2013, Stocker, T.F., D. Qin, G-K. Plattner, M.M.B. Tignor, S.K. Allen, J. Boschung, A. Nauels, Y. Xia, V. Bex, P.M. Midgley, Cambridge University Press, Cambridge, United Kingdom and New York, NY, USA, 1535 pp.

Jacob, D., J. Petersen, B. Eggert, A. Alias, O.B. Christensen, L.M. Bouwer, A. Braun, A. Colette, M. Déqué, G. Georgievski, E. Georgopoulou, A. Gobiet, L. Menut, G. Nikulin, A. Haensler, N. Hempelmann, C. Jones, K. Keuler, S. Kovats, N. Kröner, S. Kotlarski, A. Kriegsmann, E. Martin, E. v. Meijgaard, C. Moseley, S. Pfeifer, S. Preuschmann, C. Radermacher, K. Radtke, D. Rechid, M. Rounsevell, P. Samuelsson, S. Somot, J. -F. Soussana, C. Teichmann, R. Valentini, R. Vautard, B. Weber, P. Yiou, 2014: EURO-CORDEX: new high-resolution climate change projections for European impact research. – Reg. Env. Change. **14**, 2, 563–578 DOI:10.1007/s10113-013-0499-2.

Jasper, K., P. Calanca, J. Fuhrer, 2006: Changes in summertime soil water patterns in complex terrain due to climatic change. – J. Hydrol. **327**, 3–4, 550–563 DOI:10.1016/j.jhydrol.2005.11.061.

Jendritzky, G., R. De Dear, G. Havenith, 2012: UTCI – Why another thermal index? – Int. J. Biometeorol. **56**, 421–428.

Jones, R., J. Murphy, D. Hassell, R. Taylor, 2001: Ensemble mean changes in a simulation of the European climate of 2071–2100 using the new Hadley Centre regional modelling system HadAM3H/HadRM3H. – Hadley Centre, Met Office, Bracknell, UK. http://prudence.dmi.dk/public/publications/hadley_200208.pdf (last access: 06.06.2019).

Kalisa, E., S. Fadlallah, M. Amani, L. Nahayo, G. Habiyaremye, 2018: Temperature and air pollution relationship during heatwaves in Birmingham, UK. – Sustain. Cities Soc. **43**, 111–120.

Kennedy, C., J. Steinberger, B. Gasson, Y. Hansen, T. Hillman, M. Havránek, D. Pataki, A. Phdungsilp, A. Ramaswami, G.V. Mendez, 2009: Greenhouse Gas Emissions from Global Cities. – Environmental Science & Technology **43**, 7297–7302. DOI:10.1021/es900213p.

Ketterer, C., A. Matzarakis, 2015: Comparison of Different Methods for the Assessment of the Urban Heat Island in Stuttgart, Germany. – Int. J. Biometeorol. **59**, 1299–1309 DOI:10.1007/s00484-014-0940-3.

Ketterer, C., M. Gangwisch, D. Fröhlich, A. Matzarakis, 2017: Comparison of Selected Approaches for Urban Roughness Determination Based on Voronoi Cells. – Int. J. Biometeorol. **61**, 1, 189–98. DOI:10.1007/s00484-016-1203-2.

Kim, J., J. Kyselý, 2009: Mortality during heat waves in South Korea, 1991 to 2005: How exceptional was the 1994 heat wave? – Climate Res. **38**, 105–116. DOI:10.3354/cr00775.

Kohler, M., C. Tannier, N. Blond, R. Aguejdad, A. Clappier, 2017: Impacts of several urban-sprawl countermeasures on building (space heating) energy demands and urban heat island intensities. A case study. – Urban Climate **19**, 92–121. DOI:10.1016/j.uclim.2016.12.006.

Kornhuber, K., V. Petoukhov, S. Petri, S. Rahmstorf, D. Coumou, 2017: Evidence for wave resonance as a key mechanism for generating high-amplitude quasi-stationary waves in boreal summer. – Climate Dynamics, **49**, 5–6, 1961–1979 DOI:10.1007/s00382-016-3399-6.

Krispel, S., M. Peyerl, P. Weihs, G. Maier, 2017: Reduction of Urban Heat Islands with Whitetopping. –Bauphysik. **39**, 1, 33–39.

Kuttler, W., S. Weber, J. Schonnefeld, A. Hesselschwerdt, 2007: Urban/rural atmospheric water vapour pressure differences and urban moisture excess in Krefeld, Germany. – International Journal of Climatology, **27**, 14, 2005–2015. DOI:10.1002/joc.1558.

Kyselý, J., J. Kalvová, V. Kveton, 2000: Heat waves in the South Moravian region during the period 1961–1995. – Studia Geophys Geodaet. **44**, 57–72.
Landsberg, H.E., 1981: The Urban Climate. – Academic Press, 275 pp.
Lee, H., H. Mayer, 2018: Thermal comfort of pedestrians in an urban street canyon is affected by increasing albedo of building walls. – Int. J. Biometeorol. **62**, 1199–1209. DOI: 10.1007/s00484-018-1523-5.
Lemonsu, A., C.S.B. Grimmond, V. Masson, 2004: Modeling the surface energy balance of the core of an old Mediterranean City: Marseille. – J. Appl. Meteor. Climatol. **43**, 312–327.
Lemonsu, A., V. Masson, L. Shashua-Bar, E. Erell, D. Pearlmutter, 2012: Inclusion of vegetation in the Town Energy Balance model for modelling urban green areas. – Geosci. Model Develop. **5**, 1377–1393.
Lemonsu, A., R. Kounkou-Arnaud, J. Desplat, J.L. Salagnac, V. Masson, 2013: Evolution of the Parisian urban climate under a global changing climate. – Climatic Change **116**, 679–692.
Leuprecht, A., B. Chimani, M. Hofstätter, M. Kerschbaumer, S. Kienberger, M. Kottek, H. Truhetz, A. Lexer, S. Pessenteiner, 2017: ÖKS15 bias corrected Euro-Cordex models, version 2. – https://data.ccca.ac.at/group/oks15 (last access: 05.09.2019).
Li, Y., R. Babcock, 2014: Green roofs against pollution and climate change. A review. – Agro. Sustain. Develop. **34**, 695–705. DOI:10.1007/s13593-014-0230-9.
MA (Magistratsabteilung) 18 – Stadtentwicklung und Stadtplanung, 2005: Urban Development Plan Vienna 2005 – STEP05, https://www.wien.gv.at/stadtentwicklung/strategien/step/step05/download/pdf/step-gesamt.pdf (in German), https://w.at/stadtentwicklung/strategien/step/step05/download/pdf/step05kurz-en.pdf (last access: 05.08.2019).
MA (Magistratsabteilung) 18 – Stadtentwicklung und Stadtplanung, 2011: Patterns for new urban developments. – Werkstattberichte der Stadtentwicklung Wien Nr. **116**, https://www.wien.gv.at/stadtentwicklung/studien/b008197.html (last access: 05.08.2019).
MA (Magistratsabteilung) 18 – Stadtentwicklung und Stadtplanung, 2014a: Smart City Wien – Framework Strategy, https://www.wien.gv.at/stadtentwicklung/studien/pdf/b008384b.pdf (last access: 05.08.2019).
MA (Magistratsabteilung) 18 – Stadtentwicklung und Stadtplanung, 2014b: Urban Development Plan Vienna 2015 – STEP 2025 (in German), www.step.wien.at (last access: 05.08.2019).
MA (Magistratsabteilung) 22 – Umweltschutz, 2018: Urban Heat Island Strategy, Vienna. – https://www.wien.gv.at/umweltschutz/raum/pdf/uhi-strategieplan-englisch.pdf (last access: 2019.04.12).
Mahmood, R., K.G. Hubbard, R.D. Leeper, S.A. Foster, 2008: Increase in Near-Surface Atmospheric Moisture Content due to Land Use Changes: Evidence from the Observed Dewpoint Temperature Data. – Mon. Wea. Rev. **136**, 1554–1561 DOI:10.1175/2007MWR2040.1.
Masson, V. , 2000: A physically-based scheme for the urban energy budget in atmospheric models. – Bound-Layer Meteor. **94**, 357–397 DOI:10.1023/A:1002463829265.
Masson, V., C.S.B. Grimmond, T.R. Oke, 2002: Evaluation of the Town Energy Balance (TEB) scheme with direct measurements from dry districts in two cities. – J. Appl. Meteor. **41**, 1011–1026.
Masson, V., M. Bonhomme, J.-L. Salagnac, X. Briottet, A. Lemonsu, 2014: Solar panels reduce both global warming and urban heat island. – Front. Environ. Sci. **2**, published online. DOI:10.3389/fenvs.2014.00014.
Matzarakis, A., C. Endler, 2010: Climate change and thermal bioclimate in cities: Impacts and options for adaptation in Freiburg, Germany. – Int. J. Biometeorol. **54**, 479–83. DOI: 10.1007/s00484-009-0296-2.
Matzarakis, A., S. Muthers, E. Koch, 2011: Human biometeorological evaluation of heat-related mortality in Vienna. – Theor. Appl. Climatol. **105**, 1–10. DOI:10.1007/s00704-010-0372-x.
McMichael, A.J., R. Woodruff, K. Whetton, N. Hennessy, N. Nicholls N., S. Hales, A. Woodward, T. Kjellstrom, 2003: Human Health and Climate Change in Oceania: Risk Assessment Canberra. – Commonwealth Department of Health and Ageing, http://citeseerx.ist.psu.edu/viewdoc/download?doi=10.1.1.183.6422&rep=rep1&type=pdf (last access: 05.08.2019).
Mayer, H., P. Höppe, 1987: Thermal comfort of man in different urban environments. – Theor. Appl. Climatol. **38**, 43–49 DOI: 10.1007/BF00866252.
Michalakes, J., S. Chen, J. Dudhia, L. Hart, J. Klemp, J. Middlecoff, W. Skamarock, 2001: Development of a next-generation regional weather research and forecast model. – In: World Scientific (Pub.): Developments in Teracomputing. 269–276.
Michelozzi, P., F. De Donato, G. Accetta, F. Forastiere, M. D'Ovidio, C.A. Perucci, 2004: Impact of heatwaves on mortality – Rome, Italy – June–August 2003. – JAMA. **291**, 2537–2538. DOI:10.1001/jama.291.21.2537.
Morecroft, M.D., M.E. Taylor, H.R. Oliver, 1998: Air and Soil Microclimates of Deciduous Woodland Compared to an Open Site. – Agricult. Forest Meteor. **90**, 141–56. DOI: 10.1016/S0168-1923(97)00070-1.
Morini, E., A. Touchaei, B. Castellani, F. Rossi, F. Cotana, 2016: The Impact of Albedo Increase to Mitigate the Urban Heat Island in Terni (Italy) Using the WRF Model. – Sustainability **8**, 999. DOI:10.3390/su8100999.
Muthers, S., A. Matzarakis, E. Koch, 2010: Climate change and mortality in Vienna – a human biometeorological analysis based on regional climate modeling. – Int. J. Environ. Res. Public Health. **7**, 2965–2977. DOI:10.3390/ijerph7072965.
Neuwirth, C., 2015: Effects of climate on Urban Trees in Vienna. – Master Thesis (in German) at the Institute of Soil Bioengineering and Landscape Construction, University of Natural Resources and Life Sciences, Vienna, https://zidapps.boku.ac.at/abstracts/download.php?dataset_id=11754&property_id=107 (last access: 11.10.2019).
Offerle, B., P. Jonsson, I. Eliasson, C.S.B. Grimmond, 2005: Urban modification of the surface energy balance in the West African Sahel: Ouagadougou, Burkina Faso. – J. Climate **18**, 3983–3995.
Oke, T. R., 1982: The energetic basis of the urban heat island. – Quart. J. Roy. Meteor. Soc. **108**, 1–24. DOI:10.1002/qj.49710845502.
Oke, T. R., 1987: Boundary Layer Climates. – Routledge, Taylor&Francis Group, 464 pp.
ÖROK, 2017: ÖROK Atlas (in German), https://www.oerok-atlas.at/#indicator/65 (last access: 05.08.2019).
Otani, H., G. Takayuki, G. Heita, S. Minayuki, 2017: Time-of-day effects of exposure to solar radiation on thermoregulation during outdoor exercise in the heat. – Chronobiol. Int. **34**, 1224–1238.
Pearlmutter, D., P. Berliner, E. Shaviv, 2005: Evaluation of urban surface energy fluxes using an open-air scale model. – Bound.-Layer Meteor. **44**, 532–545.
Pigeon, G., K. Zibouche, B. Bueno, J. Le Bras, V. Masson, 2014: Improving the capabilities of the Town Energy Balance model with up-to-date building energy simulation algorithms:

an application to a set of representative buildings in Paris. – Energy Build. **76**, 1–14.

Pineda, N., O. Jorba, J. Jorge, J. Baldasano, 2004: Using NOAAAVHR Rand SPOT VGT data to estimate surface parameters: application to a mesoscale meteorological model. – Int. J. Remote Sens. **25**, 129–143.

PGO (Planungsgemeinschaft Ost), 2011: stadtregion+ (in German), Planungskooperation zur räumlichen Entwicklung der Stadtregion Wien Niederösterreich Burgenland, http://www.planungsgemeinschaft-ost.at/fileadmin/root_pgo/Studien/Raumordnung/Zwischenbericht_Stadtregion.pdf (last access: 05.08.2019).

Rad, H.R., M. Rafieian, H. Sozer, 2017: Evaluating the effects of increasing of building height on land surface temperature. – Int. J. Urban Manage Energy Sustain. **1**, 11–16. DOI:10.2034/ijumes.2017.01.01.002.

Rafael, S., H. Martins, E. Sá, D. Carvalho, C. Borrego, M. Lopes, 2016: Influence of urban resilience measures in the magnitude and behaviour of energy fluxes in the city of Porto (Portugal) under a climate change scenario. – Sci. Total Environ. **566–567**, 1500–1510, DOI: 10.1016/j.scitotenv.2016.06.037.

Ramamurthy, P., T. Sun, K. Rule, E. Bou-Zeid, 2015: The Joint Influence of Albedo and Insulation on Roof Performance: A Modeling Study. – Energy Build. **102**, 317–27. DOI: 10.1016/j.enbuild.2015.06.005.

Redon, E.C., A. Lemonsu, V. Masson, B. Morille, M. Musy, 2017: Implementation of street trees within the solar radiative exchange parameterization of TEB in SURFEX v8.0. – Geosci. Model Develop. **10**, 385–411. DOI: 10.5194/gmd-10-385-2017.

Roman, K.K., T. O'Brien, J.B. Alvey, O. Woo, 2016: Simulating the Effects of Cool Roof and PCM (Phase Change Materials) Based Roof to Mitigate UHI (Urban Heat Island) in Prominent US Cities. – Energ. **96**, 103–17, DOI:10.1016/j.energy.2015.11.082.

Salamanca, F., A. Martilli, C. Yagüe, 2012: A Numerical Study of the Urban Heat Island over Madrid during the DESIREX, 2008: Campaign with WRF and an Evaluation of Simple Mitigation Strategies. – Int. J. Climatol. **32**, 2372–2386. DOI:10.1002/joc.3398.

Schicker, I., D. Arnold Arias, P. Seibert, 2016: Influences of updated land-use datasets on WRF simulations for two Austrian regions. – Meteor. Atmos. Phys. **128**, 279–301 DOI: 10.1007/s00703-015-0416-y.

Schimann, J., 2015: The effect of climate on trees in streets of Vienna. – Bachelor Thesis (in German) at the Institute of Soil Bioengineering and Landscape Construction, University of Natural Resources and Life Sciences, Vienna.

Schnell, J.L., M.J. Prather, 2017: Co-occurrence of extremes in surface ozone, particulate matter, and temperature over eastern North America. – Proc. Natl. Acad. Sci. USA. **114**, 2854–2859 DOI:10.1073/pnas.1614453114.

Schreier, S., I. Suomi, P. Bröde, H. Formayer, H.E. Rieder, I. Nadeem, G. Jendritzky, E. Batchvarova, P. Weihs, 2013: The uncertainty of UTCI due to uncertainties in the determination of radiation fluxes derived from numerical weather prediction and regional climate model simulations. – Int. J. Biometeorol. **57**, 2, 207–223.

Schrijvers, P.J.C., H.J.J. Jonker, S.R. de Roode, S. Kenjereš, 2016: The Effect of Using a High-Albedo Material on the Universal Temperature Climate Index within a Street Canyon. – Urban Climate **17**, DOI:10.1016/j.uclim.2016.02.005.

Seneviratne, S.I., R. Wartenburger, B.P. Guillod, A.L. Hirsch, M.M. Vogel, V. Brovkin, D.P. van Vuuren, N. Schaller, L. Boysen, K.V. Calvin, J. Doelman, P. Greve, P. Havlik, F. Humpenöder, T. Krisztin, D. Mitchell, A. Popp, K. Riahi, J. Rogelj, C.-F. Schleusser, J. Sillmann, E. Stehfest, 2018: Climate extremes, land–climate feedbacks and land-use forcing at 1.5 °C. – Philosophical Transactions of the Royal Society A: Mathematical, Physical and Engineering Sciences **376**, 2119, DOI:10.1098/rsta.2016.0450.

Sharifi, A., Y. Yamagata, 2018: Resilience-Oriented Urban Planning. – In: Yamagata, Y., A. Sharifi (Eds.): Resilience-Oriented Urban Planning. – Lecture Notes in Energy **65**, 3–27. DOI:10.1007/978-3-319-75798-8_1.

Skamarock, W.C., J.B. Klemp, J. Dudhia, D.O. Gill, D.M. Barker, M.G. Duda, X.-Y. Huang, W. Wang, J.G. Powers, 2008: A Description of the Advanced Research WRF Version 3. – NCAR. Tech. Note NCAR/TN-475+STR, 113 pp.

Steadman, R.G. , 1979a: The Assessment of Sultriness. Part I: A Temperature-Humidity Index Based on Human Physiology and Clothing Science. – J. Appl. Meteor. **18**, 861–873. DOI: 10.1175/1520-0450(1979)018<0861:TAOSPI>2.0.CO;2.

Steadman, R. G., 1979b: The Assessment of Sultriness. Part II: Effects of Wind, Extra Radiation and Barometric Pressure on Apparent Temperature. – J. Appl. Meteor. **18**, 874–885 DOI: 10.1175/1520-0450(1979)018<0874:TAOSPI>2.0.CO;2.

Stewart, I.D., T.R., Oke, 2012: Local climate zones for urban temperature studies. – Bull. Amer. Meteor. Soc. **93**, 1879–1900.

Stull, R. B., 1988: An Introduction to Boundary Layer Meteorology. – Kluwer academic Publishers, Dordrecht-Boston-London.

Switanek, M.B., P.A. Troch, C.L. Castro, A. Leuprecht, H.-I. Chang, R. Mukherjee, E.M.C. Demaria, 2017: Scaled distribution mapping: a bias correction method that preserves raw climate model projected changes. – Hydrol. Earth Syst. Sci. **21**, 2649–2666. DOI:10.5194/hess-21-2649-2017.

Taha, H., S. Douglas, J. Haney, 1997: Mesoscale meteorological and air quality impacts of increased urban albedo and vegetation. – Energy Build. **25**, 169–177. DOI:10.1016/S0378-7788(96)01006-7.

Tan, J., Y. Zheng, G. Song, L. Kalkstein, A. Kalkstein, X. Tang, 2007: Heatwave Impacts on Mortality in Shanghai: 1998 to 2003. – Int. J. Biometeorol. **51**, 193.

Taylor, K.E., R.J. Stouffer, G.A. Meehl, 2012: An Overview of CMIP5 and the Experiment Design. – Bull. Am. Meteorol. Soc. **93**, 4, 485–498 DOI:10.1175/BAMS-D-11-00094.1.

Urban, A., J. Kyselý, 2014: Comparison of UTCI with Other Thermal Indices in the Assessment of Heat and Cold Effects on Cardiovascular Mortality in the Czech Republic. – Int. J. Env. Res.Public Health **11**, 952–67. DOI:10.3390/ijerph110100952.

Ürge-Vorsatz, D., C. Rosenzweig, R.J. Dawson, R.S. Rodriguez, X. Bai, A.S. Barau, K.C. Seto, S. Dhakal, 2018: Locking in Positive Climate Responses in Cities. – Nature Climate Change **8**, 174–77. DOI:10.1038/s41558-018-0100-6.

Valleron, A.J., A. Boumendil, 2004: Epidemiology and heat waves: Analysis of the 2003 episode in France. – C.R. Biology **327**, 1125–41.

Vidale, P.L., D. Lüthi, R. Wegmann, C. Schär, 2007: European summer climate variability in a heterogeneous multimodel ensemble. – Climatic Change **81**, S1, 209–232. DOI: 10.1007/s10584-006-9218-z.

Vogel, M.-M., 2018: Temperature extremes in a changing climate – Processes, emergent constraints and impacts. – Doctoral Thesis at ETH Zürich, DOI:10.3929/ethz-b-000323120.

Wang, C., Z.-H. Wang, J. Yang. 2018: Cooling Effect of Urban Trees on the Built Environment of Contiguous United States. – Earth's Future **6**,1066–1081. DOI:10.1029/2018EF000891.

Weihs, P., H. Staiger, B. Tinz, E. Batchvarova, H. Rieder, L. Vuilleumier, M. Maturilli, G. Jendritzky, 2012: The uncertainty of UTCI due to uncertainties in the determination of radiation fluxes derived from measured and observed meteorological data. – Int. J. Biometeorol. **56**, 537–555.

Weihs, P., S. Zamini, S. Krispel, S. Oswald, M. Peyerl, M. Revesz, A. Schneider, H. Trimmel, 2018: Optimierung reflektierender Materialien und Photovoltaik im Stadtraum bezüglich Strahlungsbilanz und Bioklimatik (PVOPTI-Ray). (in German), Berichte aus Energie- und Umweltforschung 18/2018 Nachhaltig wirtschaften, Bundesministerium für Verkehr, Innovation und Technologie, Wien, https://nachhaltigwirtschaften.at/resources/sdz_pdf/schriftenreihe_2018-18_pvoptiray.pdf (last access: 05.08.2019).

Zampieri, M., F. D'Andrea, R. Vautard, P. Ciais, N. de Noblet-Ducoudré, P. Yiou, 2009: Hot European Summers and the Role of Soil Moisture in the Propagation of Mediterranean Drought. – J. Climate **22**, 4747–4758. DOI: 10.1175/2009JCLI2568.1.

Zare, S., N. Hasheminejad, H.E. Shirvan, R. Hemmatjo, K. Sarebanzadeh, S. Ahmadi, 2018: Comparing Universal Thermal Climate Index (UTCI) with selected thermal indices/environmental parameters during 12 months of the year. – Wea. Climate Extremes **19**, 49–57. DOI:10.1016/j.wace.2018.01.004.

Zeiler, S. , 2015: Auswirkungen des Klimas auf Stadtbäume im Bezirk Korneuburg/Niederösterreich. – Master Thesis (in German), Institute of Soil Bioengineering and Landscape Construction, University of Natural Resources and Life Sciences, Vienna, 231 pp, https://zidapps.boku.ac.at/abstracts/download.php?dataset_id=12169&property_id=107 (last access: 11.10.2019).

Zhang, H., Y. Wang, T. Park, Y. Deng, 2017: Quantifying the relationship between extreme air pollution events and extreme weather events. – Atmos. Res. **188**, 64–79.

Zommers, Z., K. Alverson, 2018: Resilience – The Science of Adaptation to Climate Change. – Elsevier, Amsterdam, Oxford, Camebridge, 354 pp.

Žuvela-Aloise, M., K. Andre, K., H. Schwaiger, D.N. Bird, H. Gallaun, 2018: Modelling reduction of urban heat load in Vienna by modifying surface properties of roofs. – Theor. Appl. Climatol. **131**, 1005–1018. DOI:10.1007/s00704-016-2024-2.

The pdf version (Adobe Java Script must be enabled) of this paper includes an electronic supplement:

Table of content – Electronic Supplementary Material (ESM)

A.3 Other Contribution: III

H. Trimmel, P. Weihs, S. Faroux, H. Formayer, C. Gützer, K. Hasel, D. Leidinger, A. Lemonsu, V. Masson, I. Nadeem, S. Oswald, M. Revesz, and R. Schoetter. Influence of urban growth of the city Vienna on the thermal comfort of its habitants. [Poster] [EGU General Assembly 2019, Vienna, 7.-12. April 2019], *Geophysical Research Abstracts*, 21, 14726–14726.

Influence of urban growth of the city Vienna on the thermal comfort of its inhabitants

Heidelinde Trimmel (1), Philipp Weihs (1), Stéphanie Faroux (2), Herbert Formayer (1), Christian Gützer (1), Kristofer Hasel (1), David Leidinger (1), Aude Lemonsu (2), Valéry Masson (2), Imran Nadeem (1), Sandro Oswald (1,3), Michael Revesz (1), and Robert Schoetter (2)

(1) University of Natural Resources and Life Sciences, Institute of Meteorology, Water-Atmosphere-Environment, Vienna, Austria (heidelinde.trimmel@boku.ac.at)

(2) CNRM, CNRS-Météo France, Toulouse, France (valery.masson@meteo.fr), (3) Urban Climate Modelling, Central Institution of Meteorology and Geodynamics (ZAMG), Vienna, Austria

*heidelinde.trimmel@boku.ac.at

Urban Growth + Scenarios

Until 2030, the population within the metropolitan area (stadtregion+, PGO2011) of Vienna is expected to increase by 10 % (ÖROK 2017). This will cause the living space to be expanded and densified. However, already now the population is suffering from heat stress during the summer months. The aim of the project URBANIA was to estimate the change in thermal comfort of inhabitants during heatwaves in the timeframe 2030/2050 potentially caused by urban development and climate change and test solutions. The additional needed built floor area can be achieved in mainly two different ways: urban expansion und urban densification. Therefore two future scenarios were developed and simulated (see Table 1), which both distribute the same new additional floor area and include already known new development areas:

„SPR" which assumes maximum urban growth on the „green lawn" without any reconsideration of used building materials.

„OPT" assumes, that presently unused floor areas as attics or ground floors are turned into usable space. Additionally, industrial areas with low building density are densified, as well as low density residential area. Additional the urban materials are changed in order to reduce the heat island. This scenario is in correspondence with the municipal strategy to built a sustainable city.

For the change in meteorological condition two episodes representing extreme heat waves with a 15yr return period for the present climate (2015) and future climate around 2050 (2069) were chosen.

Name of urban scenario:	„REF"	„SPR"	„OPT"
	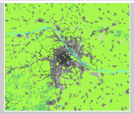	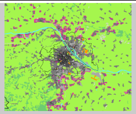	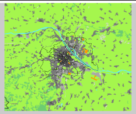
Total built urban area [km²] (relative to "REF" [%])	929 (100%) Actual urban area	1115 (120%) Actual urban area +known development +urban expansion	939 (101%) Actual urban area +known development
Portion of built area for: low density residential, high density residential, commercial [%]	22, 46, 16	22, 46, 16	24.2, 46, 24.2
Thermal conductivity roof [W/mK]	1.7	1.7	0.1
Thermal conductivity wall [W/mK]	1.4	1.4	0.1
Thermal conductivity ground [W/mK]	0.9	0.9	0.4
Thermal conductivity windows [W/mK]			0.9
Albedo roof [-]	0.15	0.15	0.68
Albedo wall [-]	0.2	0.2	0.3
Albedo ground [-]	0.138	0.3	0.3

Table 1: Definition of the 3 different urban scenarios REF (i.e. the reference), SPR and OPT and their characteristic properties.

Simulation and Validation

Simulations were done with the Weather Research and Forecasting Model WRF v3.7.1 (Skamarock et al. 2008). WRF and the Town Energy Balance Modell TEB (Masson 2000) were coupled online. The WRF-TEB runs were used to force SURFEXv8 (Boone et al. 2017) to derive the thermal comfort index UTCI. The distribution of urban areas was derived from Corine2012 land cover dataset (EEA/Copernicus) and simplified to 3 urban classes. Urban parameters for Vienna as albedo (Schweiger et al. 2018), thermal conductivity (Amtmann M and Altmann-Mavaddat N (2014), Berger et al. 2012) were assigned.

The Comparison of radiation balance and air temperature between models and ground stations within the urban structure show high correlations (Figure 1 + 2).

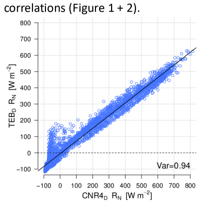

Figure 1: Comparison of radiation balance measured at the top of an urban canyon in Vienna with values modelled with TEB.

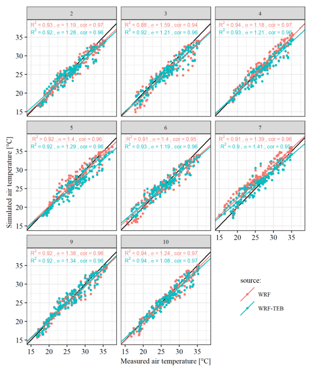

Figure 2: Comparison of the measured 2m air temperature with values modelled with WRF und WRF-TEB for 8 sites in Vienna.

Results

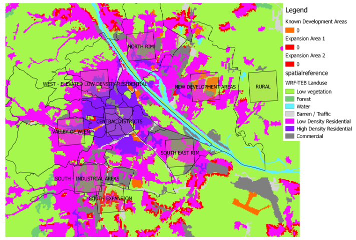

Figure 3: Subregions chosen for further analysis (clockwise): Central Districts (CE), North-Rim (NO), New development areas: Seestadt Aspern (SA), South-eastern rim (SE), South-industrial (SI), South expansion (SX), Valley of Wien (VW), West – elevated low density residential (WE).

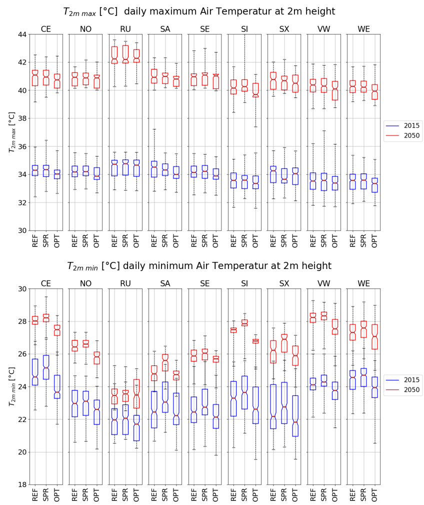

Figure 4: Daily maximum (top) and minimum (bottom) 2m air temperature within the 9 different subregions (see Figure 3) for the chosen climate episode for 2015 and 2050, blue and red respectively, and the 3 different urban development scenarios (sh. Table 1).

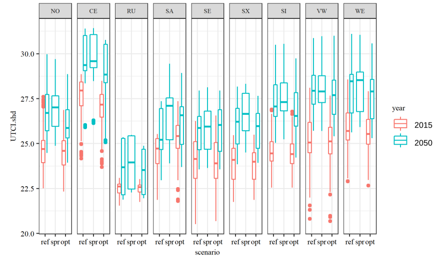

Figure 5: Comparison of the daily minimum UTCI temperatures in shadow for the 3 different urban development scenarios (see Table 1) within the 9 different subregions (see Figure 3) and for the chosen climate episodes 2015 and 2050, in red and turquoise respectively.

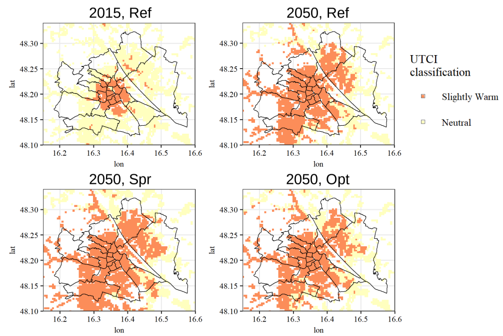

Figure 6: Comparison of the mapped distribution of UTCI categories in Vienna for the daily minimum UTCI values in shadow. Comparison of the scenario REF in 2015 as reference (upper left) with the results for the different urban development scenarios (REF, SPR and OPT) in.

Conclusions

- Maximum air temperatures during an extreme heat wave are expected to increase within the next 50 years during extreme events by around 7 °C , minimum air temperature by around 2 - 4°C. The variation of the minimum temperature between different areas is higher than that of the maxima.
- Future increases of UTCI in °C lie in the same range as increases in air temperature which signifies a change of 1 category of UTCI.
- In the urban sprawl scenario „SPR" the UTCI is slightly increased in most regions, in the optimized urban development scenario „OPT" the UTCI is slightly reduced in most areas, only in new development areas (SA) and strong densified areas (SE) the UTCI is increased due to the new buildings.
- In both scenarios the change is too little to change one UTCI category.
- more info at: http://urbania.boku.ac.at

The project URBANIA was funded by the ACRP Call No 8 (KR15AC8K12615). We thank Jürgen Preiss, the MA18 and Beatrix Gasienica-Wawrytko for their help and feedback.

Amtmann M and Altmann-Mavaddat N (2014) Eine Typology österreichischer Wohngebäude, Österreichische Energieargentur – Austrian Energy Agency, TABULA/EPISCOPE

Berger T, H. Formayer, R. Smutny, C. Neururer, R. Passawa (2012) Auswirkungen des Klimawandelsauf den thermischen Komfort in Bürogebäuden, Berichte aus Energie- und Umweltforschung

Boone, A. et al. 2017: The interactions between soil–biosphere–atmosphere land surface model with a multi-energy balance (ISBA-MEB) option in SURFEXv8 – Part 1: Model description, Geosci. Model Dev., 10, 843-872.

EEA/Copernicus: CORINE Land Cover data set, https://land.copernicus.eu/pan-european/corine-land-cover, last access: 17.4.2018

H. Schwaiger, D. Neil Bird, H. Gallaun, M. Zuvela-Aloise, K. Andre (2018): Reduktion städtischer Wärmeinseln durch Verbesserung der Abstrahleigenschaften von Gebäuden und Quartieren (KELVIN), Berichte aus Energie- und Umweltforschung 29/2018

Masson V (2000) A physically-based scheme for the urban energy budget in atmospheric models. Bound-Layer Meteorol 94:357–397. doi: 10.1023/A:1002463829265

PGO (Planungsgemeinschaft Ost) (2011) stadtregion +, Planungskooperation zur räumlichen Entwicklung der Stadtregion Wien Niederösterreich Burgenland

ÖROK 2017: www.oerok-atlas.at

Skamarock, W.C. et al. 2008: A Description of the Advanced Research WRF Version 3. NCAR. Tech.Note NCAR/TN-475+STR,113pp